Non-equilibrium phenomena in magnetotransport in epitaxial graphene

Viktoria Eless

Supervisors: Prof. Alexander Tzalenchuk, Dr. Vladimir Antonov

Thesis submitted in part fulfilment of the requirement for the degree of Doctor of Philosophy from Royal Holloway, University of London

Declaration of Authorship

I, Viktoria Eless, hereby declare that this thesis and the work presented in it is entirely my own. Where I have consulted the work of others this is always clearly stated.

Signed:_____
Date:_____

Contents

List of Figures

Acknowledgements

I would like to thank my supervisors Vladimir Antonov and Sasha Tzalenchuk for giving me the opportunity to do this project. Perhaps through optimism, or great foresight, they have given me chance to learn more than I thought I could.

At the start of the PhD I used to wonder how there could be so many people to thank at the end, when most people were working on other things, but as time passed I realised that each small accomplishment of mine was aided by multiple helping hands. The Quantum Detection group has become like an extended Physics family to me, surrounding me with diverse tidbits of knowledge, amiable company and vital pieces of equipment at crucial moments.

I am greatly indebted to those who ended up being in nearest proximity to my work and were regularly called upon to help me throughout the years, despite having no obligation to do so. In order of greatest suffering I thank Sergiy Rozhko, Patrick Joseph-Franks and Steve Giblin - I have learnt a great deal from you.

Special thanks go to Jon Fletcher who designed and developed the noise measurement system that could then be quickly deployed and made a major experimental contribution in short space of time. Our temporary CDT student on the experiment, Jake Ayres, deserves a special mention because without his handiwork to get the project moving I could have either produced this document or made measurements, but not both.

I'm grateful to the many students I have got to know, many of whom have passed time in our student office, some even before such a thing existed: Adam, Ana, Bo, Cat, Christos, Hector, Ilana, John, Jon B, Joseph, Lauren, Miriam, Nathan, Pardis, Ravish, Shean, Tom, Trupti, and Vish. Thank you for the practical and moral support, big and small.

I have learnt why friends and family are mentioned here, despite having nothing to with the work itself they deserve credit for keeping us going - with support logistics in some cases! Sam Cottrell is the exception to this rule by also being responsible for dragging my stick figures into the 21st century.

My mum, the inimitable Mrs. Bennett, will get her own book one day rather than a mention here, and I'll let her choose the topic this time.

Finally and foremost my deepest thanks go to Sasha for not only imparting of his vast amount of knowledge to me, but for simultaneously encouraging me with your patience and good humour. It is the example I hope to follow.

Abstract

The quantum Hall effect (QHE) is used realise the standard for the unit of electrical resistance, the ohm, in terms of fundamental constants h/e^2. Epitaxial graphene on silicon carbide has become the system of choice for this because of the large inter-Landau level spacing, fast energy relaxation and very robust quantum Hall state, which is owed to the charge transfer between graphene and the substrate. There are however non-equilibrium dynamics in the quantum Hall regime in graphene, which need to be understood in order to better implement the resistance standard in the future.

This thesis concerns the study of this non-equilibrium dynamics in graphene, and in particular the breakdown of the QHE. In conventional semiconductor 2DEGs it is achieved by the study of the spectrum of the terahertz radiation emitted from the hot spots, where the electrons enter and leave the 2D conductor.

In graphene the non-equilibrium dynamics can be investigated using the weak localisation corrections to the conductivity, which are sensitive to any time-reversal symmetry breaking perturbation, including temperature, magnetic field or ac electric field. High-frequency microwave radiation was employed to generate hot electrons and showed that the response of graphene is entirely bolometric.

The response to MIR radiation (λ: 5-10 μm) was studied by measuring magnetoresistance of a graphene Hall bar in a wide range of magnetic fields. At intermediate magnetic fields, the response is a combination of the direct bolometric effect and a change in the carrier density due to radiation. The cyclotron resonance did not appear as expected at the appropriate magnetic fields, which is discussed.

Finally, the breakdown of the QHE in graphene was investigated by measuring cross-spectral noise power density over a 500 kHz window centred at 3.22 MHz. Comparing the spectra to those of a GaAs sample it seems that the breakdown in graphene may occur in the bulk of the graphene sample rather than in well-defined hot spots.

Part I.

Introduction

1. Metrology and the quantum Hall effect

"Measurement is the quantitative comparison of an unknown quantity with a standard quantity."[1]. This requires that a *standard quantity* be defined. The established standard quantity becomes the unit - the reference value of that quantity.
The science of measurement, metrology, focuses not only on definitions, but the best method for attaining the correct value of the chosen standard value of a quantity, more commonly known as accuracy, and the repeatability of the found value, more commonly known as precision. These two considerations naturally lead to a heavy preoccupation with uncertainty.

Generally the desired level for a metrological standard is to know a value with uncertainty on the order of one part in a billion. While this may seem an abstract and hypothetical preoccupation, it has strong practical consequences: the accuracy of any performed measurement cannot exceed that of the defined quantity used in the measurement [2]. The importance of this can be visualised by considering the machining of parts, for example in aviation, but actually in any area of our lives from all vehicles to kitchen appliances. Mass production gives countless examples and standardisation is key to all global trade, not just in dimensions, but weight; time synchronicity; and also electrical power.

The Système International d'Unités (SI) is a set of defined quantities that form the basis of measurement systems. Its origins lie in the 19th century with some of the first standards being defined by physical objects known as artifacts, such as the kilogram. The SI framework was established in 1960 and is based on international agreement (see fig 1.1). As science and technology have advanced, more precise techniques for defining units have become available such as replacing the physical metre rule with definition according to the length of the path of light in a vacuum.

The base unit of electrical metrology is the ampere, with the volt and the ohm as defined 'derived' units. The ohm is represented using the quantum Hall effect, which manifests as steps in transverse resistance in a two dimensional material, when it is carrying current and subject to a magnetic field at low temperatures (fig 1.4). These steps are defined by

a ratio of the fundamental constants h, Planck's constant and e, the electron charge, with the latter squared: h/e^2. This ratio is known as the von Klitzing constant, R_K, named after the scientist Klaus von Klitzing who discovered it in 1980.

The way the SI system works currently is to define solely the base (and derived) units. This means that the fundamental constants of nature are also measured quantities and ascribed an uncertainty, as can be seen at the front of many textbooks.

However, it is believed that the fundamental constants, such as h and e, are unchanging, possibly for billions of years [3]. The proposed redefinition of the SI system is to fix the fundamental constants h, e, Boltzmann constant, k_B and Avogadro's constant, N_A, remove their associated uncertainties and use them to define the base units. This would then guarantee longevity against future technical improvements.

1.1. Redefinition of the SI

There are currently seven SI base units: the metre, m, the kilogram, kg, the second, s, the ampere, A, the kelvin, K, the mole, mol and the candela, cd. The names of SI units are always written in lowercase letters, even where the unit symbol is a capital, showing that it is derived from a proper name. These cover the key quantities used in science to quantify the world around us: length, mass, time, electrical current, thermodynamic temperature, amount of substance and luminous intensity. This demonstrates how metrology stands at the unique convergence of the conceptual and the practical. It is then important to bear both considerations in mind when approaching the problem of defining a reference. A definition can be abstract, just as any chosen value can be arbitrary. In fact, some would say any chosen value is inherently arbitrary, but the interplay of definition and the motivation behind it to the chosen value have formed the rich and evolving history of units and the SI. An additional component arises when a system of units is under consideration: the units need to be *coherent* in order to form a system, rather than simply being a collection. The coherence of the SI as it stands is given by the laws of mechanics and electromagnetics [4].

The specific meaning of coherent in this context is that any unit should be related to any other unit by only a multiplicative or divisive combination, with a numerical prefactor of unit [4] This simple requirement is actually very stringent and results in the formation of two classes of dissemination of unit: the *realisation* and the *representation* of the unit.

The realisation of a unit is based on well defined principles, such as Maxwell's laws, and produces the unit in terms of the SI definition. The representation of a unit is a quantity which can routinely be compared the other standards. The existence of representations is necessitated by the fact that realisations are often difficult and time consuming, which can be prohibitive for routine calibrations. It is also the case that the sequence of measurements performed to get the result in coherent SI units is not necessarily the best in terms of precision, and while a more precise technique may exist it does not yield necessarily its results in SI units.

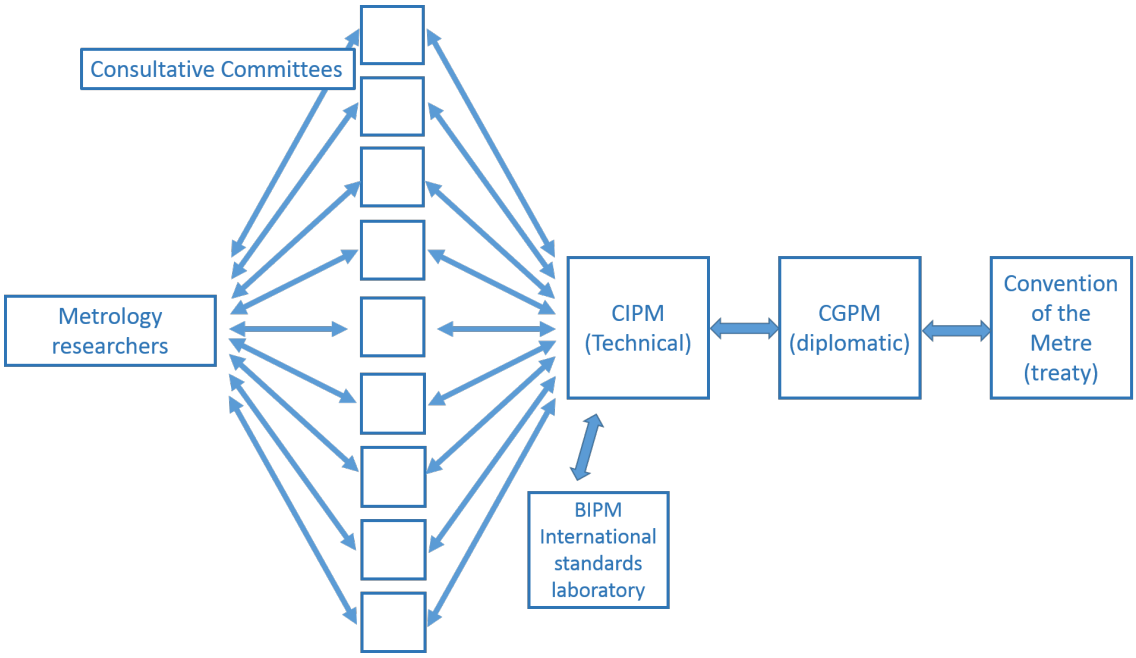

Figure 1.1.: International collaboration over physical units began in 1875 with the Convention of the Metre, which now forms the legal basis of the SI which was adopted by the Convention of the Metre in 1960 [4]. There is a diplomatic and a technical body; the CGPM (General Conference of Weights and Measures) and the CIPM (International Committee of Weights and Measures) respectively. The International Bureau of Weights and Measures (BIPM) is an international laboratory with a coordination role as well as an experimental one. However it is not a top-down management scheme. Generally, proposals for change originate from the metrological community and are put forward by consultative committees which can also form working groups that investigate and make detailed recommendations. These are then ratified in due course. Image and explanation after [4].

There are direct and indirect realisations for units. Indirect realisations rely on formulae, while direct realisations compare representations of a unit to the SI unit. While direct realisations may be challenging, they have the benefit of not assuming the validity of formulae. Agreed upon values are then the result of considering several representations as

part of realisations, which are then weighted in the final consideration.

Representations then either constitute the primary standard against which customer calibrations are carried out or calibrate the primary standard (fig 1.2). The existence of representations has advantages such as providing a cross-check of values without systematic errors and providing flexibility for technological development. However, some SI definitions have not been able to endure against improvements in measurements despite the flexibility of representations.

One example is the metre. The metre had more than one artifact definition, with the latest one agreed in 1889. This was replaced in 1960 using the wavelength of radiation emitted by krypton-86. The choice was made in part due to the advancement of microwave clocks compared to optical frequency clocks. It was a good choice in that despite being and advanced technique, it had not reached the limits of its development [5]. However in 1980 the current definiton was introduced which fixes the speed of light, but is more abstract. This did not mean that it became obligatory to measure the length of the path of light in a vacuum, but it did allow for the improving optical clocks to later replace the microwave clocks as the preferred technique without inadvertently outdating the definition. This example demonstrates the advantage of a making the definition *more* abstract. Although doing so may seem counterintuitive because the definition becomes further removed from an everyday physical quantity and may become more difficult to understand, it provides longevity for the unit.

The fact remains that a system for setting reference quantities would ideally be formed of unchanging components. Unfortunately artifacts drift which poses problems both with self-consistency and international agreement. Furthermore, minimising uncertainty of SI units is indispensible, not for its own sake but because in the calibration chain approximately one order of magnitude is lost in precision with each stage [6].

While technological advances would seem to enforce the continual evolution of unit definitions, advances in physics have actually provided the potential for permanence with the advent of quantum standards. Quantum standards not only have the benefit of giving very precise quantities that originate from atomic level properties of a substance, but are directly defined by fundamental constants. This can be reversed so that measurement of quantum phenomena provides an accurate measurement of the fundamental constants of nature. This opens the way to a new basis for the coherence of a unit sytem: to fix the fundamental constants, rather than treating classical laws as immutable.

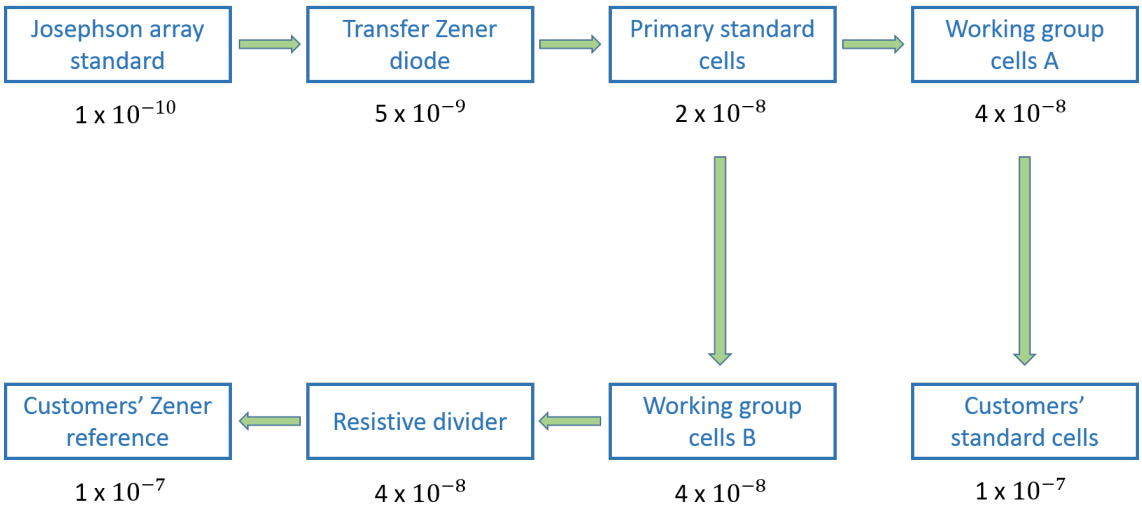

Figure 1.2.: An example of a calibration chain - the dissemination of the volt at the national standards laboratory of the USA, NIST. The loss in precision with each stage is evident.Image and explanation after [4].

This could seem to be a big change in the approach to the SI, but it was recognised already by Maxwell in an address to the British Association (an early unit committee), in 1890 that the use of nature's constants would be preferable [5]. To paraphrase his speech, a standard based on something fundamental i.e. that cannot be reduced further, such as wavelength, is reliable because any alteration to it would change its inherent nature. For instance, to alter the mass of hydrogen would result in having a different element. This is not necessarily the case with macroscopic quantities and phenomena. This more than supports the modern view that were the scientific community to set out to make a measurement system now, this would be the approach taken [1]. Fundamentally this is because the first reproducible measurements did not understand what was being measured to the same extent as is known today.

Some of the benefits of making the change can already be anticipated. Firstly, the kilogram will finally be able to move on from being defined by artifact [5]. Secondly, there will be a reduction in uncertainty, both for SI units and other constants. This was seen when the value of the speed of light, c was fixed. Consequently it fixed the magnetic permittivity of free space, μ_0 and the permeability of free space, ϵ_0, which then allowed for improvements in the uncertainty of the fine structure constant, α [3].

1.2. Electrical metrology

Historically the electrical units had electochemical representations. Weston cells were used as the standard for electromotive force (fig 1.3). Despite being an artifact they were not necessarily easy to use because when fully saturated the cell had a very strong temperature dependence.

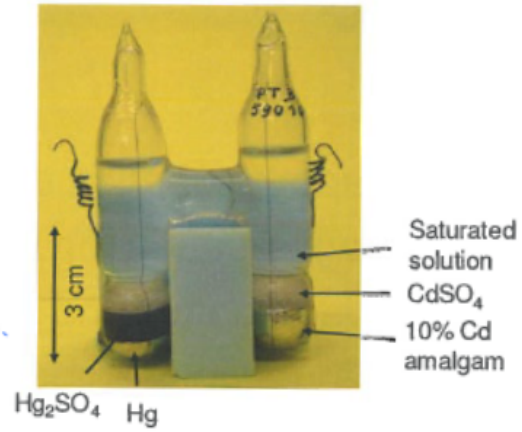

Figure 1.3.: The self-consistency checks that can be performed for all three electrical units if quantum standards are used.

The ampere is the base electrical unit but it is rarely used as the starting point for realising electrical units. Coincidentally, its early definition by electrolysis of silver and weighing the deposited amount was dependent on the Faraday constant, which contains the electron charge -then determined by the Millikan oil drop experiment. Despite its elegance, this definition was difficult to implement and was replaced in 1948 by the modern definition which is based in Ampère's law and the resultant force that occurs between two current carrying wires in a vacuum. Although this definition has not yet been superceded, this measurement is no longer carried out because its precision was limited to apprixmately one part in 10^6 [5].

Any representation is linked back to the SI unit, the absolute realisations of which is determined by linking electrical and mechanical measurement. A cornerstone of this is the calculable capacitor, as envisioned by Thomas and Lampard in 1956 [5], which uses four fixed and one mobile cylinder to measure the cross capacitance. This technique has the advantage that in it the capacitance depends only on length, and it allows the length

to be measured by displacement, rather than absolute distance [4]. Thus the metre yields the farad, which then yields the ohm. An absolute realisation of the volt can be obtained from the change in height of mercury in an electric field [5].

Since the advent of quantum phenomena very precise representations of the volt and the ohm are available, which are determined only by fundamental constants h and e. Their relatively simple implementation and fundamental basis then already allows for little need to distinguish between the SI unit and its representation [7].

1.2.1. Metrological triangle

Using quantum standards not only directly relates the electrical units to fundamental constants, but the units are therefore easily related to each other. This provides a self-consistency check that is free of systematic errors on the measurements themselves, but also on the values of h and e which has been important to the proposal for redefining the SI.

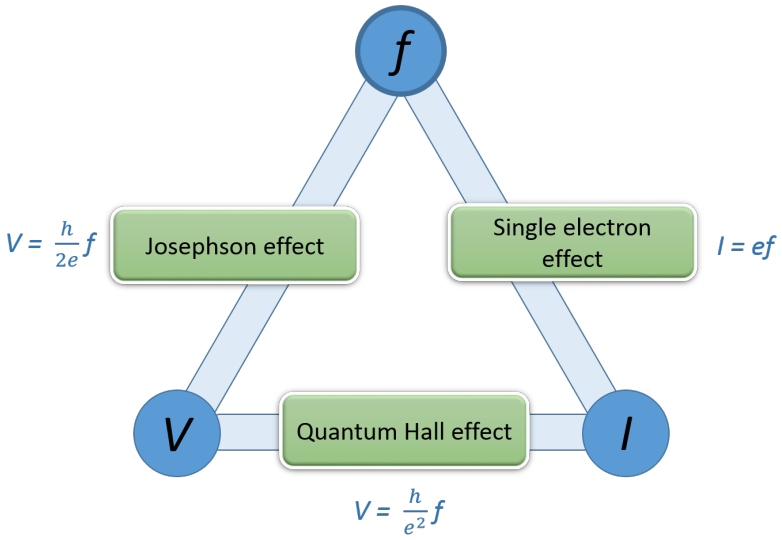

Figure 1.4.: The self-consistency checks that can be performed for all three electrical units if quantum standards are used.

The Josephson effect and quantum Hall effect have been used internationally as representations of the volt and the ohm respectively since 1990 and as such have uncertainties that are suitable for metrology. Current remains to be measured at such a level and complete the triangle, but the method used - of counting or 'pumping' electrons, has made signifi-

cant advances in recent years. All of these experiments require low temperature conditions and the attendendant expertise and expense to run them.

A Josephson junction is formed of two superconductors separated by an insulating barrier. The ac Josephson effect is where a dc superconducting tunnelling current passes across the Josephson junction in the presence of an applied microwave field when the voltage across the barrier satisfies $2eV = nhf$, where f is the frequency of the radiation. Within 10 years of the prediction of the effect in 1962, several countries had agreed on $2e/h$ to keep their voltages in agreement and in 1990 $K_{J-90} = 483759.9$ GHz V^{-1} the frequency-to-voltage ratio was internationally agreed upon [5]. The effect introduced the idea of a quantum standard and then demonstrated its efficacy as experiments have confirmed its value to be independent of material and experimental conditions on the order of parts 10^{16} [5]. It also demonstrated the continued need for international agreement as prior to 1990 even the Josephson volt was found to have a 12 part per million variation across national measurement institutes (NMIs) [7]. Despite this, it quickly demonstrated the drift present in standard cells, and helped to identify stable ones [3]. For the first time it was also possible for other laboratories to adopt this technique, significantly reducing the frequency with which calibration at the NMI has to be performed [4].

The quantum Hall effect manifests in increasing magnetic field as steps in the tranverse Hall voltage, with simultaneous oscillations in the longitudinal voltage such that the minima of the longitudinal coincide with the plateaus of the transverse voltage (fig 1.4). This occurs because the density of states of a two-dimensional material are quantised into discrete levels by the magnetic field and consequently dictate the conductance. The resistance value of the transverse plateaus depends on the fundamental constants h, e and the number of completely filled levels, i: $R_H = \frac{h}{ie^2}$ for semiconductors. The agreed upon value was therefore chosen to be h/e^2 and set: $R_{J-90} = 25812.807557(18)\ \Omega$.

Electron pumps work on the principle of electrostatically isolating electrons and setting barriers such that current flow is achieved through tunnelling. The device bears operational similarity to a transistors and so is often known as a single electron transistor. By creating two such islands and varying the voltage in the gates it is possible to achieve better directional control. The frequency of the gates then dictates the current output: $I = ef$. Although tunnelling is inherently probabilistic, good control can be established: GaAs quantum dot pumps can achieve 50pA with current accuracy of 15×10^{-6} [8] which can be further improved by tailoring the shape of the gate waveform to achieve 150pA with current accuracy 1.2×10^{-6} [9]. The best current accuracy achieved until now is 0.2×10^{-6}

[10]. However in order to complete the triangle, higher current is needed with at least an order of magnitude better accuracy is necessary. The limiting factor appears to be that increasing the frequency further can excite the electron, actually causing a loss of precision.

It is worth briefly mentioning an important piece of equipment used in electrical metrology, the cryogenic current comparator (CCC). It is used to make precise measurements of the quantum Hall and Josephson effects because it allows very low noise operation with small signals as well as having the capability of maintaining exactly the same dc current to two devices simultaneously. The CCC requires liquid helium to work as the priniciple depends on passing two currents in opposite directions inside a superconducting shell. Due to the Meissner effect any magnetic field is expelled outside the shell with the result that the magnetic field sensed out the shell is proportional to the difference of the two currents. This can then be monitored. The one problem with this is that specialised electronics (and operational expertise) required which has severely limited the number of laboratories where it can be found, as at higher signal amplitudes resistance bridges are usually adequate.

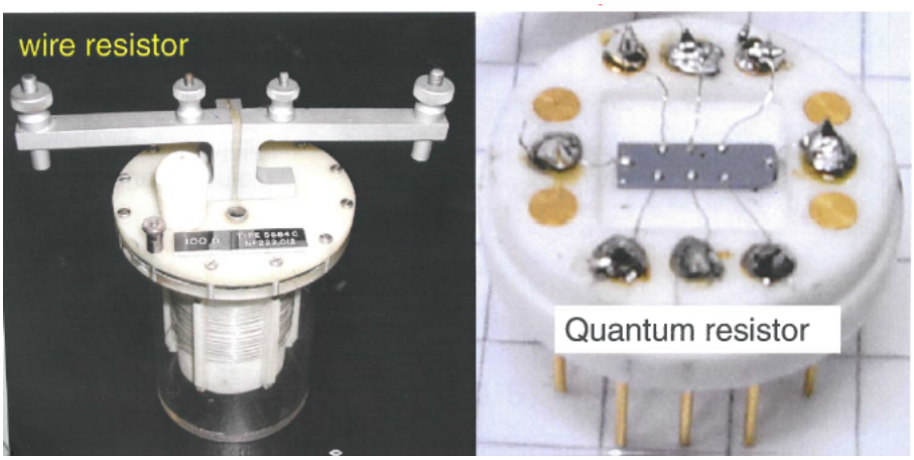

Figure 1.5.: Left: Artifact representation of the ohm - a wire wound resistor. Such standard cells become more stable over time, when maintained in constant conditions. Oil baths are often used to ensure this. Right: A GaAs sample on a ceramic TO-8 header suitable for metrology. The background grids are from squared paper.

1.3. Graphene and the ohm

The quantum Hall effect is the litmus test for two-dimensionality, precisely because its ultimate pre-requisite condition is two-dimensional confinement of carriers. Graphene has no thickness beyond the one layer of atoms that constitute its honeycomb lattice. The charge carriers are massless Dirac fermions, which are relativistic particles, and therefore rather than being governed by the Schrödinger equation, are governed by the Dirac equation. This means that when experiencing a magnetic field the discrete allowed energy levels are not equidistant, like in a harmonic oscillator, with a linear dependence on magnetic field. Instead, the Landau levels are proportional to the square root of magnetic field, which has much greater separation between the lowest energy levels.

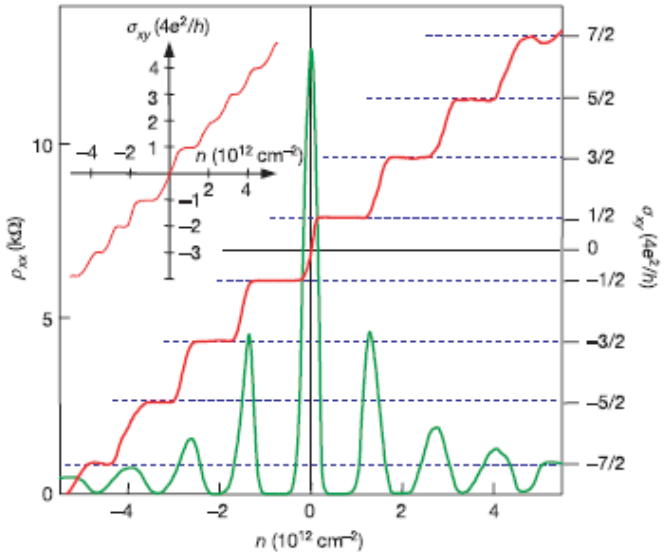

Figure 1.6.: The longitudinal and transverse resistivity for monolayer graphene as demonstrated in the 2005 paper by Novoselov and Geim demonstrating the Dirac fermion nature of the material [11]. The numerical factor governing the fillling factor and distinguishing it from semiconductor 2DEGs is contained in the units on the axis.

The energy separation of the Landau levels sets the conditions necessary to observe the effect in terms of temperature and magnetic field. Any thermal excitation due to temperature must be less than the separation of the levels to allow them to be resolved and the magnetic field has to be large enough to provide sufficient available states for the carrier density to fit into the lowest Landau levels which are the ones with which full quantisation can be seen. The separation is vastly greater in graphene than GaAs heterostructures:

1300K at 10T for graphene vs 200K for GaAs [12]. The wide separation of the Landau levels is most vividly demonstrated in the fact that uniquely for graphene, the quantum Hall effect has been observed at room temperature [13]. Due to the precision required for metrology, room temperature measurement is inadequate, but it illustrates how graphene is able to provide a significant parameter shift.

The first work to show quantisation approaching the metrological level set by 2DEGs was performed on very small flakes of only a few microns in size [14]. The precision achieved for $R_K/2$ was 15 parts per million, in spite of the low critical currents that were achieved. This was significant because it was clear evidence for much higher criticial currents being feasible on marginally wider devices. It also highlighted the importance of contact resistance as the limiting factor for critical current, in particular the variation in resistances for contacts on the same device.

The production of graphene by subliming silicon carbide (SiC), known as epitaxial graphene, was initially hindered by the inherently large carrier density produced. By altering the production technique so that carrier densities were reduced by approximately an order of magnitude, to no greater than 10^{12} cm^{-2}, made it possible to reach the $\nu = 2$ plateau in the magnets typically available in non-specialist laboratories of <18T. Significantly, precision of 3 parts per billion was achieved at 300mK [15] which is an improvement of four orders of magnitude. The use of epitaxial graphene represented a technological advance, with many Hall bars being fabricated onto a SiC wafer with patterned Ti/Au contacts having low contact resistance and devices showing uniform mobility and carrier density throughout the wafer. The robustness of the effect was confirmed by quantisation seen at 4.2K, with precision reduced by one order of magnitude. This was the start of a body of work to understand the material and develop the technology for homogenous, stable devices suited for metrological use that is further explored in later sections and that this project is a part of.

The quantum Hall effect was thought to be universal, and material independence had been verified by comparing different semiconductor heterostructures. The test against epitaxial graphene presented an extra level of rigour because the physics of Dirac fermions is different and gave further support to the basis of the redefinition of the SI. The two devices were measured simultaneously in two separate cryostats with a CCC providing current to each. The relative standard uncertainty of quantisation was determined by the difference in value between the epitaxial graphene and the GaAs, normalised to $R_K/2$, and was found to be 8.7×10^{-11} [16]. This uncertainty is lower than that typically achieved

for semiconductor comparisons of around 2 or 3×10^{-10}. It is of particular importance that the limiting factors in the measurement did not come from the graphene, but the low critical current of the GaAs device and the room temperature resistor used as a transfer standard.

The observation of the quantum Hall effect with 2DEGs requires low temperatures, preferably <1K, and high magnetic fields >10T. This has restricted the number of laboratories, even amongst NMIs [4], that perform quantum Hall experiments due to the equipment necessary to create those conditions being both expensive and requiring expertise to operate [6]. To achieve any reduction in the chain of calibration is clearly beneficial, typically saving one order of magnitude in precision per stage eliminated. Since the successful proliferation of the Josephson volt to industry laboratories [4] getting the primary standard as close to the end user has become a goal of modern metrology [6]. As a result of the fact that the quantum Hall effect in graphene can manifest in low fields and with high precision around 4.2K [17] it is now possible to make this a reality.

The use of a table top cryogen-free cryostat that works with a 0.25W pulse tube cooler achieves 3.8K, and when fitted with a fist-sized 5T magnet removes the expense and difficulty of operation from the measurement of the qunatum Hall effect [6]. A 15 minute measurement yields a precision of 5×10^9 which is reduced by an order of magnitude if performed for over an hour, another benefit of the cryo-free system being that time is no longer limited by helium evaporation.

Work on device optimisation, however continues, not least as samples ideal for traditional low temperature and high field use are not necessary ideal in the new parameter regime, with inhomogeneity being of particular interest due to the low carrier density needed for use in 5T. Contact resistance remains a key issue as high critical current is still required to achieve a good signal-to-noise ratio, and variation of resistance across individual contacts per device is also seen to be detrimental on epitaxial graphene [17]. While annealing the device is found to be effective in reducing contact resistance on flakes [14], contact resistance needs to be addressed at the fabrication stage in epitaxial graphene.

Recent work has shown that without taking some extra steps there is indeed a spread of contact resistance both across the wafer and individual devices, from less than an ohm up to a hundred kilo ohms, with a particular increase in number between one and 10 kilo ohms [12]. It was shown that this is not due to resist residues in the fabrication process as no significant difference could be found by using a a clean fabrication technique that specifically prevents residues being left under the device contacts. Instead it is found

Figure 1.7.: The longitudinal and transverse resistivity for monolayer graphene as demonstrated in the 2005 paper by Novoselov and Geim demonstrating the Dirac fermion nature of the material [11]. The numerical factor governing the fillling factor and distinguishing it from semiconductor 2DEGs is contained in the units on the axis.

that the geometry and position of bilayer inclusions is the primary cause. This can be minimised by using express optical microscopy [18] to exclude use of wafers with >10% bilayer coverage, and orienting devices parallel to the terraces of the SiC substrate where they predominantly occur. Furthermore if there is an inclusion in the voltage probe 'leg', extending the contact to cover and thereby shunt it also helps. This has influenced device design and helped to make a successful prototype of a 100 Hall bar array [19].

Arrays are used in order to cover decades of resistance (or voltage) as part of the calibration process. Parallel connection of many devices allows a higher critical current to be sustained, but homogeneity is the most vital aspect as all the devices need to be quantised at the same field. If non-uniform doping affects some devices in the array, then overall quantisation cannot be achieved. 100 Hall bars on the ν=2 plateau mean that the value of interest is $R_K/200$ which was found with a precision on 10^{-4} [19]. This precision was

limited by the 1% variation in quantisation across the individual devices.

Critical current is therefore not only important to single devices, but to the use of arrays as higher critical current density allows the use of narrower channels, which are then more likely to be uniform across the channel width [19]. There are numerous models pertaining to critical current and the breakdown mechanism that destroys the quantum Hall state, but as it is a complex problem, none as yet which are predictive. Finding one which was predictive would be a great boon, and graphene is an ideal material to explore the topic due to its relative ease of fabrication, robustness and inherently high critical current.

1.4. Summary

The SI was formed of and continued to evolve as a system of coherent units, based on classical laws and put into practise using the best available techniques of the time. There is now an opportunity to redefine the system based on fixed values of fundamental constants. Establishing the viability of this has been an ongoing process, in which electrical metrology has held an significant role, due to the discoveries of quantum phenomena in the second half of the 20^{th} century.

Facilitating the dissemination of primary standards in order to reduce the relative standard uncertainty available to the end user is now coming within reach and poses new technical challenges. Fundamental challenges also remain in understanding the mechanisms behind the limiting factors, including those of the metrological triangle. One of these is the breakdown of the quantum Hall regime due to applying current in excess of a critical value.

Graphene has opened a new avenue of investigation into this effect. This project has, therefore, used several techniques to investigate the material, with a view to gaining insight into this problem.

Part II.

Theoretical and experimental background

2. Graphene

2.1. Electronic band structure

Graphene is a single atom thick sheet of carbon atoms arranged in a honeycomb structure. It is an allotrope of carbon, like diamond, graphite and Buckminster fullerene, but unlike those materials it is a two-dimensional crystal. It was originally isolated from bulk graphite [20], and so has the most in common with it out of the three-dimensional allotropes. However, the electronic bandstructure of graphene has important differences, which result in the exceptional mechanical and electrical properties associated with it.

The successful isolation of graphene using mechanical exfoliation [20] was unexpected, because it had been theoretically stated by Peierls, Landau and Mermin that two-dimensional crystals would be unstable against thermal fluctuations. Work on thin films appeared to strongly support this, with materials losing continuity below a few layers [21].

Nonetheless, graphene had been extensively studied theoretically and its bandstructure was calculated in 1947 [22]. The unique property of graphene is that rather than having conventional electrons and holes, it has so-called Dirac Fermions [11]; massless ones in the case of monolayer and massive ones for bilayer graphene. This arises because the conduction and valence band touch, making graphene a semimetal, or a gapless semiconductor. The touching bands and subsequent Fermi velocity mean the charge carriers are relativistic and as such their energies are better described by the Dirac equation than the Schrödinger equation.

In order to form the graphene sheet the valence structure of carbon: $2s_1 2s_2 2p_2$, is hybridised to $3sp_2p_2$, which allows for three σ bonds and and one π bond to form. The σ bonds form the honeycomb structure and the π bonds are oriented perpendicular to the plane. Hexagonal structures are also seen in aromatic molecules, notably benzene, where it is well known that the ring is formed of slightly unusual covalent bonds which have strength inbetween that of a single and a double covalent bond. This is made possible

by the sp^2 hybridisation, and in graphene makes for a strong and flexible crystal. The π bonds then form the conduction and valence bands.

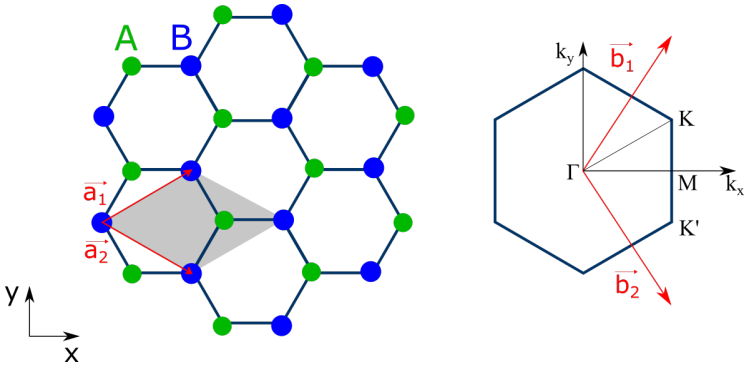

Figure 2.1.: On the left is the real space lattice with the unit cell and its vectors indicated. The triangular sublattices are distinguished by colour and labelled A and B. On the right is momentum space, showing the Brillouin zone with the important symmetry points and the unit cell vectors in reciprocal space. $\vec{a_1} = \frac{a}{2}(3, \sqrt{3})$, $\vec{a_2} = \frac{a}{2}(3, -\sqrt{3})$, $\vec{b_1} = \frac{2\pi}{3a}(1, \sqrt{3})$, $\vec{b_2} = \frac{2\pi}{3a}(1, -\sqrt{3})$. a is the C-C bond length, 1.42Å.

The crystal lattice is composed of two triangular lattices, because a honeycomb structure does not have the translational symmetry required to form a Bravais lattice. This has the result that the unit cell of each sublattice is composed of two atoms which are not adjacent to each other in real space. The hexagonal network is restored by the interlacing of the two triangular sublattices.

The existence of two sublattices has fundamental consequences. It doubles the features of the bandstructure, resulting in six points where the π bands cross on the Brillouin zone. This doubles the number of available states. It also results in chirality for the charge carriers, giving additional confirmation of their Dirac-type nature, and which will be discussed later in this section.

The tight binding model can be used to construct a Hamiltonian to yield the bandstructure of a material, and has the advantage that the wavefunctions used resemble atomic orbitals. The bandstructure demonstrates the dependence of energy on electron momentum, which is a function of its position in the lattice. The dependence of energy on momentum is known as the energy dispersion, $E(\vec{k})$. Due to the large geometric separation of the σ and π bond wavefunctions, and the large energetic separation of the bands they form, the energy and momentum of the charge carriers can be determined by applying the tight binding model to the π electrons only. This will then reveal the linear energy dispersion at low energy excitations that determines the unique behaviour of graphene.

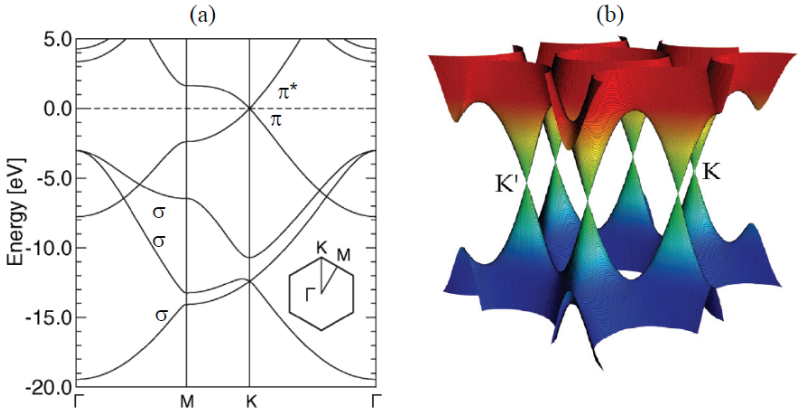

Figure 2.2.: On the left is the bandstructure calculated using the tight binding approach to get the full energy dispersion. From ref.[23]. On the right is a 3D representation of the π bands to show the six Dirac cones forming at the corners of the Brillouin zone. Each sublattice contributes three cones, which alternate around the hexagon, and are distinguished by denoting one set K and the other K'. From ref.[24].

The tight binding approach considers the interaction of a single electron at a lattice site with all other lattice sites. By considering the creation and annihilation of an electron on a lattice site, i, or its neighbours, j, the Hamiltonian can be constucted to include the self-energy of the electron, and it hopping to other sites:

$$\mathcal{H} = \sum_i \epsilon_i c_i^\dagger c_i - \sum_{\langle ij \rangle} \gamma_{ij} c_j^\dagger c_i \tag{2.1}$$

$c_i^\dagger$ and c_i create and annihilate an electron at lattice site $\mathbf{R}_i$.

Due to the repetitive nature of the lattice it is sufficient to consider nearest neighbour atoms, which are however of different sublattice, a and b:

$$\mathcal{H} = \sum_i \epsilon_{p2} a_i^\dagger a_i + \sum_i \epsilon_{p2} b_i^\dagger b_i - \gamma \sum_{\langle ij \rangle} b_j^\dagger a_i + a_j^\dagger b_i \tag{2.2}$$

ϵ_{p2}: self-energy of p2 orbital, γ: hopping amplitude between sublattices

In order to find the dispersion relation, $E(\overrightarrow{k})$ it is necessary to solve the problem in momentum space.

$$H\Psi(\overrightarrow{k}) = E(\overrightarrow{k})\Psi(\overrightarrow{k}) \tag{2.3}$$

In order for there to be a non-trivial solution for a homogenous system, the determinant must be zero. A new matrix, S is used to account for the overlap of adjacent atomic orbitals.

$$\begin{vmatrix} H_{AA}(\overrightarrow{k}) - E(\overrightarrow{k})S_{AA}(\overrightarrow{k}) & H_{AB}(\overrightarrow{k}) - E(\overrightarrow{k})S_{AB}(\overrightarrow{k}) \\ H_{BA}(\overrightarrow{k}) - E(\overrightarrow{k})S_{BA}(\overrightarrow{k}) & H_{BB}(\overrightarrow{k}) - E(\overrightarrow{k})S_{BB}(\overrightarrow{k}) \end{vmatrix} = 0 \tag{2.4}$$

The matrix elements are simplified by the fact that the two sublattices are identical. Matrix elements concerned with interactions only within one sublattice are independent of sublattice index. Elements concerned with interactions between the sublattices but in opposite directions are complex conjugate.

Additionally, if there is no overlap between adjacent atomic wavefunctions, as can be assumed, S becomes the identity matrix yielding a fairly simple form for the dispersion relation:

$$E(\overrightarrow{k})^{\pm} = H_{AA}(\overrightarrow{k}) \mp \left|H_{AB}(\overrightarrow{k})\right| \tag{2.5}$$

The nearest neighbour interaction approximation also renders interactions within sublattices constant, leaving only the matrix elements concerned with inter-sublattice hopping to contribute.

$$E(\overrightarrow{k})^{\pm} = \mp \left|H_{AB}(\overrightarrow{k})\right| \tag{2.6}$$

Solving for $E(\overrightarrow{k})$ gives the bandstructure for the whole Brillouin zone (BZ):

$$E(\overrightarrow{k})^{\pm} = \mp\gamma_0\sqrt{1 + 4\cos^2(k_x a/2) + 4\cos(k_x a/2)\cos(\sqrt{3}k_y a/2)} \tag{2.7}$$

From the bandstructure (eqn.(2.7) and fig.(2.2)) it can be seen that the conductance and valence bands touch at the corners of the BZ, the K points. Due to the low energy at these points, the electrons aggregate here where the energy dispersion is linear, forming so-called 'Dirac cones'. Since each sublattice contributes three Dirac cones, at alternate positions on the BZ, the cones and positions are distinguished by using the notation K

and K'.

Since $\epsilon_k = 0$ at K it means that rather than the states being filled at $\overrightarrow{k} = 0$ they are filled at $\overrightarrow{k}$ defined by the position of K. In this low energy limit the energy dispersion relation can be given as

$$E(\overrightarrow{k}) = \pm\hbar v_F|\overrightarrow{k}| \tag{2.8}$$

In order to see this, the first step is to shift the origin for the energy dispersion to K.

$$\overrightarrow{K} = \left(\frac{4\pi}{3a}, 0\right) \qquad \overrightarrow{K'} = \left(-\frac{4\pi}{3a}, 0\right) \tag{2.9}$$

$(k_x, k_y) \rightarrow (k_x \pm \frac{4\pi}{3a}, k_y)$

If then the momentum is shifted, such that it is now measured with respect to K, and is denoted $\delta\mathbf{k}$ [1] and the de Broglie relation is used, $|\delta\mathbf{p}| = \hbar|\delta\mathbf{k}|$, the effect on expanding the Hamiltonian at K can be seen.

$$H_{K,K'} = -\gamma_0\frac{\sqrt{3}}{2}a\begin{pmatrix}0 & \pm k_x - ik_y\\ \pm k_x + ik_y & 0\end{pmatrix} = v_F|\delta\mathbf{p}|\begin{bmatrix}0 & e^{-i\xi\theta(\delta\mathbf{k})}\\ e^{i\xi\theta(\delta\mathbf{k})} & 0\end{bmatrix} = v_F|\delta\mathbf{p}|\boldsymbol{\sigma}\cdot\delta\hat{\mathbf{p}} \tag{2.10}$$

$\theta(\delta\mathbf{k})$ - angle of $\delta\mathbf{k}$ relative to x-axis

γ_0, the hopping integral limits the range where the linear dispersion holds. But it is also limited at low energy due to reduced screening at low carrier densitites, which then causes the energy spectrum to no longer be linear and give an energy dependent Fermi velocity.

From the Hamiltonian it can be seen that for the energy eigenvalues of a Dirac cone, of either sublattice, can be given by

$$\epsilon_{\delta\mathbf{k}} = \pm v_F|\delta\mathbf{p}| = \frac{\pm 3\gamma a_0}{2}|\delta\mathbf{k}| \tag{2.11}$$

The Fermi velocity, v_f is then given by the prefactors of the Hamiltonian outside the matrix, and corresponds to the slope of the Dirac cone.

[1] $\mathbf{k}$ is the electron momentum like $\overrightarrow{k}$, but can also be considered the momentum with respect to the K point rather than $\overrightarrow{k} = 0$. (As well as having the benefit of being clearer to view in matrices.)

2.1.1. Dirac fermions

The result of the linear energy dispersion at the K points and subsequent move to use the Dirac equation describes charge carriers that do not behave in the same way as electrons (and holes) normally do. This is already seen in the high and constant Fermi velocity and masslessness. However, there is a subtle yet crucial restriction regarding the momentum of the charge carriers which sets Dirac fermions apart, and arises from the symmetry considerations of having two triangular sublattices. This determining characteristic is chirality.

Chirality expresses the property that the mirror image of something is not identical to the original image or object. This is commonly found in molecules, but the most accessible example is our own hands. In fact, the Greek word for hand, *kheir*, is the root of the term. The components and structure of the the left hand and the right hand are the same, but as seen when placed side by side the digits are in reverse order compared to each other. The two are mirror images of each other, but when not mirrored, the images of neither the palms nor the backs of the hands can be superposed onto each other successfully, irrespective of rotation. *Fundamentally, 'chirality' is used to express that two versions of something are not interchangeable, despite having the same structure (or properties).*

Chirality in graphene arises due to the crystal structure and the conservation of a property known as pseudospin. Pseudospin, as a material property, distinguishes electron occupation of the A and B sublattices. It was shown in the construction of the Hamiltonian that contributions from each lattice and hopping between them must be taken into account (eqn. (2.4)). It is then natural that the wavefunction, Ψ which must hold for the whole crystal lattice must have two components in order to account for each sublattice.

However, there is more to pseudospin than a momentary designation of an electron to lattice site A or B. This is best understood by examining the Hamiltonian. The absence of overlap between adjacent atomic wavefunctions, and the nearest neighbour approximation renders interaction between sublattices the only determining factor (eqn (2.6)). In equation (2.10) it is then shown how electron momentum at K relates to crystal momentum and the angle relative to the x-axis. By showing equation below (2.10) in a different format (2.12), it is easier to reveal the pseudospin. σ_x, σ_y are the usual Pauli matrices, but it is the total effect which is important, because the direction of this vector is linked to an axis ($\vec{\boldsymbol{\sigma}} \cdot \vec{\mathbf{n}}$), which is determined by the electronic momentum, because the product of the two is always +1, or -1.

$$H = v\begin{pmatrix} 0 & p_x - ip_y \\ p_x + ip_y & 0 \end{pmatrix} = v\begin{pmatrix} 0 & \pi^+ \\ \pi & 0 \end{pmatrix} = v(\sigma_x p_x + \sigma_y p_y) = v\,\overrightarrow{\boldsymbol{\sigma}}\cdot\overrightarrow{\mathbf{p}} = vp\,\overrightarrow{\boldsymbol{\sigma}}\cdot\overrightarrow{\mathbf{n}} \quad (2.12)$$

The nature and origin of this axis [2] are then made clear by looking at the form of the Hamiltonian which explicitly displays the relation to the angle of the electron momentum along the x-axis.

$$v\begin{pmatrix} 0 & \pi^+ \\ \pi & 0 \end{pmatrix} = vp\begin{pmatrix} 0 & e^{-i\xi\theta(\delta\mathbf{k})} \\ e^{i\xi\theta(\delta\mathbf{k})} & 0 \end{pmatrix} = vp\begin{pmatrix} 0 & e^{-i\varphi} \\ e^{i\varphi} & 0 \end{pmatrix} \quad (2.13)$$

While ξ simply denotes the valley and $\theta(\delta\mathbf{k})$ clearly expresses the relation of electron momentum to the x-axis, the angular dependence can be more simply represented using φ.

Since $E = vp$ this gives

$$\Psi = \begin{pmatrix} \Psi_A \\ \Psi_B \end{pmatrix} = \frac{1}{\sqrt{2}}\begin{pmatrix} e^{-i\varphi/2} \\ e^{i\varphi/2} \end{pmatrix} \quad (2.14)$$

The resulting solution has a familiar form resembling that of electron spin, and hence is known as a spinor. This spin-like description is the reason this material property has been given the name 'pseudospin'.

It follows from consideration of the crystal that having occupation of only sublattice A or B is non-physical. So, the two-component wavefunction has a form appropriate to show the sharing of the electron density across both sublattices.

$|\downarrow\rangle, |\uparrow\rangle$ are a more spin-like way to represent sublattices A and B

$$|\Psi_\pm\rangle = \pm\frac{1}{\sqrt{2}}\left(\,|\uparrow\rangle \pm e^{i\varphi/2}\,|\downarrow\rangle\,\right) \quad (2.15)$$

In this way it is clear that chirality in graphene is a relative phase in the two-component wavefunction [25]. However, it is not having a specific vector to describe this wavefunction that is is significant, but that it is locked to direction of electron momentum.

This has significant consequences for scattering, most notably in the suppression of backscattering, which affects the behaviour of p-n junctions [26] and had unexpected consequences

[2] $\overrightarrow{\mathbf{n}}$ is used in (2.12) to emphasise the presence of an axis. $\delta\hat{\mathbf{p}}$ in (2.10) is equivalent, but the notation is chosen to emphasise the link through the de Broglie relation to $\overrightarrow{k}$.

for weak localisation (ch4).

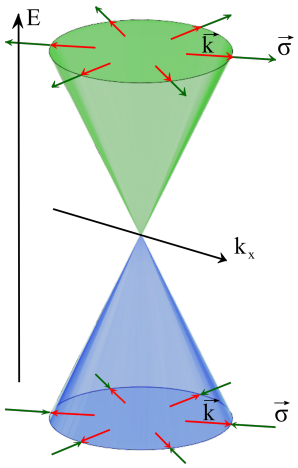

Figure 2.3.: For the K points the π^* bands have pseudospin parallel to the electron momentum, and π bands with pseudospin antiparallel to the electron momentum. This is reversed for the K' points.

It is difficult to probe the chiral nature of Dirac fermions, but it is relevant in optical transitions [27] and light polarisation is uniquely suited to probing it. This also means that ARPES with circularly polarised light can directly provide information on the pseudospin in its sense as the phase relation of the wavefunction. The angular offset can even provide information on the intial state [28]. Equations (2.12) and (2.13) include Hamiltonians to relate the π, π^* bands (probed by ARPES) to the pseudospin.

Figure 2.4 shows that the different branches of the Dirac cone are selectively excited by photons with different helicity. Helicity describes the locking of particle spin to its momentum direction. Its most well known example is that of neutrinos, which are inherently left- or right- handed. Helicity and chirality are the same for massless particles. Despite having quasiparticles, helicity proves to be a good quantum number for graphene too.

In terms of transport, it has been recently shown that chiral tunnelling is possible between two sheets of graphene which are vertically separated by boron nitride. Having a small misalignment of the two sheets creates a large pseudo-magnetic field, which aligns the Dirac cones and allows a tunnel current to pass [29].

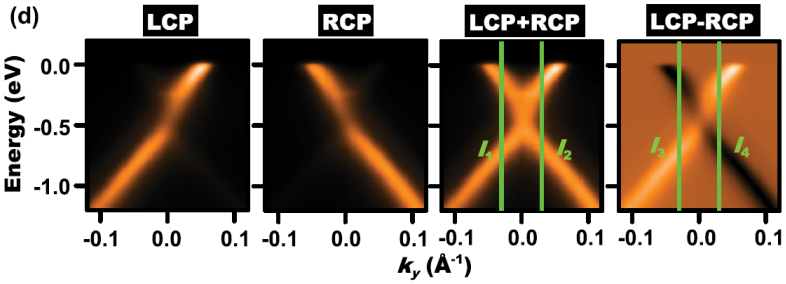

Figure 2.4.: Left circular polarisation (LCP) and right circular polarisation (RCP), sum and difference.

2.2. Graphene fabrication

There are numerous methods by which graphene can be fabricated. It was first isolated by mechanical exfoliation [20] also known as the 'scotch tape' method [30], which produces flakes of high quality material, but since the flakes are only of micron size this method is unsuited to mass production. A large scale production process with relatively low entry costs is chemical vapour deposition (CVD) which can producevery large areas of graphene; even 30 inch roll to roll production [31]. The limiting factor in the quality of CVD graphene is the crystallinity of the metal substrate being deposited on. imperfections can result in grain boundaries in the final graphene, often with domains of different layer number. A newer method also suited to large scale production is liquid phase exfoliation (LPE) however this is still lagging behind in terms of quality control [32, 33].

For this work epitaxial graphene was used. This method builds on existing wafer scale technology, and as such is compatible with the mass production methods familiar in semiconductor technologies. It allows for large area devices of monolayer graphene, which makes it well suited for the fabrication of Hall bars for metrological purposes.

2.2.1. Layer identification

There is now a well established body of work around several techniques including Raman spectroscopy [34], ARPES [35], and LEED [36, 37] for quantifying the number of layers present. These techniques are effective on epitaxial graphene, as is of course the quantum Hall effect which is the ultimate test for establishing a material as two dimensional. Leaving aside the quantum Hall effect, due to some differences arising from the substrate

and its relation to the graphene in epitaxial graphene, additional work has taken place to optimise these techniques.

Recent work [38] has made it possible to use the fastest technique, optical micorscopy to identify and enumerate graphene layers on epitaxial graphene, and even establish micron scale characterisation. The silicon substrate that flakes are transferred onto typically has an oxide layer present on its surface giving a refraction coefficient that results in sufficient contrast to make the flake visible to simple optical microsopy [39]. The refraction index of silicon carbide is 2.65 which does not provide sufficient contrast. However in the same manner that it was possible to optimise finding flakes for different oxide thicknesses by using different wavelengths of light and filters [39], recent work using transmission as well as reflection mode, and real time software processing, has provided an effective alternative using optical microscopy [38], and, confocal microscopy can also be effective.

2.3. Epitaxial graphene

Epitaxial graphene is distinct from other fabrication methods in that it is not a transferred sheet of material that has been previously isolated [40]. The most common method for producing epitaxial graphene is the sublimation of silicon out of silicon carbide wafers [40].

Silicon carbide is formed of equal parts silicon and carbon, stacked in layers of atoms bonded in a tetrahedral structure (with each atom bonded to four of the other element). The stacking of the layers in parallel and antiparallel combinations results in many polytypes [41]. The stacking sequences also give rise to different crystal symmetries, which together with the number of layers within a sequence is used to designate each polytype [42]. The symmetries are H - hexagonal, R - rhombohedral and C - cubic. There are 215 recorded polytypes [43] of which three are widely available and therefore of greatest interest: 6H, 4H and 3C. The graphene used in this thesis was sublimed from 4H-SiC(0001) at 2000°C in 1 atm argon.

The growth kinetics of the epitaxial method are non-trivial and achieving controlled growth has required investigation [44]. The structure of silicon carbide means that one side of a wafer has silicon on the surface, while the other has carbon. The Si-face has slower sublimation which also appears to be partly self-limiting [45, 46] allowing easier production of single or bilayer graphene than on the C-face which typical grows more layers and with

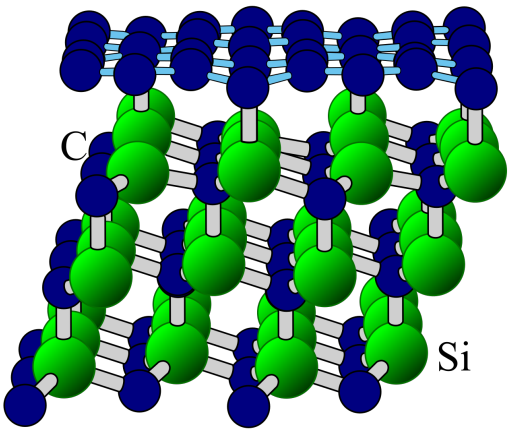

Figure 2.5.: Diagram of three parallel layers of tetrahedrally bonded silicon carbide terminated on the silicon face, with partially reconstructed carbon on top known as the interfacial (or buffer) layer. The bonds between these carbon atoms and the top silicon are incomplete, "dangling" covalent bonds. It is the next sheet of carbon which is the fully formed graphene sheet.

less homogeneity [47].

The cut wafers reveal the tree trunk-like grain of silicon and carbon layers. It is found that the growth nucleates along these edges [48], also known as terraces or step edges, but the rearrangement of carbon atoms to form the honeycomb lattice produces a continuous layer of carbon formed over these steps. Nonetheless there are often patches of bilayer to be found on otherwise single layer material, even on the Si-face of the material. As this graphene is grown in a process that relies on the removal of silicon from the surface, the bilayer can be found underneath the monolayer sheet.

However, the sublimation of the silicon carbide results in an "interfacial layer" of incomplete covalent bonds between the substrate and the graphene on the silicon face of the wafer (fig.2.5).

It has been established that the interfacial layer is not graphene [36, 49], and so a "monolayer" of epitaxial graphene on the Si face consists of one continous carbon sheet connected by dangling bonds to the SiC substrate (fig.2.6).

This layer gives rise to some differences with respect to transferred graphene materials. The main consequence of the interfacial layer is to facilitate charge transfer from the silicon carbide to the graphene. The charge transfer is strong as it is driven by the work function difference of about 1eV. This results in high electron densities in the as grown material,

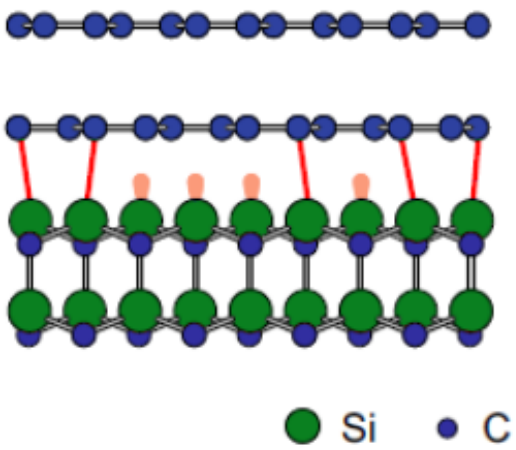

Figure 2.6.: Side view schematic of epitaxially grown monolayer graphene on the silicon face, with the partially covalently bonded interfacial layer beneath the continuous sheet held on by only van der Waals forces.

($n \sim 10^{13}$ cm^{-2}) and pins the Fermi level of the graphene to the charge reservoir in the substrate [50].

The pinning of the Fermi level turns out to be beneficial for metrological purposes as it allows the ν=2 plateau to be accessed easily and makes the plateau very long, that extends to all measurable fields (up to 30T [51]), due to ongoing charge transfer [52, 51].

The n-doping poses a challenge because the magnetic field at which quantum Hall plateaus are observed is proportional to carrier density. As such it determines whether the quantum resistance standard can be determined in a typically equipped cryostat of less than 20T.

New techniques have had to be developed to reduce the carrier density by approximately an order of magnitude, because the coupling to the substrate prevents the use of electrostatic gating of the carrier density [50].

3. Quantum corrections to transport

3.1. The Drude model

The Drude model gives the simplest description of electron transport, treating it as a series of collisions, by otherwise non-interacting electrons with the ion cores. The collisions result in a change in velocity, so that the rate of change of momentum can be described due to the acceleration by the electric field, $\mathbf{E}$ and magnetic field, $\mathbf{B}$, if present, and the reduction by collisions. There is given probability of collision per unit time, so collisions are quantified by a scattering time, which represents the average time between their occurrence, τ.

$$m\frac{d\mathbf{v}}{dt} = -e\mathbf{E} - e\mathbf{v}\times\mathbf{B} - \frac{m\mathbf{v}}{\tau} \tag{3.1}$$

The electrons do not interact with each other between collisions, so all energy loss is through collisions with the cores. This loss of energy makes the scattering term like a friction term in the equation of motion (3.1).

In the absence of a magnetic field the particle is accelerated linearly. A magnetic force would deflect it, so solving for the equilibrium solutions, when $\frac{d\mathbf{v}}{dt} = 0$, grouping it with the friction force makes physical sense as well as keeping variable separation.

$$\mathbf{v} + \frac{e\tau}{m}\mathbf{v}\times\mathbf{B} = -\frac{e\tau}{m}\mathbf{E} \tag{3.2}$$

Having transport in more than one direction, i.e. in a magnetic field, requires matrix representation. Here ω_B is the cyclotron frequency eB/m and $\mathbf{J} = -nev$ is the current density.

$$\begin{pmatrix} 1 & \omega_B\tau \\ -\omega_B\tau & 1 \end{pmatrix}\mathbf{J} = \frac{e\tau}{m}\mathbf{E} \tag{3.3}$$

Inverting the matrix gives Ohm's law in tensor form, described by the conductivity, σ:

$$\mathbf{J} = \sigma \mathbf{E} \qquad \sigma = \begin{pmatrix} \sigma_{xx} & \sigma_{xy} \\ -\sigma_{xy} & \sigma_{xx} \end{pmatrix} \tag{3.4}$$

Solving for the simplest case, i.e. without magnetic field gives $\sigma_{B=0} = \frac{ne^2\tau}{m}$, as given by the diagonal terms. Often the resistivity, ρ is used to describe transport because it can be more pertinent to the measured quantity of an experiment.

$$\rho = \sigma^{-1} = \begin{pmatrix} \rho_{xx} & \rho_{xy} \\ -\rho_{xy} & \rho_{yy} \end{pmatrix} \tag{3.5}$$

Since the off-diagonal terms contain the effect of the magnetic field, they describe the Hall effect, explored in a later chapter. As off-diagonal terms they do not depend on scattering, which means they can reveal fundamental information about the material.

The total scattering time can have multiple contributing components from different sources as per Mattheissen's rule: $\tau_{Total}^{-1} = \tau_{Impurities}^{-1} + \tau_{Defects}^{-1} + \tau_{electron-phonon}^{-1}$. Scattering sources inherent to the sample, such as impurities and defects form a 'residual resisitivity' which limits the resistivity of real metals at low temperature. This is demonstrated in figure (3.1), together with a quantum correction that can occur at sufficiently low temperatures.

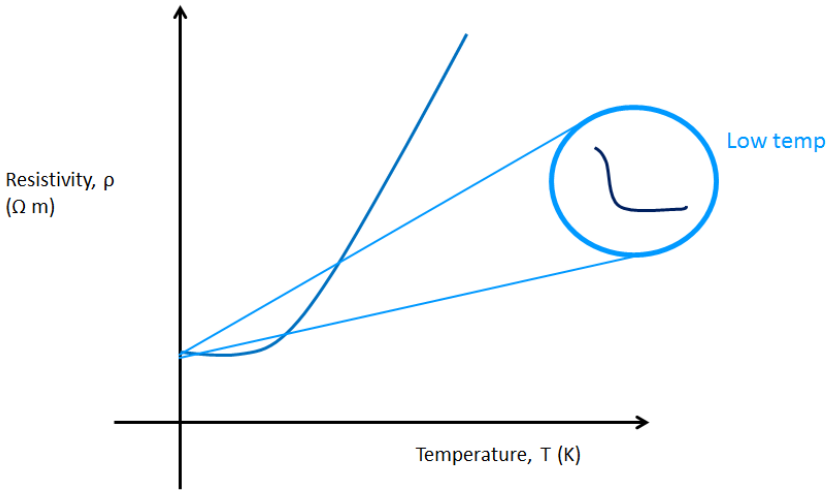

Figure 3.1.: Diagram showing the typical dependence of resisitivity on temperature, with the quantum correction at low temperature magnified.

The transition from the linear temperature dependence to the residual resistivity can be described by the Block-Grüneisen formula. Different interactions can dominate this region which correspond to different values of the integer index in the formula, such as electron-electron, electron-phonon.

3.2. Weak localisation

Weak localisation (WL) is a quantum correction to the Drude conductivity in the region where the temperature is sufficiently low for impurity scaterring to dominate.

The correction is an increase in resistance due to increased backscattering. This occurs because the temperature is sufficiently low for a statistically significant number of carriers to reverse direction after a series of scattering events on defects and impurities (fig.3.2).

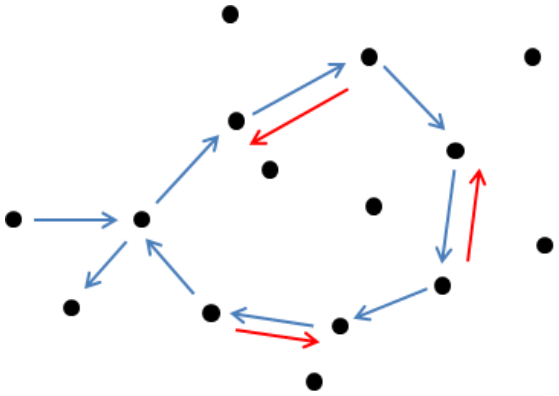

Figure 3.2.: The electron traces a loop of scattering events, exiting where it entered.

Experimentally the correction can be observed by measuring resistance while varying temperature (fig.3.1), but, an experimentally more efficient method is to fix the temperature and apply a magnetic field perpendicular to the sample. This produces the characteristic graphs of weak localisation "peaks" that show the suppression of the effect, through decoherence caused by time reversal symmetry breaking, as the magnetic field is increased (fig.3.3).

WL arises from scattering events that form closed trajectories. However, the subsequent increase in backscattering does not create a correction to the conductivity that is classical

in nature, because when two electrons traverse the same loop in opposite directions their wavefunctions intefere.

In the absence of magnetic field the two electrons will have the same phase and the interference will be constructive at the entry/exit point of the loop.

In the presence of a magnetic field, time reversal symmetry is lost, because the potential associated with travelling the loop in opposite directions is no longer the same, which results in slightly different phases for the two electons, decreasing the probability amplitude total.

As the field is increased the degree of dephasing increases and the weak localisation correction is suppressed. This produces a magnetoconductance, or magnetoresistance, curve that allows the size of the effect to be studied.

For metals in zero magnetic field negative magnetoconductance (a peak in resistance) is to expected i.e. WL, with inelastic scattering processes contributing to the suppression of weak localisation [53] because those are the processes which alter phase and therefore cause decoherence. Conversely, in graphene, positive magnetoconductance - weak antilocalisation (WAL) is expected. In metals this is due to spin-orbit coupling and is usually seen as a dip at zero field atop a peak, rather than the usual full peak.

3.3. Weak (anti-)localisation in graphene

Both WL and WAL have been observed experimentally in graphene [54], but in epitaxial graphene WL is consistently observed. The presence of the WL is now understood as an effect of intervalley scattering restoring WL [55] where without it WAL dictated by the crystal structure of graphene would dominate [**?**].

3.3.1. Weak antilocalisation predicted for honeycomb lattices

In graphene the spin-orbit coupling is expected to be weak based on carbon having a low atomic number, but there is an additional phase shift of π that arises from having two constituent sublattices in the Bravais lattice, which means that the sum of the amplitudes should yield destructive interference i.e weak antilocalisation.

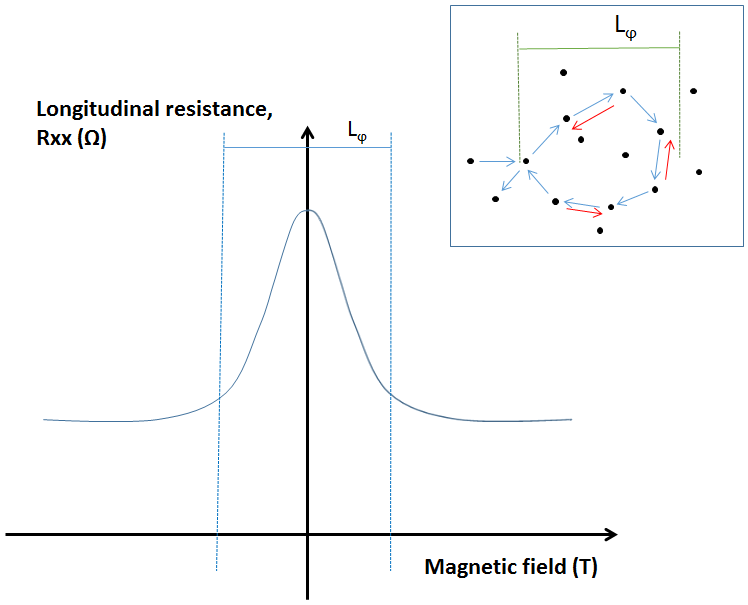

Figure 3.3.: Varying the magnetic field at a fixed temperature produces the characteristic graphs of weak localisation "peaks" that show the suppression of the effect due to decoherence as the magnetic field is increased. Fitting the curve allows the phase coherence length to de extracted, as well as elasic scattering times.

Having two sublattices means that there are two 'valleys' in which transport can take place [56]. Often it is enough to consider only one valley to understand behaviours. However the two sublattices in graphene result in a property analogous to electron spin known as 'pseudospin', whereby the wavefunction contains two components: "up" and "down", as is the case for spin 1/2 particles [56]. This results in chiral quasiparticles, with the pseudospin of each either parallel or antiparallel to the direction of its momentum [56]. This means that according to Ando et al.[57] graphene should show weak antilocalisation because backscattering by long range potentials is not allowed under pseudospin conservation [57].

3.3.2. Restoration of weak localisation in graphene

Further work, specifically for graphene, by McCann et al. showed that WL can be restored in graphene by scattering that mixes quasiparticles of different chirality together [55]. A complex picture emerges, because the chiral nature of the carriers means that elastic scattering also contributes to suppression of weak localisation processes [55].

The ratios of the different scattering types determine the shape of the quantum correction and even the sign of it, with the crossover from WL to WAL was demonstrated by Tikhonenko et al. in graphene flakes [54].

The scattering processes can be examined by fitting the weak localisation peak to the equation by McCann et al [55]. For the case when magnetoresistance is being measured the relation is the following:

$$\Delta\rho(B) = -\frac{e^2\rho^2}{\pi h}\left[F\left(\frac{B}{B_\phi}\right) - F\left(\frac{B}{B_\phi + 2B_i}\right) - 2F\left(\frac{B}{B_\phi + B_*}\right)\right] \tag{3.6}$$

with $F(z) = ln(z) + \Psi(\frac{1}{2} + \frac{1}{z})$.

Fitting allows the different scattering times to be extracted using the relations $\tau_\phi, i, * = \frac{\hbar}{4De}B^{-1}_{\phi,i,*}$.

Generally it is conceptually easier to consider scattering rates - the collisions per second, but in the case of the phase coherence time, τ_ϕ, consideration of the time and also the phase coherence length, L_ϕ, is instructive because these parameters give physical shape to the phase coherent quantum correction being examined.

The first term gives the phase coherence time, τ_ϕ and therefore also the phase coherence length, L_ϕ, which describe the amount of time, or distance travelled respectively, before the electron scatters so as to exit the self-intersecting path as shown in figure 3.2.

Figure 3.3 and the equation above (3.6) demonstrate that the phase coherence time determines the magnitude of the weak localisation peak. It is inelastic scattering processes which affect this parameter, like the static magnetic field used to aquire the magnetoresistance curve.

The second and third terms in the equation encompass the elastic scattering contributions.

τ_*^{-1} is the intravalley scattering rate. There are several potential contributions to the intravalley scattering rate. One can be directly related to 'atomically sharp' defects, τ_s^{-1} which also includes ripples and dislocations that result in chirality being broken [58]. The other, τ_w^{-1} is 'trigonal warping' which is the anisotropy of the Fermi surface in k-space [58].

τ_i^{-1} is the intervalley scattering rate, which is usually attributed to defects on the scale of the lattice spacing, a, such as edges and atomic defects. Intervalley scattering restores WL as chirality is reversed between the two valleys which allows for zero phase difference between two self-intersecting paths. This negates the chirality breaking and trigonal warping effects that suppress intravalley WL [58] and also WAL.

Any WAL contribution is from the second and third terms, but it only manifests if the ratios τ_ϕ/τ_* and τ_ϕ/τ_i are small. This is found by examining equation (3.6) but in the form of magnetoconductance, in the small field limit [54].

3.4. Electron- electron interaction

The contributions to the conductivity are summarised in equation (3.7).

$$\rho_{xx} = \rho_{xx} + \Delta\rho_{WL} + \Delta\rho_{e-e} \tag{3.7}$$

WL is not the only correction: the linear dependence of conductivity on carrier density in graphene indicates dominance of scattering from Coulomb impurities [59], which in turn is indicative of electron-electron interaction (EEI) being present in the system [60]. The carrier density cannot be readily varied in epitaxial graphene so cannot be used to investigate EEI [59].

The work done by Lara-Avila *et al.* [59] not only extracted the scattering parameters for epitaxial graphene, but also determined the Fermi liquid nature of this epitaxial graphene by the strength of the electron-electron interaction which showed that the system was in agreement with Aronov-Altshuler theory.

3.4.1. Aronov-Altshuler theory

The conductivity tensor reveals that the longitudinal conductivity does not stay constant and so in [59] it was possible using

$$\frac{\Delta R_H}{R_H} = \gamma \frac{\Delta R_{xx}}{R_{xx}} \tag{3.8}$$

to determine the presence of electron-electron scattering (the case when γ=2). The logarithmic temperature dependence of σ_{xx} allowed the strength of the interaction and the

Fermi liquid constant to be determined confirming epitaxial graphene as a disordered Fermi liquid.

3.5. Effect of additional inelastic scattering

Equation (3.6) describes the shape of the weak localisation peak as determined by elastic scattering from different sources in a magnetic field. However, any type of inelastic scattering would also be a source of decoherence. While the effect of a dc magnetic field has been widely studied, the effect of a varying electromagnetic field has been less so. Theoretically a distinct shift in magnetoconductance is predicted, and the extra conductivity correction is called "dynamic dephasing" [61]. Dynamic dephasing has been observed in some experimental work done on conventional 2DEGS [62].

High frequency applications of graphene are widely sought, and such applications could be impacted such a correction, particularly in astronomy where low temperature detectors are used.

Although the original work demonstrated a shift, it could not be known what magnitude of effect might be seen in exposing a graphene sample to high frequency electromagnetic radiation, or what other contributions there may be particularly in terms of heating. Graphene was already known to have unique heat conducting properties, which made studying this source of decoherence in graphene of particular interest, as it had not been previously explored.

3.5.1. Dynamic dephasing

Dynamic dephasing is the suppression of weak localisation by exposing the sample to a quickly varying electromagnetic field e.g.microwaves, which then directly interacts with the electron causing scattering. The resulting correction has been observed in silicon metal-insulator-semiconductor (Si-MOS) transistors [62] and magnesium thin film [63].

To arrive at the quantum correction to conductivity for a high frequency electromagnetic field, E_Ω, the conductivity is treated by using a cooperon to represent the fields involved [61] and yields the relation below [62]:

$$\delta\sigma(E_\Omega) = -\sigma_0 \int_{\Omega\tau}^{\infty} \frac{dx \exp(-2x/x_\phi)}{(2/\xi)\sinh(x\xi/2)} \exp(-\alpha B(x)) I_0(\alpha B(x)) \tag{3.9}$$

where $B(x) = x[1 + \frac{1-\xi^2}{1+\xi^2}\frac{\sin x}{x} - \frac{4\xi}{1+\xi^2}\frac{\sin(x/2)^2}{x\tanh(\xi x/2)}]$, I_0 is a modified Bessel function, D is the diffusion coefficient, τ is the momentum relaxation time, and τ_ϕ is the phase relaxation time, with $x_\phi = \Omega\tau_\phi$ and similarly $x = \Omega\tau$. Additionally, $\sigma_0 = e^2/2\pi^2\hbar$, $\alpha = 2De^2E_\Omega^2/\Omega^3(1+\xi^2)$, and $\xi = 8DeH/\Omega c$ is the term arrived at for ξ which accounts for the electric and magnetic field of the microwaves in calculation.

The suppression represented in (3.9) is additional to that caused by temperature, and any magnetic field present [62].

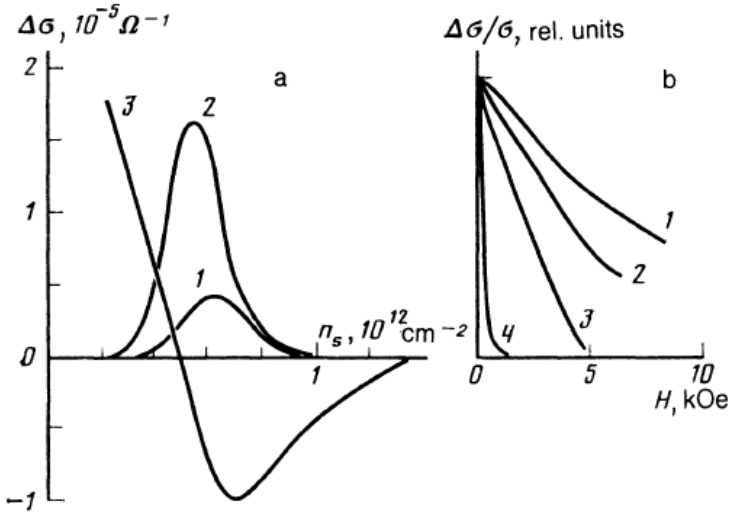

Figure 3.4.: Low carrier density findings, graphs from [62]. Left image: Dependence of correction to conductivity on carrier density at T=4.2K, 9.1 GHz at powers of 29,15 and 0dB for curves 1 to 3. Right image: Normalised conductivity correction in magnetic field with 1 n_s : $7.7 \times 10^{11}\text{cm}^{-2}$ and curve $4n_s$: $9.8 \times 10^{11}\text{cm}^{-2}$.

In the Si-MOS system at high powers it was found that at zero field there was a significant change in conductance for high frequency excitation, which was markedly bigger than that at lower frequency (37 GHz rather than 9 GHz) excitation. Calculations showed that this was due both to heating and a dynamic dephasing component at high carrier density.

At low carrier density and low power it was possible to observe a correction that only had

a dynamic component even at the lower frequency. The resulting correction was found to have a maximum in carrier density that varied with power (fig.3.4 left), but importantly was found to diminish almost linearly with increased magnetic field. The suppression of the dynamic correction by field was also much stronger with higher magnetic field, as shown in figure 3.4 right, curve 1 has n_s: 7.7×10^{11} cm^{-2} and curve 4 n_s: 9.8×10^{11} cm^{-2}.

4. Hot electrons

The current that can be passed in the quantum Hall state before the longitudinal resistance becomes non-zero is known as the breakdown current, I_c. The breakdown current affects the ultimate precision with which the resistance quantum can be determined, primarily because higher signal to noise ratio can be achieved.

The breakdown current is affected by the energy loss rate of the carriers, and the cyclotron energy, which in graphene combine to give higher breakdown currents than traditional 2DEGs [64].

In this instance the energy loss rate, P refers to the situation where the electrons have a higher effective temperature, T_e than the lattice (T_L) due to fast thermalisation by electron-electron collisions. This can become the case where a current is applied such that the carriers are heated faster than they can lose energy [65] and results in a Fermi-Dirac distribution of 'hot' electrons while the lattice remains in equilibirum with the surroundings [66]. P is then a measure of the rate by which the hot electrons lose energy via the electron-phonon interaction.

The decoupled nature of a hot electron system from its surroundings renders usual thermometry techniques unable to determine the real the temperature of the process being examined, which is often of crucial importance. However, there are transport measurements which are able to extract the electron temperature, such as Johnson noise measurements [67, 68] and, establishing the damping of the amplitude of Shubnikov de Haas oscillations.

Optical excitation, both pulsed or continuous (cw) also creates a population of hot electrons which can be extracted using pump-probe measurements both at room temperature and low temperature. However at low temperature it is usually the subsequent effect on transport that is of interest, which can be investigated by looking at photo- or thermoelectric currents [69]. This is not always practical for reasons of device design or instrumentation, and there are situations, such as low carrier density, where examination of SdH

oscillations is also impractical.

Fortunately for magnetotransport, the strong temperature dependence of weak localisation means that WL is also a good measure of electron temperature and in graphene it has been shown to consistent with the widely used SdH technique [70].

4.1. WL compared to SdH as measure of electron temperature

The effective temperature of these hot electrons, T_e, has traditionally been determined by applying the Lifshitz-Kosevich formula (4.1) to Shubnikov-de Haas (SdH) oscillations. The formula is derived from the free energy in terms of magnetisation and so corresponds to the maximla and minimal energies in the Fermi surface. The SdH oscillation amplitude is reduced with increasing temperature and the reduction in amplidtude normalised by the original amplitude has an $x/sinhx$ dependence.

$$\frac{\Delta\rho}{\rho} = f(\omega_c\tau)\frac{\chi}{sinh\chi}exp\left(-\frac{\pi}{\omega_c\tau_q}\right) \tag{4.1}$$

where $\chi = \frac{2\pi^2 k_b T_e}{\hbar\omega_c}$ contains the effective temperature term to be extracted.

The SdH method requires a high carrier concentration [70] which already makes it unsuited for use with epitaxial graphene, but this is even more the case because the Fermi level is pinned due to substrate effects [59] and so there are not the many oscillations needed for fitting.

The low carrier density alternative is to use the WL peak to make a direct comparison of peak height when suppressed by bath temperature and when suppressed by current heating to determine an effective temperature. This is complemented by comparing the SdH amplitude suppression by current and by temperature. In the case of Joule heating the energy loss rate per carrier is then $P = I^2 R_{xx}/nA$. The equivalence of these two methods was established [70] using CVD and epitaxial graphene (with the former having the high carrier concentration necessary for the SdH method and the latter having pronounced WL behaviour).

The temperature dependence of the energy loss rate then gives further basis for comparison between the two methods, but also between two samples or excitation systems.

A characteristic parameter can be found using the effective temperature and energy loss

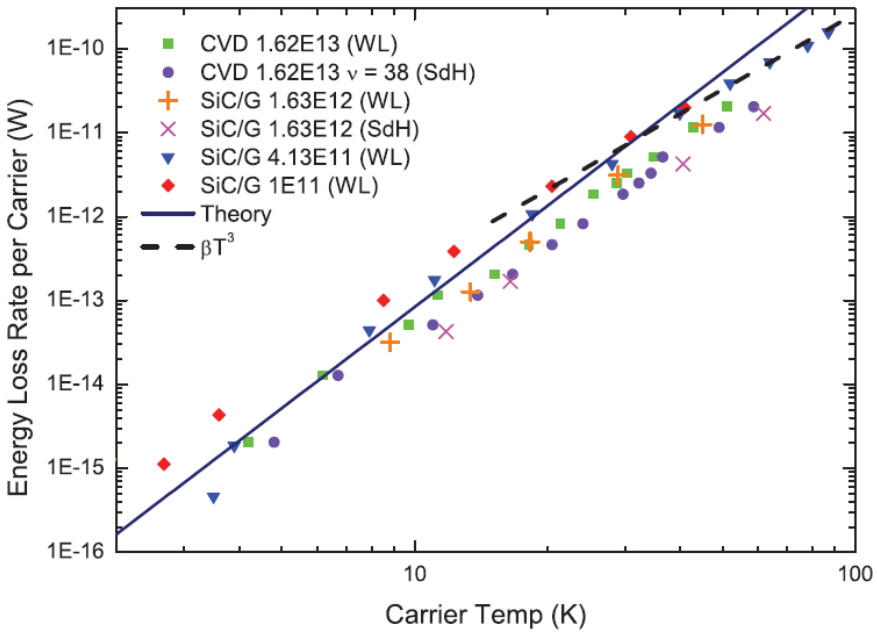

Figure 4.1.: WL and SdH ampltiude measurement of electron temperature are very different techniques, but extraction of the energy loss rate per carrier shows them to be equivalent.Image from [70].

rate, the energy relaxation time, τ_e by applying the following relation [70, 64, 71]

$$\tau_{\mathrm{e}} = \frac{\pi^2 k_b^2 T_e^2}{3E_F P} = \frac{\pi^2 k_b^2 T_e^2}{3E_F \alpha (T_e^3 - T_L^3)} \tag{4.2}$$

where T_e is the effective electron temperature as determined from the weak localisation peak and T_L is the average lattice temperature based on measurements of the bath temperature. P is the energy loss rate per carrier, and its form is determined by the excitation the system is subjected to. For current heating $P = I^2R/nA$ and for microwave excitation $P = \gamma M/nA$ where γ is the coupling coefficient of that frequency of microwave to the sample. α is a coefficient that describes the energy transfer from the heated electrons to the lattice and is material dependent.

τ_e becomes an important parameter in evaluating the system under excitation for comparison with other scattering times such as τ_ϕ, and also the period of any radiation.

4.1.1. Temperature dependence of energy loss rate

In equation (4.2) there is a T^3 dependence. This may not seem unusual because in traditional 2DEGs there is usually a region where resistivity has a cubic dependence on temperature, and it is often viewed as a transition region between the linear high temperature region and the T^5 low temperature Bloch limit [72]. However in graphene the Fermi surface is small, so the expected temperature dependence is T^4 at low temperature, due to the reduced phase space for phonons to scatter electrons [73].

This also means that the Debye temperature, T_D the temperature below which phonon effects manifest is not the parameter of interest. Instead it is the Bloch-Grüneisen temperature, T_{BG} the temperature at which the phonon states can still scatter to everywhere on the graphene Fermi surface [74]. It is a common distinction between metals and 2DEGs for T_{BG} to become the relevant parameter for reasons of reduced dimensionality, as the relation between Brillouin zone size and Fermi surface is the dominant factor. The Debye approximation assumes constant speed of sound and inherently overlooks features in the density of states. This assumption results in high values of T_D for elements with many valence electrons and high elastic moduli; graphene's is particularly high at 2300K [73].

However graphene has been shown to have fast thermal relaxation which is not accounted for by T^4 dependence, particularly at high phonon temperatures [67]. The T^3 dependence observed is explained by three body collisions between carriers and phonons called 'supercollisions'. These can occur when there is disorder in the system which relaxes the momentum conservation conditions [67].

5. The quantum Hall effect

An electron in a magnetic field experiences the Lorentz force, which causes its otherwise linear acceleration by the electric field to be deflected and tend toward circular motion. In the case where a sample is carrying current, with the magnetic field applied perpendicular to the surface of the sample, the force on the electron will be orthogonal to both and will lead to the accumulation of charge on that edge of the sample. The accumulated charge creates a potential difference across the sample, transverse to the current direction, and establishes an electric field. This is the classical Hall effect, as discovered by Edwin Hall in 1879. The measured transverse voltage, the Hall voltage, V_H and corresponding transverse electric 'Hall' field, E_H are named after him.

In the low magnetic field regime the longitudinal and transverse voltages are considered largely independent of each other. Since the Hall field is determined by the accumulated charge, it makes for a good intrinsic measure of the number of carriers, and also of their type through the sign of the voltage, which is particularly useful with semiconductors where the majority carrier may be holes.

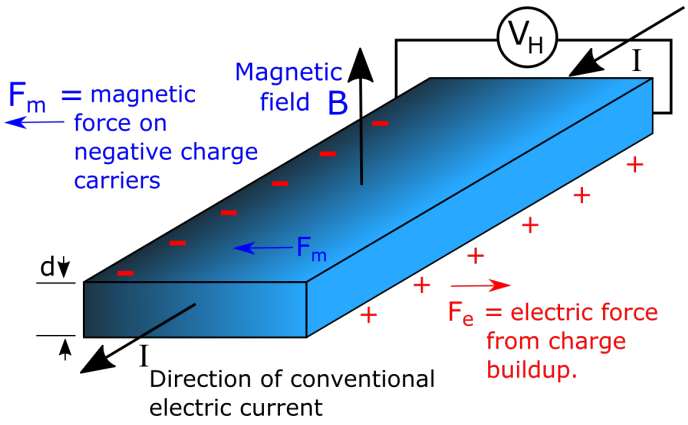

Figure 5.1.: The Hall effect arises from the deflection of charge carriers by the Lorentz force when an electric field and magnetic field are applied orthogonally to a material. The accumulated charge creates a transverse electric, 'Hall' field.

As the magnetic field is increased it disrupts the density of states which can be observed when the temperature is low compared to the energy of the electrons. This can be seen in bulk samples as the de Haas - van Alphen effect where the magnetic field affects the free energy and leads to oscillations of the carrier density and consequently the total magnetisation of the sample which can then be detected. This is a powerful tool in exploring the Fermi surface of metals.

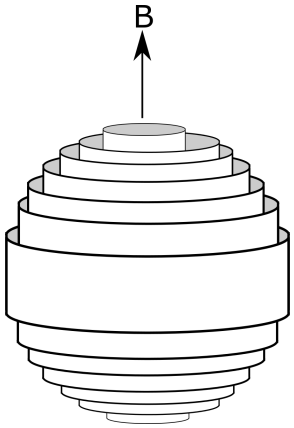

Figure 5.2.: Applying a magnetic field quantises the allowed energy values, discretising the DOS. For a 3D material witha spherical Fermi surface concentric tubes of Landau leves form.

If the material is thin it restricts the choice of current and field direction needed in order to measure the voltage, but a real change occurs when the sample is thin enough to confine the electron wavefunction, making the material effectively two dimensional. In that situation the magnetic field can no longer be treated classically. Instead it only allows energy states conforming to discrete values.

In this case the Hall voltage is no longer linear in magnetic field and the longitudinal voltage no longer constant, which manifests when the two-dimensional sample is at low temperature and has sufficiently low carrier density. Fig. 5.3 shows the anti-synchronous oscillations that appear in the transverse and longitudinal directions of the voltage, which are characteristic of the integer [1] quantum Hall effect. The quantum Hall state is achieved with the simultaneous vanishing of longitudinal resistance and entry onto a so-called a plateau in the transverse resistance (see fig.5.3). This unusual magnetotransport is a property of two-dimensional materials.

[1] There is also the fractional quantum Hall effect, in which the transverse resistance plateaus are governed by fractions of the electron charge. The fractions are attributed to "composite fermions" - bound states of electrons to vortices. It only manifests in very clean samples of high mobility and is its own separate field of study.

5.1. Integer quantum Hall effect

The non-linear Hall voltage and oscilllating longitudinal voltage seen are due to the discrete density of states imposed by the magnetic field, and the effect of high magnetic field on transport. At high fields the motion of electrons is confined to travel along the edges of the sample.

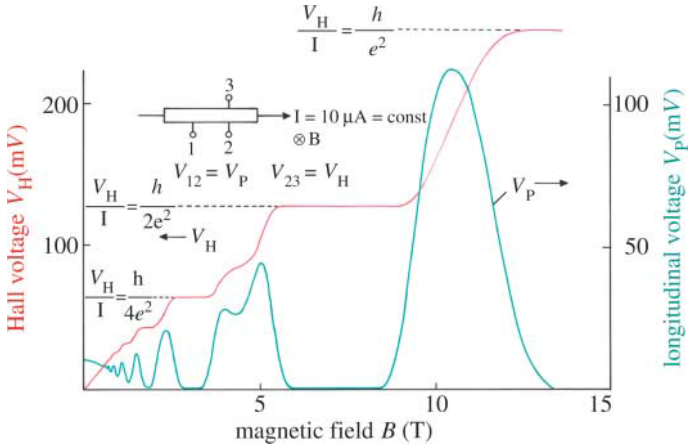

Figure 5.3.: The longitudinal and transverse voltage in a GaAs Hall bar demonstrating the vanishing V_{xx} and plateaus in V_{xy} (image from [75] These features arise from Landau quantisation together with two-dimensional confinement. The effect was discovered in 1980 in MOSFETs

The average DOS must be the same in finite magnetic field as it is in zero field, but becomes divided across the Landau levels (LL) (fig.5.4).

In the ideal case the LL are delta functions, but in fact they have finite width due to impurity scattering as this affects the lifetime of the state, $\Gamma = \hbar/\tau_i$. The carrier density drops to zero in the space between LL in an idealised situation of Gaussian broadening, so it is sometimes called the 'mobility gap'. Once the magnetic field is large enough that the separation of Landau levels becomes greater than the width of the LL due to broadening, the states become completely discrete.

In some situations it is evident that in fact there is a background density of states bettween the LL, but as long as the separation between the LL centres is greater than the energy of the electrons, the oscillations and quantum Hall state remain intact.

The broadening is usually represented using a Gaussian curve and gives the wide plateaus experimentally observed. Without impurity scattering there would be very narrow regions to observe the quantum Hall state.

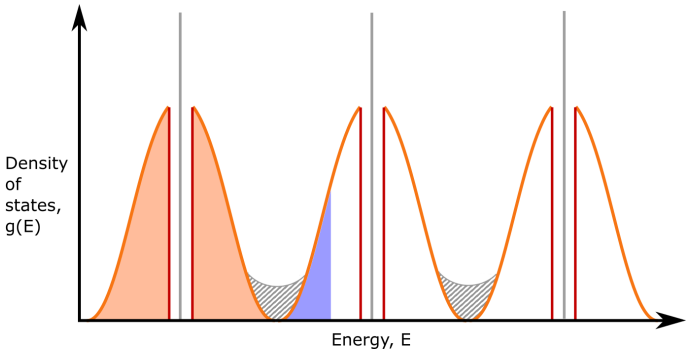

Figure 5.4.: Ideal LL are δ functions (grey vertical lines), and are equidistantly spaced in 2DEGs. Scattering broadens these in real devices. The centre extended (conduction) states are then surrounded by localised states in the tails. The QH state is realised when E_F is in the mobility gap between LL - fixed R_{xy}, vanishing R_{xx} as there are no available states for conduction (orange fill). Both are finite when the next LL is partially filled (blue fill). It is possible to have a constant background DOS (grey fill).

This region would be determined by the number of available states. The average DOS in finite field must be the same as the DOS in zero field, even if it is split across discrete LL. This gives the average DOS in finite field as $2N_L/\hbar\omega_c$, where $\omega_c = eB/m^*$, N_L is the number of states and the factor of two accounts for the spin. The energy difference between adjacent LL helps to quantify this, as the number of possible states must correspond to the number of free electron wavevector states and so the energy is $E = \frac{\hbar^2 k_L^2}{2m^*}$. Then the DOS, $g(E) = 2g(k)\frac{dk}{dE} = \frac{m_e}{\pi\hbar^2}$. Rearranging gives

$$N_L = \frac{eB}{h} \tag{5.1}$$

These states constitute integer filling at the centre of each LL and are also responsible for conduction in the QH state as they form one dimensional channels. Their formation is demonstrated in fig.(5.5a) by considering the cross section of the device channel. The physical edge of the channel forces a confining potential on the LL forcing them to bend up and cross the Fermi level.

Due to the potential difference between the source and drain contacts there are two lines of equipotential, so each LL has two 1D channels. Viewed from above the conduction channel travels around the edge of the sample (fig.5.5b). Considering the centre of the channel as zero momentum, it can be seen that the equipotential lines move in opposite directions since they have opposite momenta. This, together with the 1-D nature of the channels and their spatial separation essentially suppresses backscattering in the QH state.

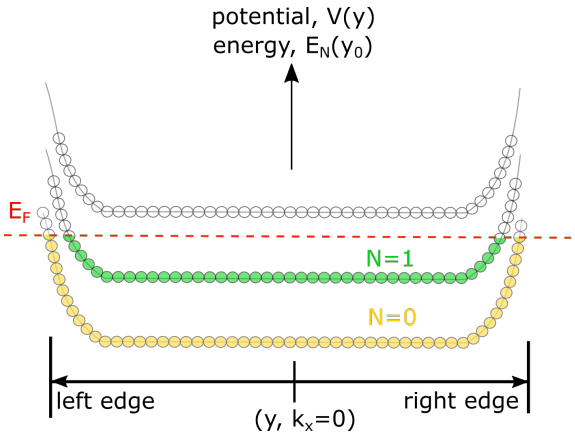

(a) A cross section of the channel width (y-axis) to show the filling of Landau levels. There is a real space confinement potential, V(y) due to the physical edges of the channel. The states look the same in momentum space, E_N vs k_x, and show that momentum of the states is of opposite sign on the two sides of the channel.

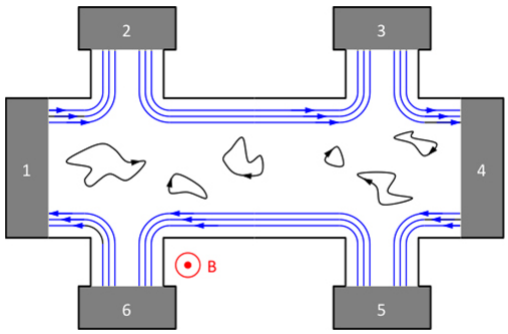

(b) Diagram of the edge channels as seen from above the plane of the channel, demonstrating three filled LL and the localised states in the bulk. This can be investigated using scanning probe microscopy [75].

Figure 5.5.: Quantisation of electrons in a 2DES in a magnetic field.

The electrons which surround the LL centre are known as localised states. They form enclosed orbits in the potential energy minima of the spatial fluctations in LL energy, which are created by the impurity scattering. This prevents them taking part in conduction.

The extended and localised states alternate around the edge of the sample, enclosing a non-conducting bulk. This can be observed on the surface of the sample, and are demonstrated to correspond to metallic, compressible and insulating, incompressible regions respectively.

In the QH state the absence of conduction and necessarily perfect contacts means that the transport can be described using the Landauer-Büttiker formalism which is based on transmission and reflectance rates from the contacts.

The edge state model struggles to address finite currents and transport in the bulk, but it holds for ideal QH states irrespective of the material. In semiconductor 2DEGs the QH plateaus occur at integer values of the filling factor while there is a shift of 1/2 and a multiple of 4 for graphene,which means that the QHE in graphene is sometimes referred to as the anomalous quantum Hall effect. The multiple of 4 accounts for the valley and spin

degeneracies, while the shift is due to the Berry phase, but the basic physics is unchanged. However, when the energy dependence of magnetic field is addressed, instead of the usual equidistant energy levels of a harmonic oscillator a $\sqrt{B}$ dependence is found.

Consequently the energy spacing between the first two LL is much larger in graphene than say GaAs. It makes it easier to realise the QHE because energy separation is maintained at higher carrier concentrations and much higher temperatures.

5.2. Dissipation - quantum Hall breakdown

When the quantum Hall state has been achieved it is very robust against temperature and current. There will be no deviation from the plateau value until significant current is applied and the longitudinal resistance deviates from zero. The state will hold at exactly integer filling, although the electron system is affected: the plateau width can narrow, the SdH amplitude increase. However, for a given temperature, it does breakdown eventually when excess bias current is applied. The value of critical breakdown current is found to increase sharply on the plateau as the centre of plateau is approached, where there is exact integer filling of the LL and the maximum breakdown current is found. There have been several mechanisms proposed to explain the abrupt increase in longitudinal resistance at breakdown, including Zener tunnelling and Cherenkov acoustic phonons. However they do not have good agreement with experimental values. One of the considerations in deducing the mechanism that triggers the destruction of the quantum Hall state is to decide whether heating is a cause or just an effect, and what role the Hall field plays. The bootstrap heating mechanism provides a subtle resolution and has good agreement with experimental values [76].

5.2.1. Bootstrap heating mechanism

The bootstrap electron heating (BSEH) mechanism holds for samples where the breakdown current increases linearly with the width of the sample and argues that no “trigger” from the Hall field is required to bring on breakdown. Instead, the features of breakdown are accounted for by the interplay of the energy gain rate, G and loss rate, L, of the carriers. This results in there being a critical value of electric field at which the small fluctuations in energy distribution, inherent at any finite temperature, can be amplified such that an avalanche process builds along the length of the sample.

Instability can set in when G exceeds L. Both rates are assumed to increase smoothly with temperature, but L is independent of the Hall field while, for finite conductivity G is not: G= j · E = $\sigma_{xx}(E_x^2 + E_y^2)$. In a strong magnetic field $E_x \ll E_y$, so that G= $\sigma_{xx}E_y^2$. This makes the stability condition:

$$\partial G/\partial T_e < \partial L/\partial T_e \tag{5.2}$$

with the critical point occuring when the curve of G is tangent to the curve of L [77].

The fluctuation in carrier homogeneity is likely, but due to the very reduced screening present in the quantum Hall state, a small change in the density of states can result in a large fluctuation in LL energy. When equation (5.2) is not met the electron cannot successfully lose all its energy to the Fermi sea and so contributes to heating in the electron system. This causes a runaway situation to occur until the stability condition is met once more, which can sometimes be observed as saturation of conductivity. In order to better understand how stability can be re-established, it is necessary to explore what happens to the excited electron.

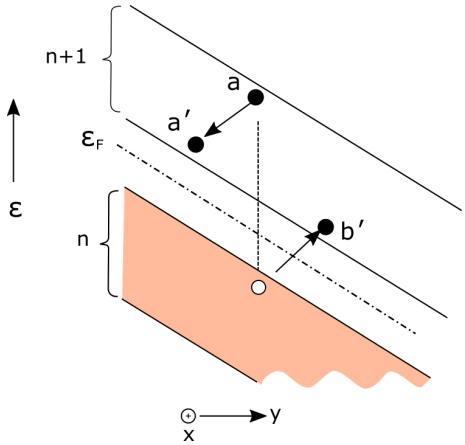

Figure 5.6.: Channel profile as per fig.5.5a to show LL tilted by potential of Hall field. Hot electrons undergo impact ionisation at the mobility gap, which creates an electron-hole pair. The energy gain under the transverse potential, increase in carrier multiplication and repeated impact ionisation forms an avalanche along the drift direction, x Image after[76]

The LL are subject to the Hall field across the width of the sample, as is the local Fermi energy (5.6). The excited electron cannot cross into the next LL because of the mobility gap. However, through a process of impact ionisation - collision with a cold electron

and exciting that into the higher LL, it can create an electron-hole pair [76]. This also contributes to heating, because the potential slope of the Hall field means that the initially excited electron, the hole and the newly excited electron can all gain kinetic energy as they drift in the direct of the current (x). As the energy gain is along the current direction an avalanche develops. Once significant numbers of electron-hole pairs are present, the recombination lifetime is reduced which makes it an effective process for losing energy and raising temperature [76].

The consequence of the avalanche is a spatial dependence of breakdown along x; an exponential increase, then saturation, in resistivity as the distance between measurement contacts increases [76]. It is one of the characteristics of BSEH, but also one which is less frequently fulfilled. Stronger evidence to support BSEH, which other models are not able to meet, lies in its ability to explain the maximum in breakdown current at integer filling provided a constant background of density of states is included (fig.5.4) [76].

5.2.2. Hot spots

One of the phenomena associated with the breakdown of the quantum Hall state is the appearance of so-called 'hot spots' at the source and drain contacts, at diagonally opposite corners of the channel (fig.5.7). The position of the hot spots is determined by the current and magnetic field directions, as per the the edge state model. They were first observed by Klass et al. using a superfluid fountain [78] in 1991 and it was later found that these spots radiate cyclotron emission (CE) [79]. However, the edge state model does not account for their appearance, nor does the bootstrap heating mechanism predict them.

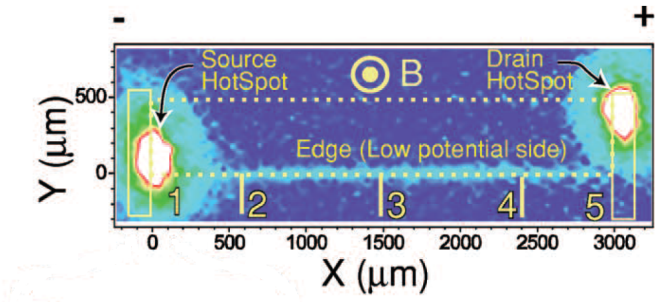

Figure 5.7.: The image reported by Komiyama et al. [80] showing the areas of strong cyclotron emission with the position of the device channel and source and drain contacts marked in white.

Approaching the problem is challenging because the original Büttiker model [81] holds for infinitesimal current but not for finite current, let alone the non-equilibrium electrons

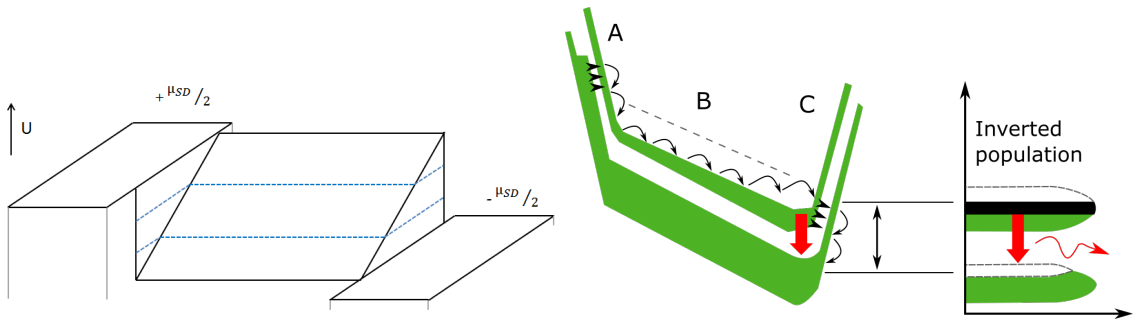

(a) The potential of the device showing the source and drain contacts and the slope in the channel due to finite current.

(b) CE attributed to tunnelling energies at source and de-excitation from higher LL at the drain contact, arising from the tilted LL.Image after [83].

Figure 5.8.: The mechanisms behind hot spots in Hall bars

which must be present when emission is seen. However, as the current is increased the Hall field is strengthened, which subjects the channel to a potential slope across its width (fig.5.8a). This forms the basis of theoretical work by van Son et al. [82] which was able to predict the hotspot near the source as being due to the injection of nonequilibrium electrons but did not predict the one on the drain side. Kawano et al. built on this using a photoconductive detector [83] and were able to explain both, summarised below and in figure 5.8b.

The slope in potential means that electrons have to tunnel into the device at the source contact. Some states are left unoccupied because the probability of tunnelling cannot be unity. This leaves the highest LL not entirely filled. Additionally, some electrons with higher energy will tunnel into the higher LL, so these two factors could explain the emission at the source contact. Once in the channel, if an electron travels the interior due to its own energy and the potential gradient it may arrive at the drain contact in the higher LL (fig.5.8b). Then it has to de-excite in order to pass into the drain contact. In this model it is also possible for emission to occur along the low potential edge. Using a second Hall bar as a detector to achieve greater sensitivity, Ikushima et al. did observe this (fig.5.7) in later work [84, 80] which provides strong support for this explanation.

In addition to the problem of the origin of the hotspots, there has been difficulty quantifying their temperature and whether they occur inside the contacts or not. Part of the difficulty arose due to observing the hotspots when the longitudinal resistance was not vanishing. Two terminal measurements [83] showed that the filling of the LL determines their nature and physical location. At exactly integer filling the hotspots are in the

2DEG, however away from exact filling even greater CE is observed, which does occur in the contacts.

Hot spots have not yet been observed in graphene. In exfoliated material this could be due to the small sample sizes limiting channel length. However investigating this of particular interest in epitaxial graphene with the high breakdown currents [85] and the fast thermal relaxation [86] observed.

5.3. Graphene magneto-optics

Graphene couples strongly to light due to its linear dispersion, with a single sheet absorbing 2.3% of incident light, which is in good agreement with theory [87]. Apart from the easy implementation, with insensitivty to local defects and compatibility with Si-CMOS technology, graphene's greatest advantage is its tunability over a wide wavelength range thanks to the use of electric field effect gating [87]. In particular, it could make for a suitable detector even in the FIR-THz regime which is traditionally difficult to access.

The technical challenge lies in increasing the absorption to provide sufficient signal. Gold nanoparticles, silicon waveguides, and incorporation into microcavities have all been explored, with a focus on creating internal fields via work function differences rather than external biasing which can create large dark currents [87]. This is all already true at room temperature and zero magnetic field.

Some of the best detectors for the FIR-THz regime are in fact quantum Hall crosses [88], precisely because the spacing of the LL corresponds to these energies. The robustness of the QH effect in graphene allows it to manifest liquid nitrogen temperatures, where it has been demonstrated to have a photoresponse to 10.6μm irradiation [89]. This photoresponse was not the resonant response hoped for when using Hall crosses, but is promising nonetheless.

5.3.1. Optical transitions

In a perpendicular magnetic field the linear dispersion of graphene results in $\sqrt{B}$ energy dependence [90]. Subsequently the LL are not equidistant as they are in 2DEGs with parabolic dispersion. The selection rule for the inter-LL transitions, $|n| = |n| + 1$, is unusual because it depends on the absolute value of the LL number which together with

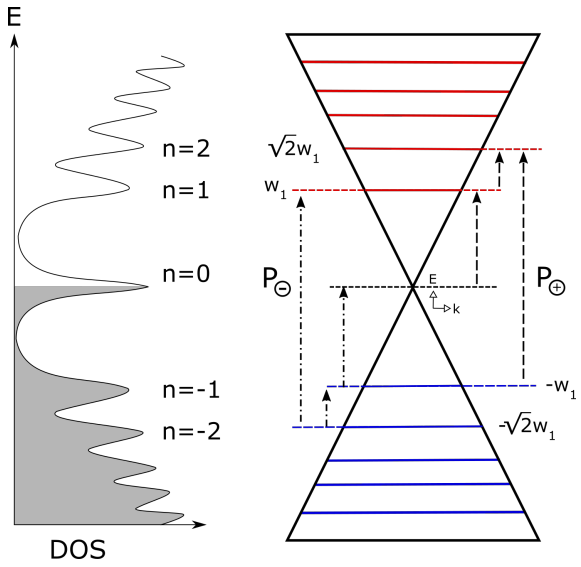

Figure 5.9.: LL of monolayer graphene: $E_n = sign(n)v_F\sqrt{2|e|\hbar B|n|}$. The selection rule allows for intra- and inter-band transitions. The chiral nature of the Dirac Fermions however, adds an extra level of complexity: the right polarisation is necessary excitation.

the symmetry of the electron and hole bands means it simultaneously governs intra- and inter- band transitions. Furthermore the charge carriers are chiral. This means that the polarisation of the light is significant, and it distinguishes transitions that otherwise have the same energy (fig.5.9).

LL spectroscopy allows the probing of the energy levels by irradiation. It is a generic term to describe transitions between LL. When the wavelength of the light matches the energy separation of the levels some quasiparticles can be excited into the higher LL if there are states available. Since this is determined by the cyclotron frequency for the material, such measurements are also interchangeably referred to as cyclotron resonance (CR), although strictly CR refers to intraband transitions [90].

5.3.2. Cyclotron resonance

CR experiments are often performed as transmission experiments and reveal information about the 2DES through the dynamical conductivity. In this way it expected that both localised and non-localised (integer-filling, extended states) are probed.

CR can also be measured as photoresponse in transport measurements, usually by applying a lock-in technique to obtain a change in voltage (or resistance). This however is expected

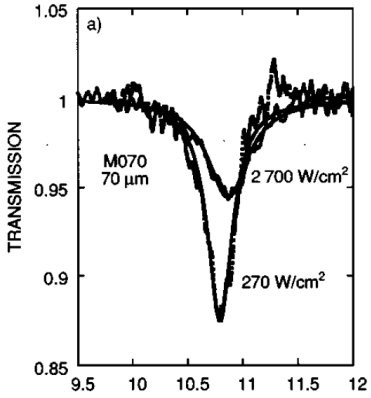

Figure 5.10.: CR of GaAs measured in transmission. Image from ref. [91].

to exclude the localised states, provided that there is no thermal contact between the two sets of states. The two types of measurement agree and when compared the slightly wider peak of the transmission measurement suggests that localised states may have a shorter scattering time [92].

However, there are also features observed which do not correspond to CR, particularly in transport measurements. The most common one is a bolometric response observed on either side of a quantum Hall plateau. It can be identified by its dependence on bias current and its fixed position regardless of laser energy.

This bolometric response is found to depend on the filling factor, which provides an explanation of its presence at the edge of the plateau in terms of the interplay between the critical current and substrate heating [88]. There is also evidence that there is contribution from a photoinduced Hall current, which is not invariant under magnetic field direction, contrary to the usually considered longitudinal component.This type of bolometric response has been observed in graphene too [89].

Deacon et al. [93] measured photoconduction in exfoliated graphene and by varying the magnetic field and carrier density obtained a CR map (fig.5.11). The resonances obtained showed a very broad curve in magnetic field (9-13T) for the transition from the 0th to the 1st LL, with much smaller response for 1st to 2nd LL. This was found to be the case over a range of wavelengths and also for -1 to 0th transition (fig.5.11). In addition to the CR response, a negative response was seen at low magnetic fields and low carrier densities [93]. More significantly there is response between the LL which is due to localised states in partially filled LL being excited into the extended state, either thermally or by variable

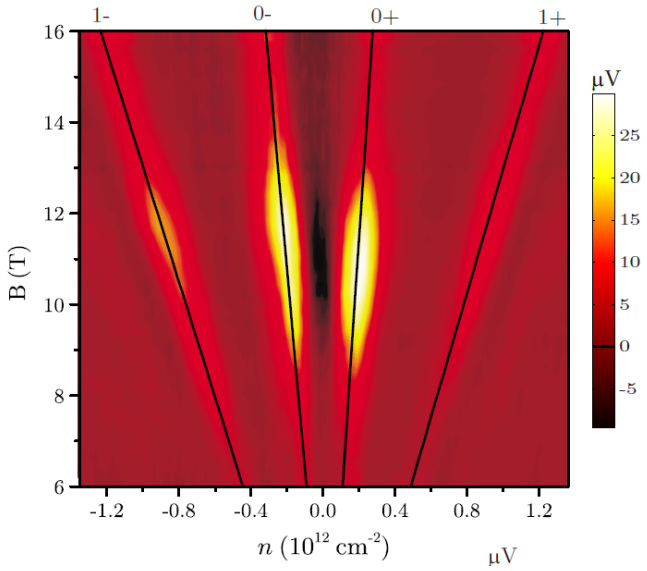

Figure 5.11.: Map of photoconductance in carrier density and magnetic field, showing location and intensity of CR resonance in exfoliated graphene. Image from ref. [93].

range hopping.

In exfoliated graphene it is possible to use a gate to vary the carrier density, which allows for a full demonstration of the different responses. This is not possible in EpiG, and it is found that although the carrier density is nominally fixed by charge transfer from the substrate, the charge transfer actually increases with magnetic field [50]. As a result once on the $\nu = 2$ plateau the filling stays close to integer filling throughout [95].

Some of the difficulty in attempting to observe hotspots in graphene may be due to the presence of heating effects and the broad resonance, similar to the case with contacts creating greater CE hotspots than the integer filling response [83].

5.4. Noise measurement of the quantum Hall state

Noise measurement is able to provide information that is inaccessible to other techniques which take time-averaged values. Generally speaking noise in a dissipationless quantum conductor is considered to be the voltage fluctations caused by the emission and absorption of electrons by the contacts which act as electron reservoirs [96].

The mean square of the voltage fluctuation, $\overline{u^2}$ within a bandwidth Δf gives the mean-

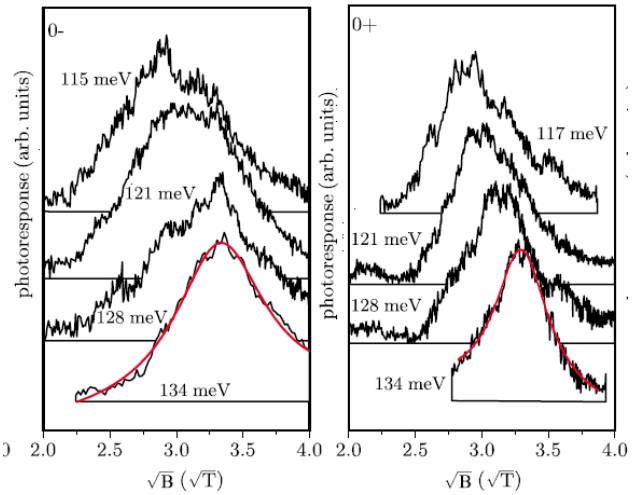

Figure 5.12.: Fixed carrier density showing CR width dependence on laser wavelength. The resonance is very broad. Image from [94].

square noise voltage density, S_u. However, in the low frequency approximation S_u is frequency independent and can be given by:

$$S_u \equiv \overline{u^2}/\Delta f = 4k_B T R + 2eIR^2F \tag{5.3}$$

k_B - Boltzmann constant, T - temperature of contacts, e- electron charge, F - Fano factor, I - current, R - resistance

The first term is Johnson-Nyquist noise that is the result of thermally agitated current fluctuations. It holds for both classical and quantum scales, making for a very reliable thermometry technique. In this way the electron temperature may be known when it is otherwise inaccessible.

Shot noise, the second term, is caused by voltage fluctuation due to the discreteness of electron charge. It is often considered in terms of flow across a potential barrier. The Fano factor relates the success of transmission, with a perfect conductor having F=0.

It is theoretically expected and experimentally observed that the noise of the quantum Hall regime agrees with the Johnson-Nyquist noise of a conventional resistor, if the latter were of the same resistance value and at the same temperature [96]. While it is in fact a macroscopic resistor, the QH state is also a nonballistic and reflection-free quantum conductor. This means that no shot noise is expected, since it would only occurr if there were point scatterers or poor contacts [96].

The absence of shot noise was demonstrated by Schurr et al. [96], but it is important to note that it cannot be ignored out of hand as a contributor to the noise because it can be applicable when $eV_H \gg kT$.

There is also total agreement between resistance and noise measurement in [97] as predicted by the transmission approach [98]. Measuring the noise in a Hall Barr at one contact reveals the correlation to R_{xy}, but using two also shows the correlation to R_{xx}. All of which points to noise measurement being a promising tool for measuring the breakdown of the QH state.

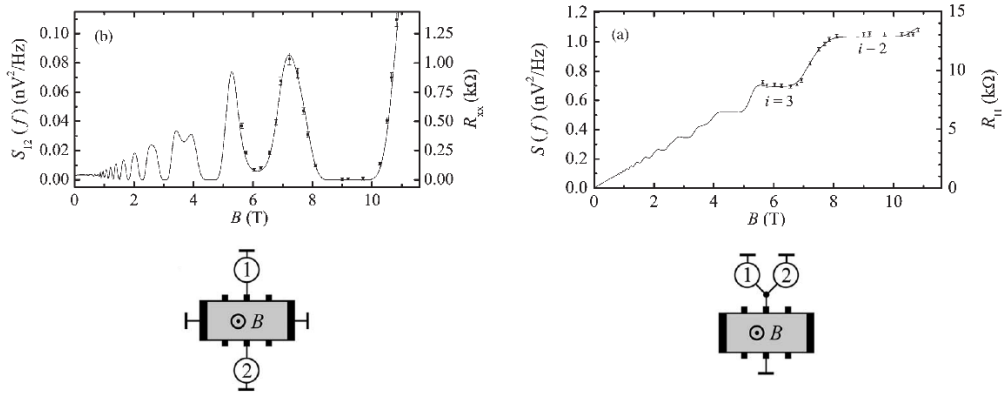

Figure 5.13.: Individual noise spectral density measurements taken at different fields overlayed on transport data. The probe configuration allow R_{xx} or R_{xy} to be extracted.Taken and adapted from Schurr et al. [97]

The situation is altered when current is applied. Burst noise is observed at increased currents, but also non-integer filling factor, which results in a frequency dependent contribution at low frequencies [97]. There is also a quadratic rise in total noise power with increased current, starting from before breakdown being recorded. These observation seem to support the clear evidence by Chida et al. [99] of a 'precursor regime' prior to breakdown. A precursor regime is particularly interesting in view of the interpration of excess noise being the result of partially reflected edge states [98].

Although **not** in the quantum Hall regime, it is worth noting an unusual property of graphene with respect to noise. Measurements performed on ballistic graphene devices with two contacts, without any magnetic field applied, have found shot noise to be present [100]. The Fano factor found, roughly F=1/3, agrees with theory, but is surprising because

this is the value universally found in diffusive metals. This is attributed to quantum relativistic effects [101], namely 'Zitterbewegung' which is a jitter motion due interference of states with positive and negative energy [102].

Part III.

Experimental results

6. Experimental set up, samples and measurement techniques

6.1. Graphene devices

The devices used in all measurements of graphene had a standard Hall bar configuration. The epitaxial graphene was grown on Si-terminated face of silicon carbide by subliming away the silicon at 2000°C in 1 atm argon.

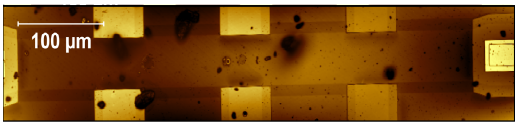

(a) Photoconductivity measurement device.

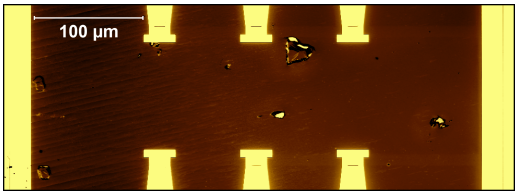

(b) Noise measurement device

Figure 6.1.: Images of Hall bars measured

The devices in the three experiments were fabricated at different times onto 7mm × 7mm chips, using the same technique. Metallic contacts are prone to lift-off when deposited directly onto graphene, so oxygen plasma etching is used to remove the graphene in order to evaporate Ti/Au anchors directly onto the silicon carbide. After this, ohmic contacts are deposited on top of both the anchors and the graphene. Finally, the Hall bar is patterned with e-beam lithography and the graphene is removed from those areas with oxygen plasma etching.

Measurement	Device dimensions	Carrier density control
Weak localisation	50µm × 20µm	Photochemical gating
Photoconductivity	148µm × 49µm	Corona discharge
QH Noise (GaAs)	125µm × 80µm	N/A
QH Noise	177µm × 98µm	Corona discharge

After fabrication the sample is encapsulated in a thick polymer layer (PMMA) to prevent unintentional doping. In order to reduce the intrinsic n-doping to sufficiently low levels that allow the observation of the $\nu = 2$ plateau within 11T, the two techniques that were used will be described in the following section.

6.1.1. Carrier density control

The high carrier density increases the necessity for carrier density control. It is unfortunately not possible to use electrostatic gating to efficiently control the carrier density in epitaxial graphene [103] due to the pinning of the Fermi level. This means the range of achievable carrier densities through electrostatic gating is not large enough, particularly for quantum Hall work.

Although GFET configurations have been investigated, the dielectric leakage, which is of the order of nA/μm^2 for a few volts [104], makes it unsuitable for metrological purposes.

Intercalation by gases to separate the graphene from the substrate is successful, particularly with hydrogen, and has been extensively studied [105, 106]. This process does not just separate but converts the interfacial layer into a graphene layer. However, the interfacial layer and subsequent pinning of the Fermi level also results in a very robust quantum Hall effect, with a long $\nu = 2$ plateau. This is a useful property to preserve, so techniques have been developed to provide a large range of carrier densities, in a reversible fashion, which are also stable and do not degrade the sample or introduce noise to the device.

Photochemical gating

The n-doping in graphene means that the goal is to reduce the number of electrons. For metrological purposes it is necessary to have a technique that will have great stability. The exposed nature of a graphene sheet means that anything coming into contact with the surface can result in doping. For this reason samples often have a thin layer of electrically neutral copolymer resist deposited on them such as PMMA. This practic e offers a springboard to a technique which takes advantage of the easily doped nature of graphene and meets the necessary criteria.

There exists a polymer resist called ZEP520A which compared to PMMA replaces a methyl group in the hydrocarbon chain with a chlorine atom. Irradiating ZEP520A with deep

UV radiation of wavelength 250nm results in photodissociation, with the now chlorine radical moving away from the molecule [107]. The chlorine radical powerfully attracts electrons, drawing them away from the graphene sheet and trapping them in the polymer layer.

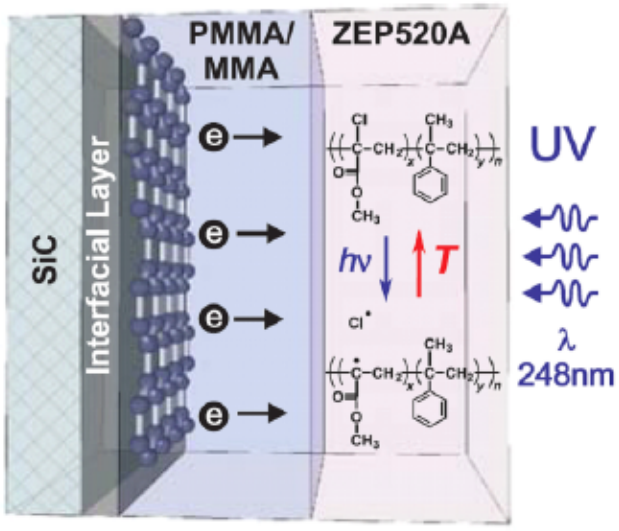

Figure 6.2.: Diagram of components for photochemical gating. Molecular diagrams illustrate radical and acceptor sites formed by the scission of the active moelcule in ZEP520A, due to photodissociation by the deep UV. Image from [108].

The photochemical gating makes use of this property. ZEP520A is deposited on the sample on top of a spacer layer of neutral PMMA. The PMMA acts both as a dielectric and preserves the mobility of electrons in graphene, which provides an improvement on chemical gating, because photo-generated dopants are spatially decoupled from the graphene [103]. The now twice coated sample is exposed to deep UV to activate the reaction in the ZEP520A layer so as to attract electrons out of the graphene, and to diffuse through the spacer layer to the acceptor sites ine ZEP520A.

The ZEP520A cannot be activated when at low temperature, so the exposure to UV needs to be performed at room temperature. Some further reduction in carrier density is then seen when the sample is cooled.

Sources of deep UV are not commonplace, but in addition to light boxes used in lithography and mercury lamps it is now possible to purchase LEDs operating in this region.

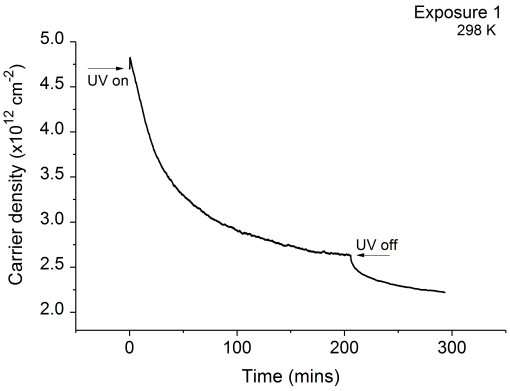

(a) First exposure of sample prepared for photochemical gating to deep UV LED. Rapid, dominant decrease in electron concentration is only seen on first exposure.

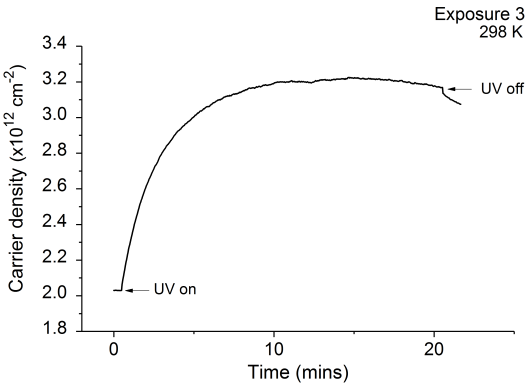

(b) Third exposure of photochemically gated device showing behaviour during irradiation. Despite this new dynamic, net reduction in electron concentration is maintained, and can bee seen once the sample has relaxed.

Figure 6.3.: There is a a discrete change in transverse voltage when the UV is switched on and off. The size of this increases a little with dose, but could not be linked to any excitation process of the substrate or the graphene.

The dynamics and effect of UV dose have been investigated [109] using both an LED and a small mercury pencil lamp used for spectrometer calibration. The power of both was determined using a silicon carbide detector, with the mercury lamp found to be much more powerful, to the extent that the ozone created by performing exposure in ambient conditions was no longer negligible. The investigation consisted of performing room temperature magnetotransport measurements with the sample inside an enclosure, together with either the LED or mercury lamp spaced a few millimetres from the source.

The findings gave an insight into both the efficacy and the limitations of the photochemical gating technique. It was found that even with repeated exposure it was difficult to reach the Dirac point. This is in part because although neutrality is neared with extensive exposure, the exposure can bake the resist which can then result in instability. It was also seen that about half of the total reduction possible is obtained in the first exposure (fig.6.3a), inadvertently setting a limit on the total achievable reduction in electron concentration.

After the first exposure, instead of an immediate reduction in carrier density, an increase in electron concentration is seen (fig.6.3b). It is only once the UV is switched off that the reduction begins, and the time constant is hours long before a near final value is

reached. Despite the increase under UV the total reduction is never reversed, but the electron extraction effect diminished, irrespective of whether short or long exposures are used. So although high powers of UV can produce consistent results, fine tuning the carrier concentration remains difficult even using lower power sources.

This was the technique used on the sample used in the investigation of weak localisation.

Corona discharge

There are two areas in which photochemical gating could be improved upon for the quantum Hall application. The primary one is to extend the accessible carrier density closer to and beyond the Dirac point. Another is to improve the reversibility of the technique.

A disadvantage of the photochemical technique is that the first exposure largely determines the the maximum reduction in electron concentration, and the effect of exposure is not entirely predictable despite in situ monitoring. While it is possible to reverse the effect on the polymer layer by heating it beyond its glass temperature [108], or in case of excess exposure refurbishing the sample with new polymer coatings, these are separate, time consuming processes. It would be preferable to reverse doping alterations in situ. This may seem unfeasible, but it is possible for low temperature applications thanks to applying ions to the sample surface using corona discharge.

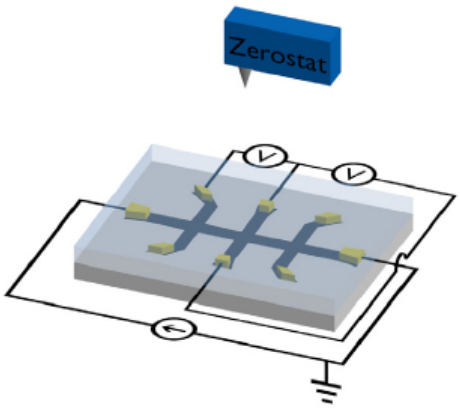

Figure 6.4.: The antistatic gun is held above the sample, and the piezo is activated by compression or expansion of the crystal to produce a voltage that ionises the species in the air. Due to the electric field lines around the tip one polarity is attracted to the tip while the other propagates away, allowing it to be deposited in the surface of the sample [103].

Corona discharge is the production of ions in a gas due to electrical discharge [103]. It can be created by applying a high voltage to a sharp tip or wire. The ions move along the lines of electric field [110, 111] and at sufficient proximity can be deposited on the sample surface.

In air the predominant species are H_2O^+ and CO_3^- [110, 111] for the respective voltage polarities.

The carrier density control is carried out in ambient conditions, using a piezo-activated antistatic gun to generate the corona discharge. The change in doping can be monitored in situ through the Hall voltage by connecting voltmeters to the device and a relatively small magnetic field (min. 500mT). The antistatic gun contains a piezo crystal which produces voltages of either polarity through either being compressed or expanded by the "trigger", thus allowing either positive or negative ions to be deposited on the sample surface in 1-2s long pulses. Applying negative voltage to the tip causes the negative ions produced to propagate away from the discharge source and become deposited on the surface. The ions can cover mm^2 areas, and the doping can be reversed immediately through depositing the opposite polarity of ion.

Repetition of pulses and decreased tip to surface distance allows carrier density of naturally n-doped epitaxial graphene sample to successfully pass the Dirac point to finish p-doped to high $\times 10^{12} cm^{-2}$ [103].

The graphene sample has a PMMA coating both to act as a dielectric and protect carrier mobility. It appears that the change in doping is independent of coating thickness [103].

In ambient conditions there is carrier density drift on the order of minutes, but the carrier concentration becomes fixed when the sample is cooled below 200K [103]. This makes the technique very effective for low temperature magnetotransport measurements as the carrier density can be maintained for many weeks at low temperature, particularly under stable conditions, but the doping is reversible once in ambient allowing any carrier concentration to be set in the future. By lowering the carrier density, the quantum Hall effect can be realised in magnetic fields of less than 5T at liquid helium temperatures.

This technique has been previously used in the semiconductor industry. The ions deposited on a dielectric layer induce a surface charge density on the underlying material. The strong effect on doping is possible through the low mobility of ions in the dielectric allowing large electric fields to form. The low dielectric ion mobility also suppresses dielectric breakdown,

which allows the electric fields to be even larger than those produced by metallic gates [112].

This was the technique used on the samples used in the investigation of quantum Hall breakdown and Landau level spectroscopy.

6.2. Weak localisation measurement

In order to be able to evaluate whether high frequency radiation causes additional scattering by direct interaction with charge carriers, known as dynamic dephasing, it is necessary to know the bolometric response of graphene. Although there are numerous ways in which to vary temperature in cryogenic conditions, the use of a cryogen-free dilution refrigerator is advantageous because it provides stable and well known bath temperatures as well as being economical. For this experiment an Oxford Instruments Triton 200 cryogen-free dilution refrigerator was used to carry out measurements.

Figure 6.5.: Oxford Instruments Triton 200 dry dilution refrigerator. Already installed coaxial lines, well controlled bath temperature from as low as 10mK, and a programmable 12T magnet made it well suited to weak localisation studies.

It was particularly suited to the work planned because of its low base temperature of 1mK

and the ease and stability with which different temperatures can be set. It also had a 12T magnet, which is greatly in excess of the magnetic field needed to suppress WL, however it has the advantage of being stable at low fields and being programmable. When looking to extract scattering times and in particular looking for small alterations to them, it is vital to take many data points, so having reproducible small field increments available was useful.

Ensuring the coupling of the microwaves to a sample requires undertaking device design, manufacture and implementation. However in this instance perfect coupling is not required because simple environmental exposure to high frequency radiation is a real scenario in a number of applications for which graphene may be used.

The Triton 200 is fitted with eight coaxial lines that go down into the sample holder puck. Exposing the coaxial core creates a simple dipole antenna. In order to irradiate the sample as well as possible, two pieces of copper coaxial cable were bent around to minimise the distance to the sample, which is is mounted onto a ceramic TO-8 header with gold contact pads for wire bonding.

A vector network analyser (VNA) was used to examine the signal, primarily to establish whether the level of attenuation was acceptable. Due to the reflections and the potential for standing waves the inside the puck, the exact frequencies used were determined based on the size of the signal seen on the lock-in. Microwaves were supplied using two different sources due to equipment availability, but no difference was observed and both had a range up to 20GHz. A dc block was placed on the output to ensure that noise and any resultant heating from the source were minimised.

The measurements were carried out using a photochemically gated Hall bar with channel dimensions 20μm by 100μm, with the voltage probes spaced 50μm apart. This qualifies the device as being large and so mesoscopic fluctuations are not expected to affect the WL. The first set of measurements applied a dc current and measured longitudinal and transverse voltage to obtain R_{xx} and R_{xy}, but it was quickly established that an ac current was preferable as it did not affect the WL peak observed but heated the sample less. Once an ac current was applied, the measurements were performed with a lock-in amplifier, which gave information on the phase instead of transverse voltage.

|0.2T| was observed to be sufficient to suppress the weak localisation, in part because as earlier work had indicated τ_{i} and τ_* were found to be constant.

6.3. Magneto-optic measurement

Cyclotron resonance measurements do not necessarily have to be performed at very low temperatures, which is particularly true for graphene and is also relevant to its application as a higher temperature resistance standard. A 4.2K LHe^4 cryostat with a 12T magnet was refurbished for this work.

The diagram in figure 6.6 shows large solenoid coils which are in fact roughly to scale. The dimensions of the magnet had drawbacks in terms of having large thermal mass and large inductance, but the large 50mm bore allowed room piezo positioners to comfortably fit in a probe. Figure 6.6 shows that a large XYZ stack could be implemented while keeping the sample centred in the magnet. There was even room for fine scanning piezos to be attached above and facilitate tuning fork based atomic force microscopy.

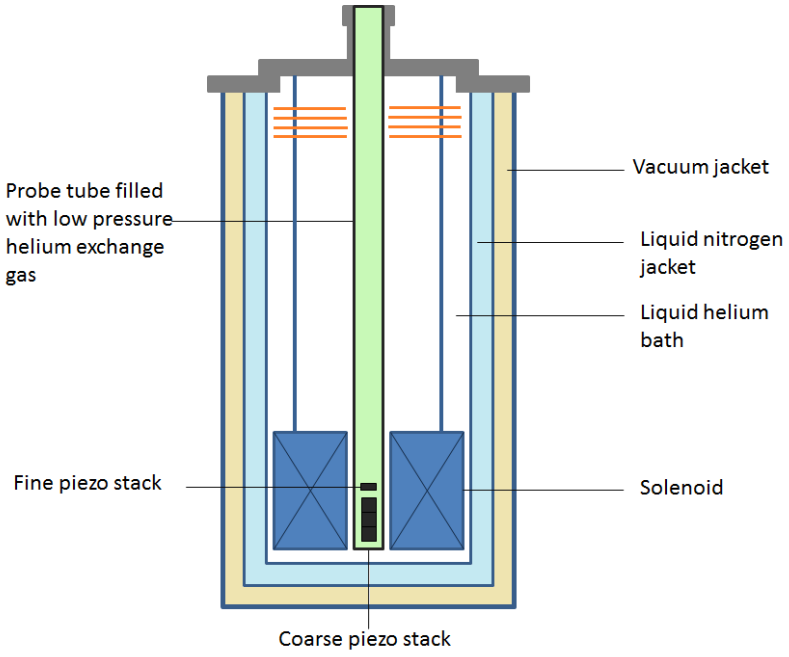

Figure 6.6.: The 4.2K cryostat has a 12T magnet 40cm in height and with 50mm bore. Orange lines indicate the position of radiation baffles, which also carried the quench protection

The refurbishment entailed making power lead extensions to connect to the top plate and installing quench protection. The orange lines near the top are radiation baffles designed to help reduce evaporation of the liquid bath. They were made of pcb board which allowed for easy installation of highly dissipative resistors to the copper surface in a protection circuit. Isolation of power leads was achieved by removing the copper in the vicinity of

the contact.

The probe was filled with exchange gas because the titanium Attocube piezo positioners took hours to cool in vacuum. The design of the probe is based on having two stainless steel tubes as the main support for the load at the bottom. This has a number of benefits: measurement cabling can be run separate to the high voltage lines necessary for the operation of piezos and it has the structure to allow for large unobstructed plates to be hung at the bottom (fig.6.7b). The plates are tightened with screws to a back plate. By milling parallel M3 tracks in the backplates the position of all components is adjustable. Adding holes to the stainless steel baffles with rotational offset to one another not only aided wiring (while preventing line of sight to room temperature), but made insertion of an optical fibre possible. In this way the probe was adapted for the study of cyclotron resonance in epitaxial graphene.

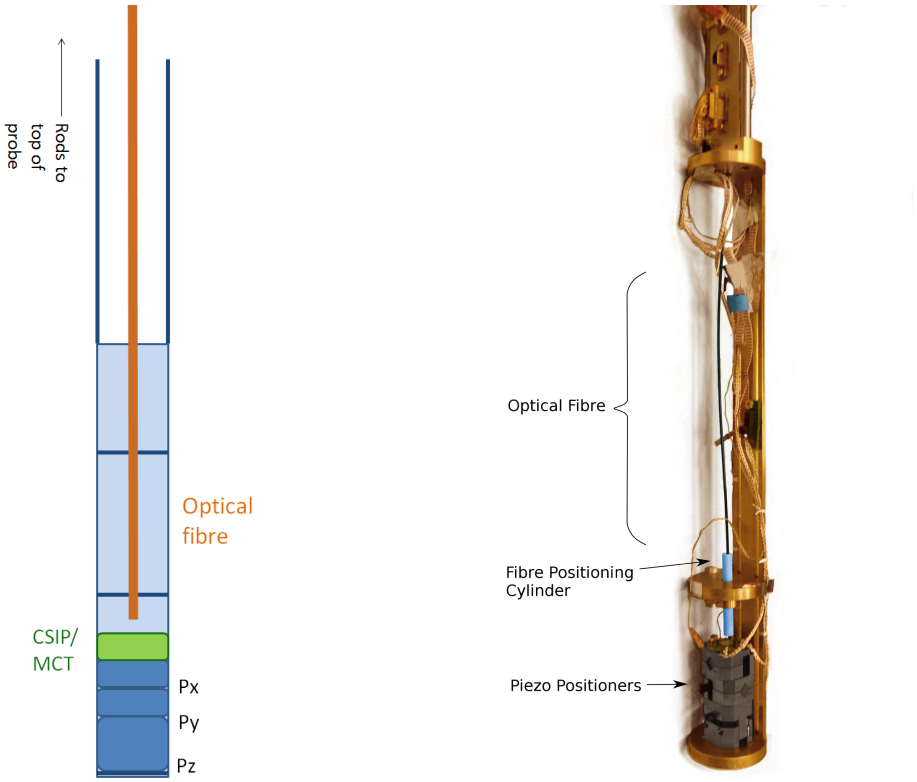

(a) Diagram of components for cyclotron resonance set-up of probe.

(b) Image of probe elements for photoresponse measurement.

Figure 6.7.: Photoresponse measurement set-up

The optical fibre comes down and is held in place above the sample using a brass plate. A

cylinder of Tufset plastic with an off-axis hole allows for better positioning above a specific device. This was employed to ensure a fixed position, but also because a typical graphene sample used is 7mm x 7mm and the fibre has 1mm diameter. Despite the samples being mounted on a flat pcb, the fixed position of the threaded holes in the top-plate of each piezo meant that the extra control over fibre position was necessary to reach some devices, in spite of the mobility range of the positioners.

Nonetheless, the use of positioners was crucial in achieving optical alignment, which is tricky enough to achieve on massive, fixed platforms at room temperature. It would also have been indispensible if CR had been observed and cyclotron emission from the hotspots had subsequently been sought out. As can be seen in fig.6.7b there was ample space to install a detector and optics for focusing it.

6.3.1. Coupling light

While the probe design made coupling light to the sample relatively easy in the sample space, there were other logistical steps to consider, such as what source to use and how make a vacuum-tight fitting for the optical fibre.

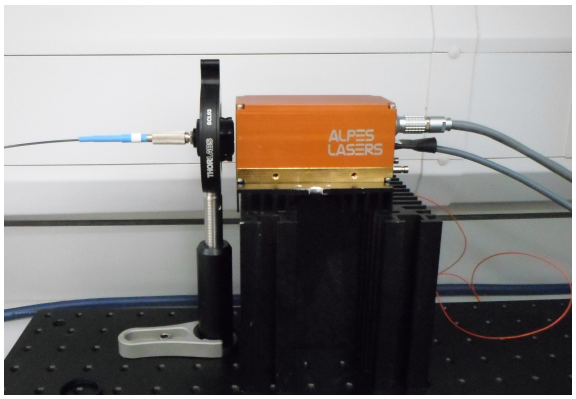

Figure 6.8.: Side view of the QCL from Alpes Lasers, together with the collation lens for coupling into the optical fibre. The laser diode generates a lot of heat so the large heat sink was quickly replaced with water cooling of the Peltier junction in the base.

A quantum cascade laser (QCL) is a superlattice structure which produces a sequence of quantum wells on a potential slope. This makes is possible to engineer any chosen wavelength on a small semiconductor diode, even traditionally inaccessible ones such as the 10µm needed for the $0 \rightarrow 1$ LL transition in graphene. Its small dimensions (the

housing is palm sized) are also advantageous for cryogenic applications where an elevated position will generally be necessary.

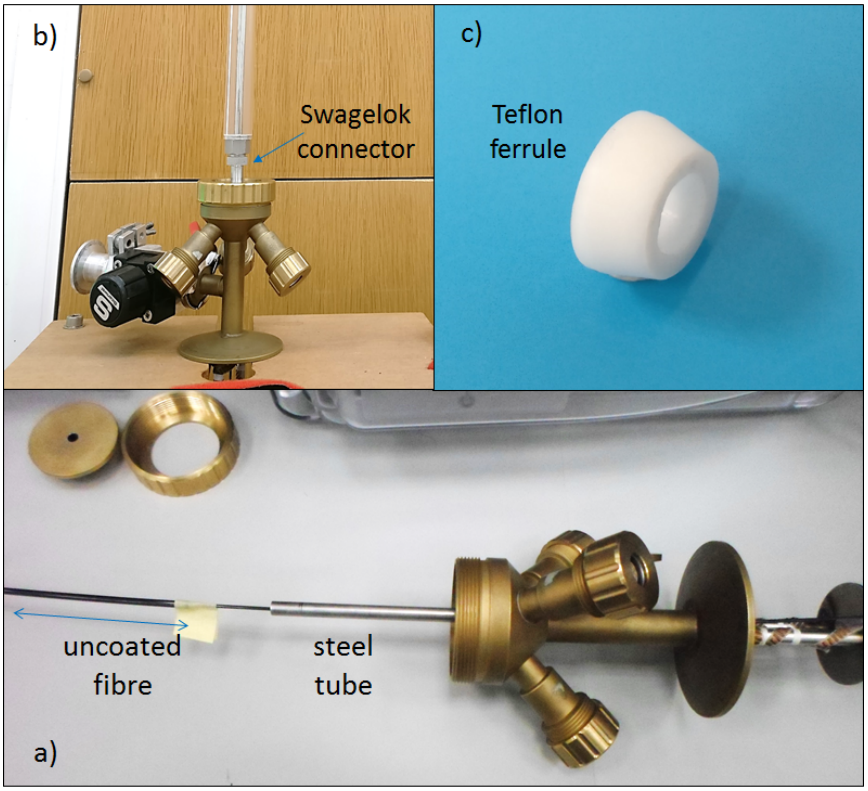

Figure 6.9.: A demonstration of the components required to a make a vacuum-tight optical fibre coupling. a) shows the components prior to assembly.

A small shelf and optical bread board were employed to meet this requirement. (Shelves as seen in figure 6.12b). The bread board was a necessary step because it was found that despite the point source emission of the diode through a mica window, very precise alignment of the optical fibre was necessary in order to produce sufficient output at the sample end. In fact the power output of the diode by itself is so low as to be barely perceptible, which is why a large collation lens has to be placed very close to the window. This gathers enough signal to be able to detect, but milliwatts of power can be coupled into the fibre when micrometer positioning stages are used.

The output was investigated using both a pyroelectric sensor and a powermeter at room temperature, and a mercury-cadmium-telluride bolometer (MCT) in liquid nitrogen.

In addition to its spatial distribution, the power output of the QCL was extensively char-

acterised. This was because as well as the dc bias applied to the QCL diode it can also accept an ac modulation which then modulates the power and makes it possible to use it in conjunction with a lock-in amplifier. This was particularly useful because the use of an optical chopper was not possible with the highly divergent output of the diode.

The challenge of coupling the fibre was met with a few crucial adaptations. The first thing to note is that this alteration was possible because the top of the probe head could be removed. It consists of a circular plate held on by a threaded ring top, noth of which can be seen in the top left of figure 6.9.

This allowed a plate with a hard soldered Swagelok connector to replace it (6.9b). Replacing the metal ferrule in the connector with one made of Teflon makes for a vacuum-tight seal [113]. The new ferrule needs to have sloped sides that match the original's, a through-hole just bigger than the diameter of the fibre and a small parallel sided head (6.9c). This is works because the remaining metal o-ring compresses the Teflon as the thread is tightened. The technique is usually used with smaller diameter fibres, but it worked well.

Inserting the fibre into a stainless steel tube ensures a good fit with the Swagelok connector, particularly if the tube polished smooth. The tube also helps to support the fibre, but more importantly it ensured vacuum-tightness with respect to the fibre coating too. For 10μm use the fibre has to be custom made using polycrystalline $AgCl_xBr_{1-x}$ and is particularly brittle, but the manufacturer (Art Photonics) agreed to leave a section of it unsheathed to ensure a good seal with the Stycast.

In addition, this is a totally reversible adaptation because the fibre can be removed, and replaced with the original plate.

6.4. Noise measurement

There are numerous methods for measuring noise and its auto- or cross-correlations. Dicarlo et al. combined cryogenic amplification with fast Fourier transform (FFT) based spectral measurement [114] and their technique is applied here.

In low frequency measurements an increase in temperature or resistance can often appear in the 1/f regime, which can make quantifying it difficult. However, if there is an inductance introduced together with a capacitance, an RLC tank circuit is formed and the noise is shifted into a resonance peak at higher frequency. This is the principle of operation here and the gain is provided by the transconductance of a high electron mobility transistor (HEMT).

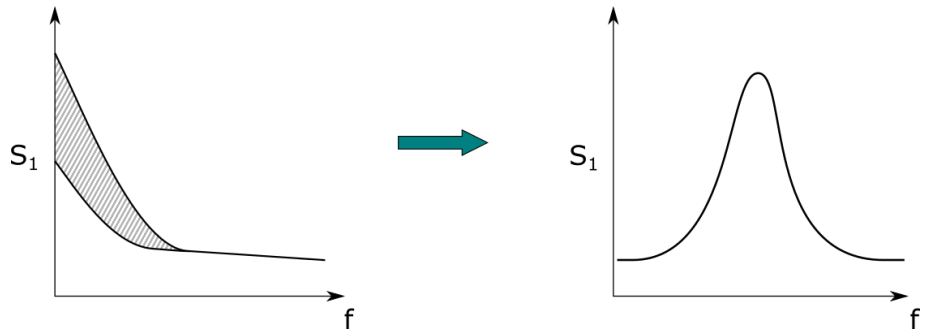

Figure 6.10.: The principle behind creating a tank circuit resonance is to move away from the 1/f regime and has the advantage of providing information about the system under test through its centre frequency and width.

For typical coaxial cables in a cryogenic probe the capacitance is of the order of 80pF, so that the centre frequency, f_0, is readily shifted to a few MHz with surface mount inductors. The centre frequency is determined by L and C only, and the width provides a measure of effective resistance:

$$f_0 = \frac{1}{2\pi\sqrt{LC}} \qquad \Delta f = \frac{1}{2\pi RC} \tag{6.1}$$

The two amplifiers will have slightly different frequency properties even if the components are carefully matched, and the individual HEMTs can have very different saturation points. Nonetheless extracting the correlation will subtract the flat, background white noise. The noise is then just the Johnson noise without any amplifier contribution, and can be obtained in real time. The Xr curve can be fitted, but the fit may not converge, while a simple evalution of the peak using bins is suitable for many evaluations. Simul-

taneously recording the spectrum of each measurement allows for future verification, or fitting if necessary.

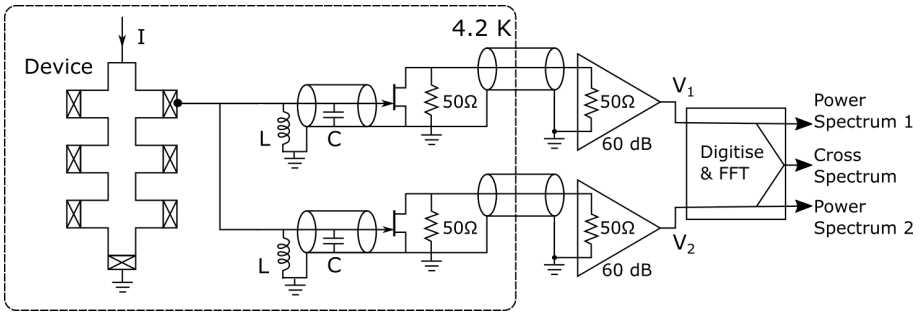

Figure 6.11.: A new probe with coaxial lines, dc loom and sample holder to accomodate both were constructed. The noise is measured at one contact with two amplifer channels. This allows for subtraction of the background white noise through extracting the correlaton. The Hall bar is biased when in magnetic field to investigate QH breakdown. L = 33μH, C=74pF so $f_0 = 3.22$MHz. Schematic adapted from [114].

In this investigation one contact is used and so the configuration resembles one used by Chida et al. [99]. The noise measurement works without any transport present, but since it is the QH breakdown that is of interest, bias current is applied and voltage measurements performed. The noise is much cleaner without the DVMs connected, so two sets of measurements are taken.

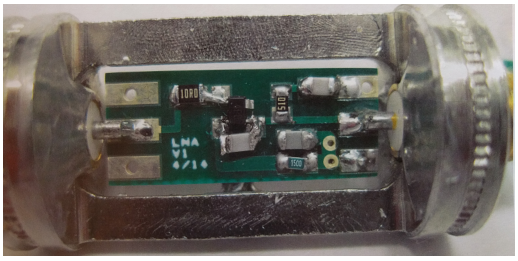

(a) Compact pcb design directly after Dicarlo et al. [114].

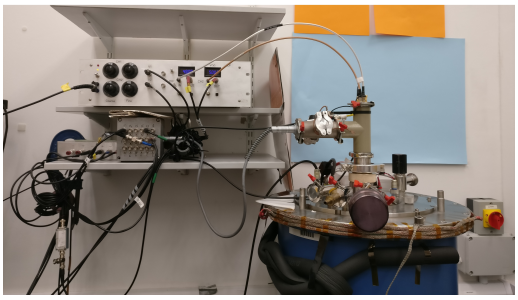

(b) Coaxial cables seen going in through top of probe and control box. Dc lines in through side arm of probe.

Figure 6.12.: Noise measurement set-up

The amplifier is small and suited to mounting inside a cryogenic probe. A control box was made in order to individually control the gain on each channel. The display panels showing the current drawn by the amplifers also proved to be useful diagnostic tool.

7. Weak localisation to probe microwave interaction

Weak localisation is sensitive to different types of scattering, which makes it useful a tool for understanding interactions in systems where it is present. Here the phase coherence and energy relaxation rate, which can be calculated from WL, were used to seek evidence of additional inelastic scattering under microwave radiation. The author of this thesis published the data summarised in this chapter [86].

7.1. Determining effective electron temperature

The resistance was recorded with ax bias current of 10nA during sweeps of magnetic field from -0.2 T to +0.2 T to obtain the weak localisation peak. This was done at a number of temperatures from 10 mK to 20 K, which are all below the Bloch-Grüneisen temperature, which is estimated as 30 K for graphene and thought to be 28 K for our particular sample (fig.7.1).

In the absence of WL the resistance is determined by temperature, so taking the value where the peak is suppressed (0.1T) and plotting this "background" resistance against the bath temperature as set by the cryostat, a calibration of the temperature of the sample was obtained.

7.2. Suppression by microwaves

In order to be able to investigate the the effect of microwave irradiation, it is necessary to determine an effective temperature for these externally heated electrons.

The effective temperature of the electrons, T_e was determined by extracting and plotting

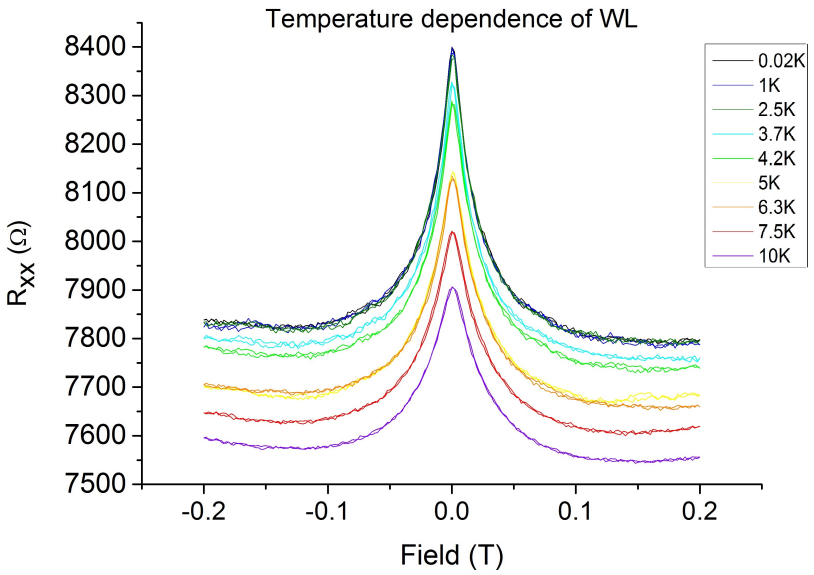

Figure 7.1.: The WL peak as suppressed by temperature. There is dc current applied here which increases the offset between the curves.

the background values for a given frequency of microwave excitation, and directly comparing it to the resistance to the plot obtained by varying the bath temperature only (see fig.7.2). The shape of the the temperatures and microwave curves is different, although plotted here against $\sqrt[3]{W}$ there is some similarity. The choice of power will be come apparent further in this section.

The size of the WL peak can be determined as the difference in the resistance found at 0T and 0.1T. Dynamic dephasing is expected to manifest as additional inelastic scattering [61, 62] and so to suppress the WL peak and reduce the phase coherence length, L_ϕ which determines the width of the peak. The elastic intervalley and intravelley scattering times which determine the shape of WL curve as described in equation (3.6) are not expected to be affected. Previous observations found that this correction was carrier density depend, but was indentifiable by a strong linear dependence on magnetic field [62]. Comparing the peak heights for irradiated and thermally heated graphene will show if the weak localisation behaviour of the sample is affected by irradiation with microwaves in a non-bolometric way.

There is no difference observed for any of the frequencies applied (fig.7.3), which indicates that there is no dynamic dephasing present and microwave irradiation only has a bolo-

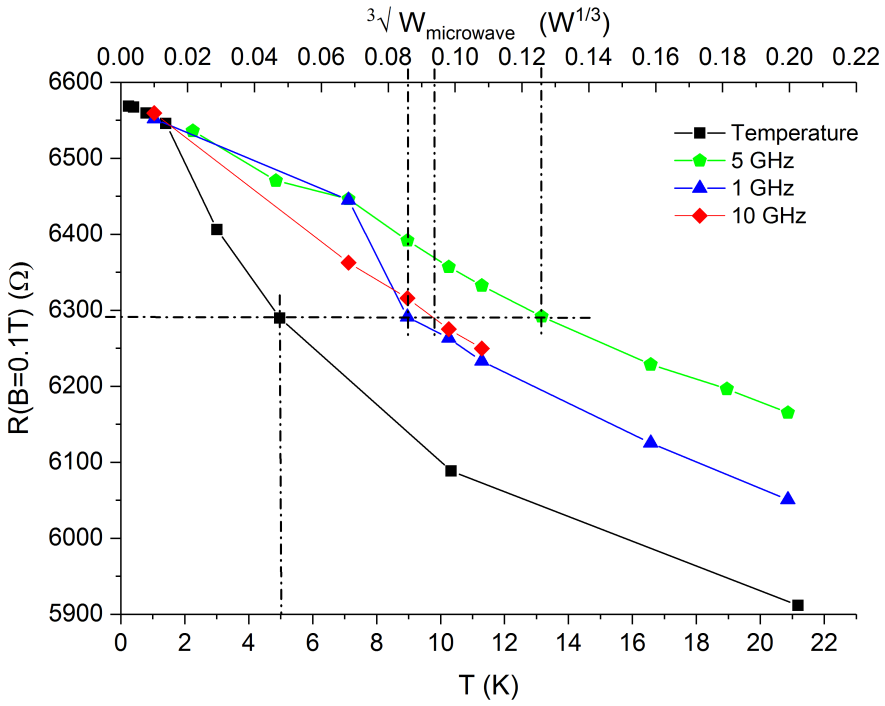

Figure 7.2.: Determining the effective temperature created by microwave excitation by equating resistance away from the WL quantum correction, R(B=0.1T) to temperature.

metric effect. It may occur in the THz region, although work carried out by Antonov in [86] does not suggest that to be the case even at 170 GHz.

The shape of the peak height against temperature is not immediately obvious, but as is well demonstrated in figure 7.3, shows an $x/sinh(x)$ dependence. This is the same dependence as the Lifshitz-Kosevich formula for extractioning electron temperature from Shubnikov de Haas oscillations (4.1).

In fact it is important to be able to plot the low temperature region well, because sometimes a saturation can produce a similar effect, or even a pronounced bend in the curve, referred to as a "knee". Such a feature is commonly observed in such WL suppression measurements at around 1 K and various processes have been used to explain it. Using low microwave power and ac current bias helps to keep T_e and bath temperature low, so the presence of knee at 3K rather than 1K suggested the presence of measurement problem. Once the grounding problem was found and rectified the full dependence was revealed as seen in (fig.7.3).

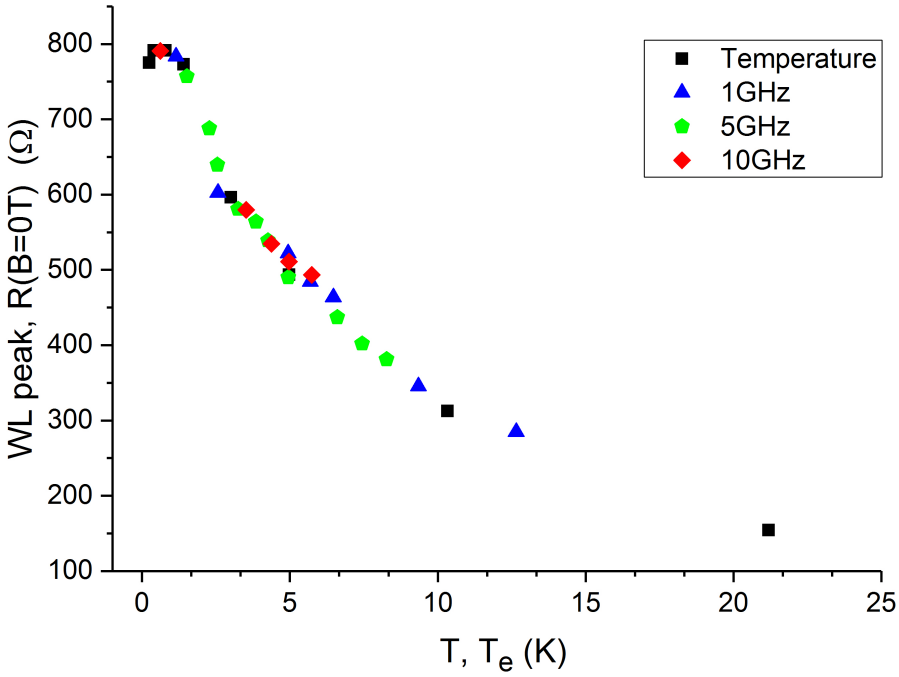

Figure 7.3.: The suppression of the peak by microwaves shows no disparity between heating by raising the bath temperature or creation of an effective temperature by microwave irradiation. This suggests that microwave excitation only results in a bolometric effect.

7.2.1. Phase coherence

The strong agreement of peak heights in figure 7.3 seems to preclude the presence of additional inelastic scattering. Fitting the WL peak according to equation (3.6) and extracting the scattering times may prove more sensitive to any effects of the microwave radiation.

The extraction of the scattering times and lengths was done using a fitting programme written in LabVIEW. It uses $\frac{\Delta\rho}{\rho^2}$ based on equation (3.6) in McCann [55] to fit the weak localisation curve. This extracts the inter- and intra- valley scattering times τ_i, τ_* and the phase coherence time, τ_ϕ.

The phase coherence time, τ_ϕ describes the time between collisions which break time-reversal symmetry. Magnetic field is the most obvious parameter to do this, but inelastic scattering such as that introduced by direct interaction with microwave photons would

also affect τ_ϕ. Plotting the phase decoherence rate (fig.7.4) showed all temperature and microwave points to fall on the same curve. This confirmed that the behaviour under microwave excitation was purely bolometric. The elastic scattering times were found to be largely independent of temperature, with a very small change at 5K.

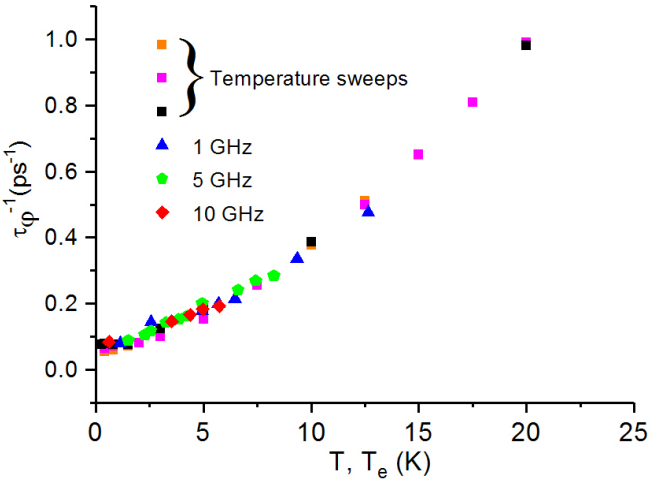

Figure 7.4.: Different sets of temperature runs represented by squares in pink, orange and black. The blue triangle is 1GHz, green pentagon 5GHz and red diamond 10GHz. As can be seen irradiation by microwaves does not result in decoherence behaviour any different to that of increasing the bath temperature.

The phase decoherence rate, τ_ϕ^{-1} is thought to be described by $\tau_\phi^{-1} = \tau_s^{-1} + AT$. Plotting τ_ϕ^{-1} on a log-log scale (fig.7.5) can establish whether the low temperature behaviour saturates and the proposed relation is correct. The constant indicating saturation, τ_s^{-1}, is thought to be due to spin-flip processes from scattering on magnetic defects. There appears to be good agreement and the values found for this sample were $\tau_s = 14$ ps compared to 50 ps in [59]. Sample dependence for τ_s^{-1} would not be surprising from spin-flip processes as they would be governed by impurities in the SiC substrate.

Further consideration of τ_ϕ, and its magnitude compared to the period of the incoming radiation can explain the absence of dynamic dephasing. τ_ϕ ranges from 1-15 ps while period of microwave radiation is between 0.6 and 7ns. There is insufficient time for additional inelastic scattering to be caused by microwaves as the inherent decoherence rate is faster. The absence of dynamic dephasing is then explained as $\tau_\phi \ll \frac{2\pi}{f}$.

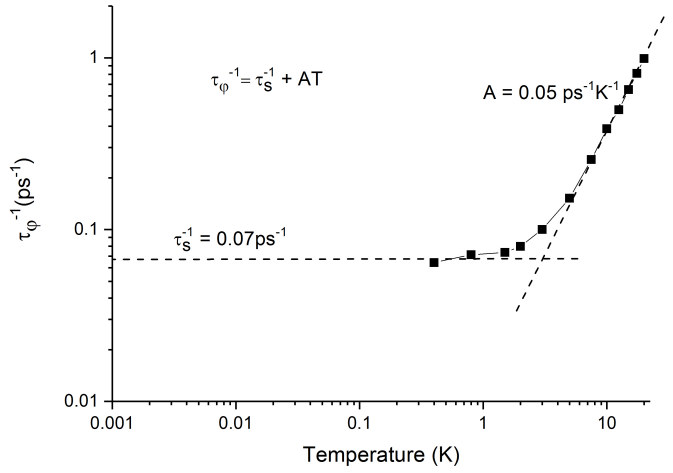

Figure 7.5.: On a logarithmic scale the same data as in figure 7.4 shows behaviour interpreted as saturation. In ref [59] this is attributed to spin flip processes. This data is for set of bath temperature measurements, but will be the same for all as shown in the previous figure.

7.3. Energy relaxation time

The energy relaxation time, τ_e can be found from the relation relating electron temperature to the power loss rate per carrier, P by equation (4.2). Since the effective electron temperature due to irradiation has been demonstrated to be bolometric, T_e will now refer to electron temperature in general, be it from raising the bath temperature, bias current or microwave radiation. Determining τ_e allows the investigation of the thermal equilibrium of the system and its processes of heat loss. Equation (4.2) is repeated here for ease of use.

$$\tau_{\mathrm{e}} = \frac{\pi^2 k_b^2 T_e^2}{3E_F P} = \frac{\pi^2 k_b^2 T_e^2}{3E_F \alpha (T_e^3 - T_L^3)} \tag{7.1}$$

Baker et al. [64] found that the power loss rate per carrier in the temperature regime below the Bloch-Grüneisen temperature followed a T^4 law. This is the expected dependence based on phase space considerations (section 4.1.1). Later measurements on graphene devices manufactured using different techniques [70] demonstrate that there is crossover to a T^3 dependence at higher temperatures; shown in figure 4.1 to be about 20K. For graphene this can be related to supercollisions [67], but a T^3 dependence has been observed

in InSb devices, as well as other materials Si, SiGe and GaAs [71]. The difference may be due to the small Fermi surface of graphene, but in these measurements despite having control over the bath temperature only a T^3 dependence was measured.

In the paper establishing the equivalency of the SdH and WL methods for finding electron temperature, it was shown that the power to be lost is dictated by the material and carrier density dependent coefficient, α [70]. As in that work, α can be determined by comparing P to (effective) temperature due to current heating. Current heating can be used to directly and bolometrically vary T_e and determine τ_e. P is energy loss per carrier, so has a denominator of nA -carrier density times device area, but since this is true for both sides of the equation it can be neglected and α can be found by plotting $(T_e^3 - T_L^3)$ against I^2R_{xx}. Applying a dc offset current to the ac current normally applied, α was found to be $5.75 \times 10^{-18} WK^{-3}$ which is of the same order of magnitude, if a bit larger than those found in [70]. This puts it in broad agreement with the Kubbakadi theory, where energy loss rate at low temperatures is dominated by deformation potential coupling [66].

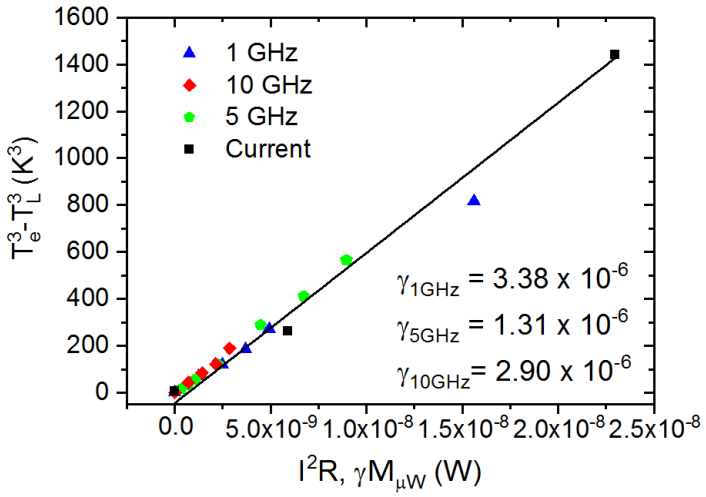

Figure 7.6.: Plotting the difference in electron and lattice temperature cubed against power with microwave irradiation needs to account for the different coupling coefficients of the frequencies. The bolometric temperature equivalence is established by determining the effective electron temperature as in figure 7.2.

Microwave heating, since it is bolometric, can be readily compared to current heating, with $P = \gamma M/nA$, with M being microwave power. As seen in figure 7.2 the different frequencies have different effective temperatures at any given power which is due to having different coupling coefficients to the sample. γ represents these in relation to current heating. Each

data set in figure 7.6) has a different slope, but by taking the ratio of the slope due to a microwave irradiation frequency to the slope due to current heating gives a measure of the different coupling coefficients. Multiplying by this then γM data will have the same slope as current heating, allowed by their bolometric equivalence.

Looking again at equation (7.1) it can be seen that when $T_e \gg T_L$, for a T^3 dependence, τ_e is a function of temperature as 1/T. For a T^4 dependence, the function of temperature would be as $1/T^2$. τ_e can calculated once α and γ are known. The 1/T dependence is clear in figure 7.7.

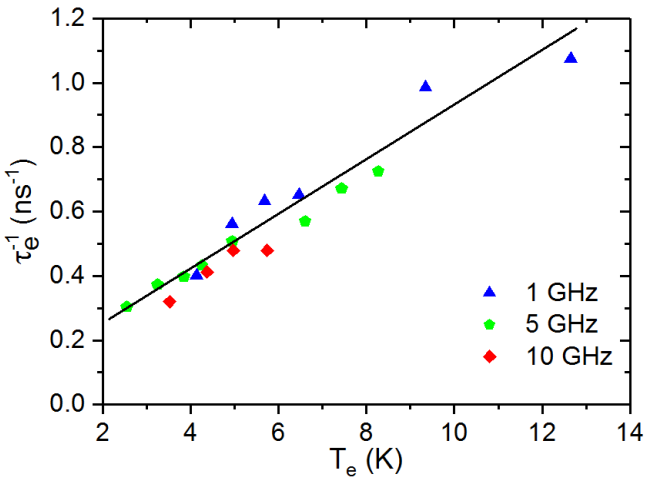

Figure 7.7.: The energy relaxation rate as a function of temperature

This confirms the T^3 dependence of energy loss rate in this sample even under microwave radiation. In addition the values of τ_e are all greater than 1 ns. This means the energy relaxation time is approximately the same as the period of the microwaves, which confirms that there is sufficient time to establish a temperature in the electron system, but not enough to introduce inelastic scattering $\tau_\phi \ll t \approx \tau_e$ [86] .

7.3.1. Discussion

Performing fitting on WL measurements on an epitaxial graphene Hall bar gave scattering times in agreement with earlier work [59], with constant elastic scattering times and a phase coherence length of about half a micron at 1K. Comparison of WL peak height due to varying bath temperature and microwave irradiation showed microwave irradiation to

have a purely bolometric effect. High frequency radiation can cause additional inelastic scattering, which by breaking time-reversal symmetry could suppress the WL peak [61, 62]. This was not observed due to the phase coherence time being much shorter than the period of the radiation, rather than a carrier density effect.

The energy relaxation time of the device was approximately the same as the period of the radiation allowing a temperature to be established and explaining the excellent agreement to bolometric behaviour with bath temperature and current heating. Current heating was used as the basis to establish the energy relaxation time under irradiation, and it confirmed the T^3 dependence of the energy loss rate per carrier. Given that the electron temperature due to radiation did not exceed about 8K, this is surprising as below 20K a T^4 dependence would be expected for graphene [70].

In graphene the T^3 dependence of the energy loss rate per carrier indicates the presence of supercollisions, which are three-body collisions permitted by disorder in the sample [67]. Alternatively, this dependence is common for other 2DEGs [71].

8. Photoconductivity of epitaxial graphene

Epitaxial graphene is a good candidate for observing cyclotron emission (CE) hotspots because of the high breakdown currents it can support, large device area compared to exfoliated graphene, and the high percentage monolayer coverage compared to CVD graphene. It is a good first step to investigate the photoresponse to confirm resonance, and also gain in situ information about the heating effects and the photoconductance.

In conventional semiconductor 2DEGs the parabolic energy dispersion form into the equidistant energy levels of a harmonic oscillator when a perpendicular magnetic field is applied. In the magnetoresistance then a set of Shubnikov de Haas (SdH) oscillations are seen as the magnetic field is increased, which then evolve into separate quantum Hall states once the spacing between the levels exceeds their width due to broadening.

If a photon of the same energy as the spacing between levels is incident on a sample, its absorption can excite electrons (holes) into an unoccupied level and this is called cyclotron resonance (CR). The corresponding reduction in transmission through a sample can be measured optically by placing a detector behind the sample. However, transport measurements can also be used, by detecting the photoinduced change in resistance. CR has been investigated in 2DEGs not only to extract information about the system, but for application purposes because the energy level spacing corresponds to the THz regime in frequency [115, 88], which is a part of the electromagnetic spectrum that is difficult to detect.

Irradiated transport measurements provide more information about the system and are easier to operate than optical measurements, but their interpretation is complicated by the magnetic field dependence of the resistance, and the heating of the electron gas.

In graphene fewer studies have been carried out. The linear energy dispersion results in a $\sqrt{B}$ dependence of energy levels in a magnetic field, so the levels are not equidistant from each other. This alters the selection rule and these transitions have been studied extensively in transmission [116, 117, 118, 119]. There have been few studies using transport

however.

8.1. Cyclotron resonance in transport measurement

Cyclotron resonance cannot be observed at exactly integer filling in a quantised 2DEG- which means that in transport measurements it will be observed in the dissipative transition regime between quantum Hall states. As such it must be distinguished from bolometric changes in resistance i.e. heating due to the irradiation of the sample. There are often features on the flanks of the QH plateaux. This area is particularly sensitive to bolometric heating due to the effect of changing filling factor on the temperature coefficient of the material [83]. Empirically, taking the difference of two magnetoresistance plots at different bath temperatures will provide this information [92]. Comparing this to the photoresponse then determines whether the response is bolometric.

Often the photoresponse is bolometric, in which case it has been found that this can be described by a single exponential decay of the energy relaxation [115, 88] and is contributed by the longitudinal component of the device resistance, with the physical parameters of the device having an important role. It has also been possible to separate out CR from a larger bolometric response, by dividing by the temperature coefficient [92].

Some earlier works found a large photoresponse centred on the plateau [120]. Subsequently these have generally been attributed to the high power of the source. Since in these cases a marked increase in the photoresponse was seen at device bias values close to breakdown, but not after, it is plausible that the irradiation pulse causes breakdown in this situation resulting in significantly increased photoresponse.

Later investigations showed that pulses can cause momentary breakdown, which then result in multiple decay times [121]. Interestingly, in these situations a CR response was identified a bit further away from the flank of the plateau than the bolometric one. It was attributed to a photoinduced Hall current forming across the localised bulk region, and so being of transverse origin. However, longitudinal contributions can easily dominate a system.

Studies on graphene have been less extensive and have primarily been on two contact devices. Deacon et al. showed photoresponses which correlated to the energy level spacings of the linear dispersion of monolayer graphene, using a gated device [94]. Their photoresponse was one large peak, very broad in magnetic field. The breadth is understandable

to some extent due to the large spacing between the N=0 and N=1 Landau levels. A small negative response is also observed, but is not discussed [93]. The power used is low, but the device area is small too.

A bolometric response has been found to be viable up to even liquid nitrogen temperatures [89], but this time flanking the plateau as is commonly found in AlGaAs/GaAs heterostructures. Measurement by Watanabe et al. on a high mobility device thanks to its h-BN substrate found bolometric, and also reported CR photoresponse across the width of their plateau by varying their gate voltage [122].

8.2. Photoresponse in epitaxial graphene

The measurement undertaken here differs from most previous ones in a number of ways. A 4-terminal configuration is used, rather than a 2-terminal one, with a lock-in amplifier measuring across longitudinal voltage probes. The source of radiation is not a high power laser, but a quantum cascade laser diode. It has a divergent output, acting almost as point source, which means that although mW are observed with a collecting lens, only a fraction of that travels down the optical fibre, allowing at most hundreds of μW to be emitted. It is not possible to maintain this is alignment during the mounting of the probe into the cryostat, and the amount incident on the sample is further reduced by the position of the fibre relative to the device. The source is not broadband, but is not entirely fixed, with the exact wavelength being affected by the laser diode bias current. Even at the maximum possible power, the greater size of these EpiG devices puts the irradiance within a factor 10 of the output value used by Deacon et al. Mechanical chopping was not possible, so the cw power output of the laser is changed by modulating the laser diode bias current.

Figure 8.1 shows R_{xx} vs B and the photoresponse vs B together. Comparing the photoresponse curves to their corresponding resistance curves shows that there is a feature in the vicinity of the Shubnikov-de Haas (SdH) oscillation and that there is no photoresponse on the plateau. The plateau corresponds to exact $\nu = 2$ filling, but unfortunately despite becoming minimal, the longitudinal resistance never vanishes completely and so the device cannot be said to be fully quantised. The response is observed on the slope of R_{xx} down to the plateau. For the N=0 $\rightarrow$ N=1 LL transition the energy difference is of order 124meV which in wavelength is 10μm. In order for it to be possible to observe the transition, the carrier density needed to be less than $5.3 \times 10^{11} \mathrm{cm}^{-2}$. Depending on the exact wavelength it varies, but the CR was expected at 9T.

The photoresponse curves are plotted on a log scale in order to be able to present the results for the two diodes at the same time, which is necessary because the photoresponse to 5µm irradiation is so much smaller than for 10µm. The response to 5µm radiation is consistently two orders of magnitude smaller than to 10µm radiation, which does not correspond to either the power difference of the laser diodes or the energy difference of the photons. It was found that the photoresponse was much bigger with 10µA bias current than 1µA and with the laser power modulated at low frequency.

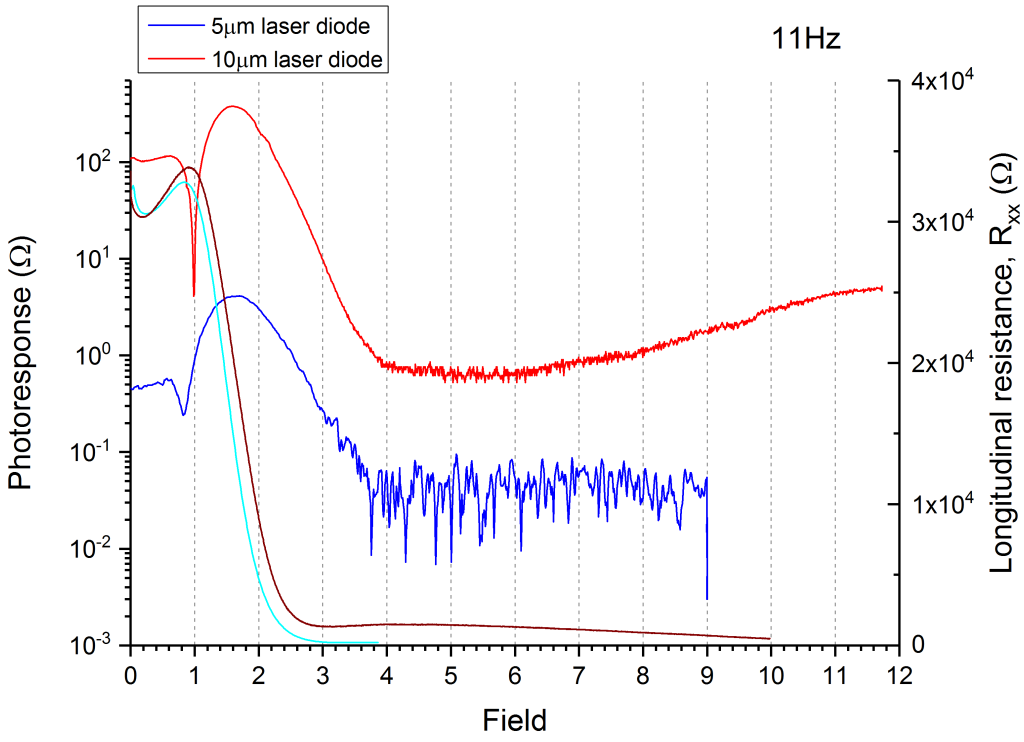

Figure 8.1.: Response to 10µm and 5µm radiation with 10µA bias current measured with a lock-in amplifier at low frequency (11Hz). The longitudinal resistance curve is included to demonstrate the behavioural regime of the sample. There are two sets because the data are from different data runs, with different carrier densities. The 10µm response curve is unusual because it has some response at high magnetic field.

There is a similarity in the shape of the magnitude of the photoresponse curve to the longitudinal resistance curve, that is partly obscured when plotted on a logarithimic scale. The strong response seen at the SdH oscillation prior to entering the plateau, is similar to, but does not correspond well with the bolometric response observed at the edges of conventional 2DEGs. This is due in part to the unusual and broad features of magnetore-

sistance in epitaxial graphene, compared to the many narrow features of gated graphene devices or those of materials with parabolic energy dispersions.

In order to understand this unusual photoresponse it is not sufficient to only study it in isolation, but to examine the dc transport measurements and to correlate the two.

8.2.1. Origin of the photoresponse

The graph (fig.8.2) shows the R_{xx} curve taken at two device bias currents, 1μA and 10μA, with the laser off (black and blue lines), and with the laser on at a high power setting, but unmodulated (green and red lines). The laser power was unmodulated because when measuring with the DVM there is no benefit to having an ac component present. It has previously been verified that additonal ac modulation can cause a small difference in the resistance, but that change is small and not necessarily consistent across measurements, and so was omitted for simplicity. The high power setting (dc diode bias current 980mA) was designed to compensate for the absence of modulation as it has the same the maximum power value as achieved with modulation (dc940mA plus ac40mA). In this way this data gives the maximum possible change in longitudinal resistance as a result of irradiation with this 10μm laser diode.

As can be seen there is one SdH oscillation present before the device enters the $\nu = 2$ plateau at about 4T. This is not unusual for epitaxial graphene devices due to the pinning of the Fermi level [123].[1]

The higher current of 10μA reduces the overall resistance of the device. The lower value of the SdH peak (and WL feature) indicate that this is due to heating of the electron system. At both currents, irradiation has a qualitatively similar effect to current, albeit much smaller in magnitude. However, in addition to suppressing the SdH peak by heating, the oscillation is also shifted in magnetic field. The SdH maximum is shifted by a small amount (≈ 0.05T) even by irradiation, although due to the broad nature of the maximum this is more clearly seen on the straight slope prior to the $\nu = 2$ plateau than at the maximum. This shift in magnetic field position is indicative of a change in carrier density. Although this is surprising, it is more plausible for epitaxial graphene than it would be for devices made of other 2DES. It is now known that there is charge transfer from the substrate

[1] There is also a peak near B=0. After due consideration this is taken to be a weak localisation feature, but it is unusual in its size, asymmetric shape and peak not being at exactly B=0. For these reasons it is not used as a measure of electron temperature.

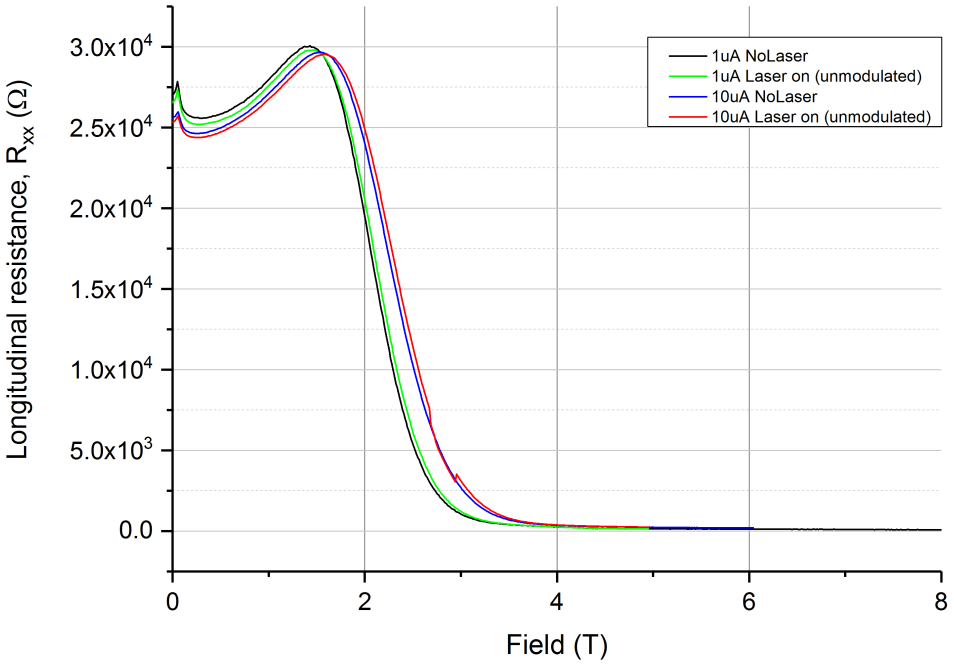

Figure 8.2.: R_{xx} with and without laser irradiation at 1μA and 10μA bias current. Increasing the current reduces the resistance and alters the SdH oscillation. The plateau is not fully quantised. The change in resistance due to irradiation gives no indication of the observed difference in photoresponse.

at the pinned Fermi level i.e. allowing the $\nu = 2$ plateau to extend to extremely high magnetic field [51, 95]. While there has not previously been evidence of charge transfer in the SdH regime, the carrier density is not fixed by an electrostatic gate as would be the case for other materials.

When investigating the photoresponse in a 2DES it is usually sufficient to be interested in the magnitude of this response. However, in these measurements the magnitude appears to give a feature with a small peak preceding the larger one, with a minimum between the two at approximately the maximum of SdH oscillation (fig.8.3). The position in magnetic field of the photoresponse raises questions as to its nature, not least because a response is often seen at the edge of the quantum Hall plateau. As a change in resistance, the photoresponse could then either be equivalent to the derivative of the slope, or a simple difference i.e. between the two curves.

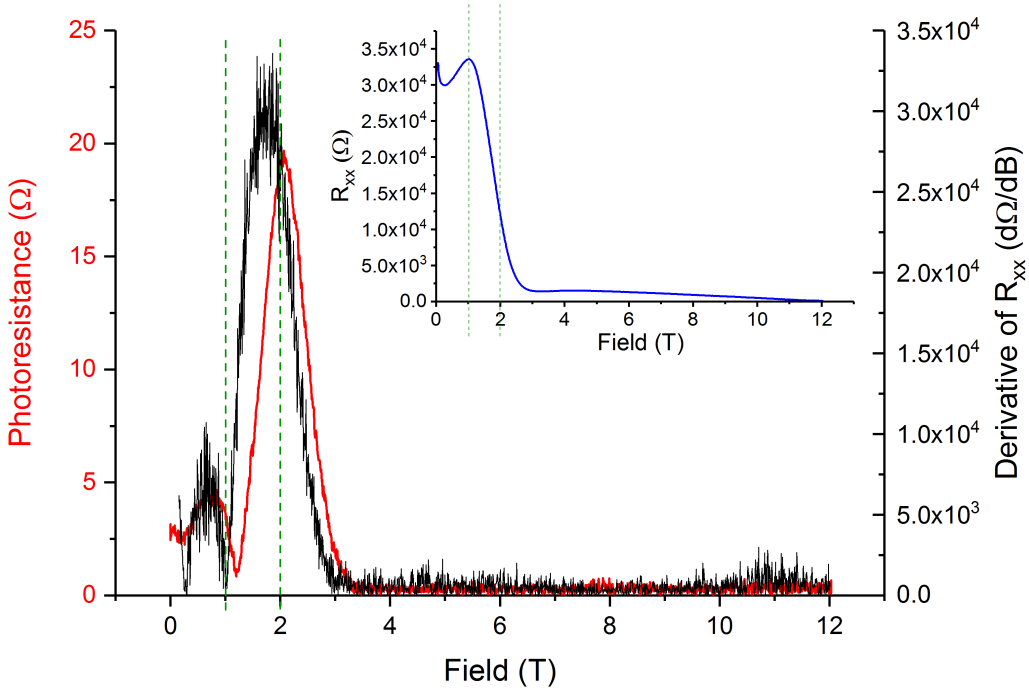

Figure 8.3.: Comparing the derivative of R_{xx} to the photoresistance (both absolute values here) shows the same shape, but that the curves are offset in magnetic field. The photoresistance was taken with 1μA bias current and low power modulation. Inset:R_{xx} included for reference, with markers for the SdH maximum and 2T.

Comparing the magnitude of photoresponse in terms of resistance (lock-in voltage divided by device bias current) to the magnitude of the derivative calculated for the longitudinal resistance at 1μA bias current shows that the features agree in shape, but not in magnetic field position (fig.8.3). Agreement in this respect is more important than usual, due to the observed increase in carrier density (fig.8.2). At 10μA bias current the photoresponse is broader and so the difference with respect to the derivative is reduced.

It can be seen by measuring in the (X, Y) configuration of the lock-in amplifier (fig.8.11) that the photoresponse happens predominantly in the real component, X, but crosses zero creating two peaks when the modulus is taken. In the (r, θ) configuration this more clearly manifests as an abrupt change in phase of the signal. Taking a simple difference in R_{xx} with and without the laser produced curves which reproduces this shape (fig.8.4), demonstrating that the photoresponse originates from the change in resistance between

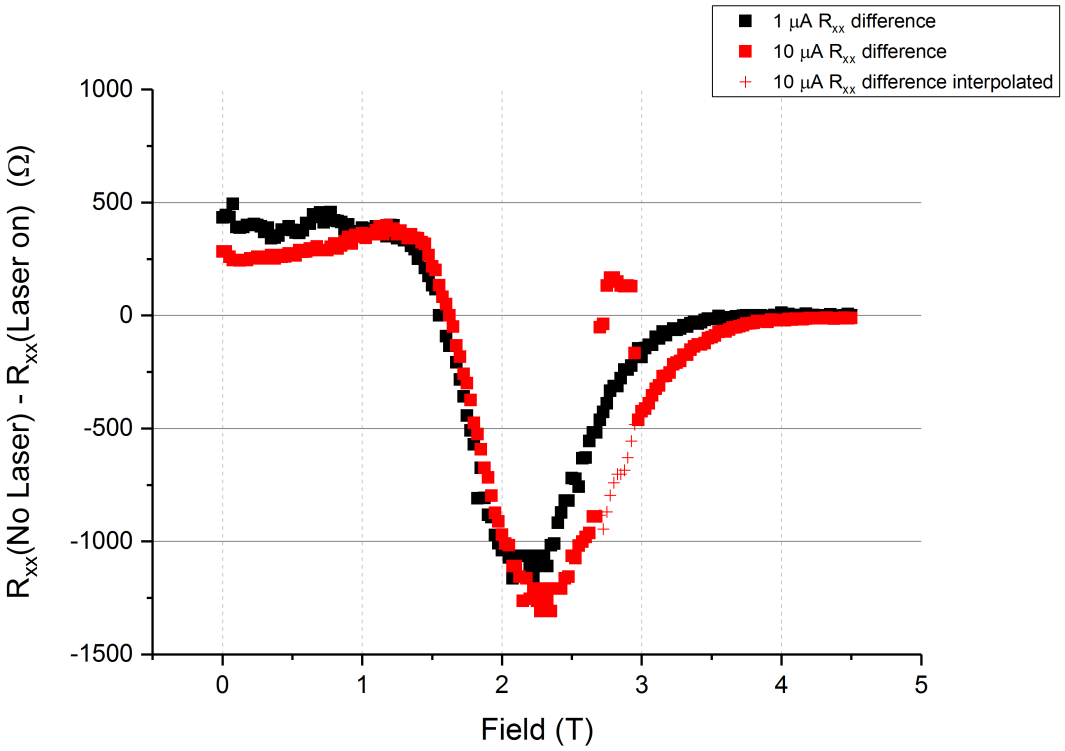

Figure 8.4.: R_{xx} due to irradiation subtracted from R_{xx} without the laser. The difference curve is identical to the dominant component of the lock-in voltage (fig.8.11)

the irradiated device and what it would otherwise be. However this difference has to be taken very carefully at exactly matching values of magnetic field because the slope of magnetoresistance is so steep (30Ω/mT) that even small deviations in magnetic field or inaccuracies in determining the resistance value introduce errors and can alter the difference value found by hundreds of ohms.

Usually, in gated devices, the SdH oscillations line up well in magnetic field and the amplitude of the oscillation is reduced by temperature or bias current. In that case the shape of a difference curve would not be expected to look like it does here for epitaxial graphene. The correspondence of the difference curve with the real component of the photoresponse signal is strong enough evidence to put the origin of the photoresponse in the difference of resistance in the device when irradiated. However, the much greater size of the photoresponse at 10μA indicates the explanation is incomplete.

Comparing the absolute value of the difference in resistance when irradiated to the per-

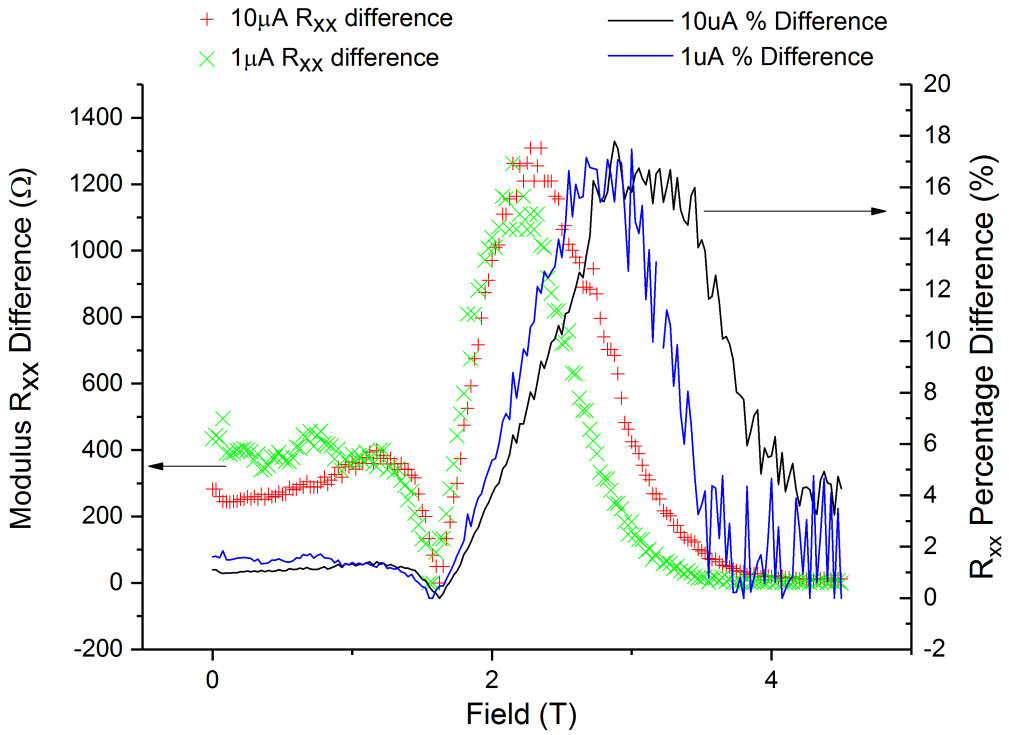

Figure 8.5.: The highest percentage change occurs at unexpectedly high magnetic field. It does not coincide with the maximum difference in resistance. It is also found that percentage change in resistance due to irradiation is the same for the two bias currents, despite the photoresponse at 10μA being larger.

centage change in resistance, it is notable that the biggest percentage change occurs at higher magnetic field values, rather than at the maximum difference (fig.8.5).

Even accounting for the fact that the total change in resistance needs to sum the positive and negative components, the change in resistance at 10μA is only a few hundred ohms greater than for 1μA. These changes in resistance amount to the same percentage change in resistance, compared to the zero field resistance at these currents. This is surprising considering the orders of magnitude difference in photoresponse at these two currents recorded with the lock-in.

The position in magnetic field of the greatest percentage change in resistance emphasises that the relative shift of the two curves is responsible. This is evident when the difference is overlaid with the longitudinal resistance curves (fig.8.6): the difference is approximately constant until it is reduced as the curve with no irradiation reaches its peak, then becomes

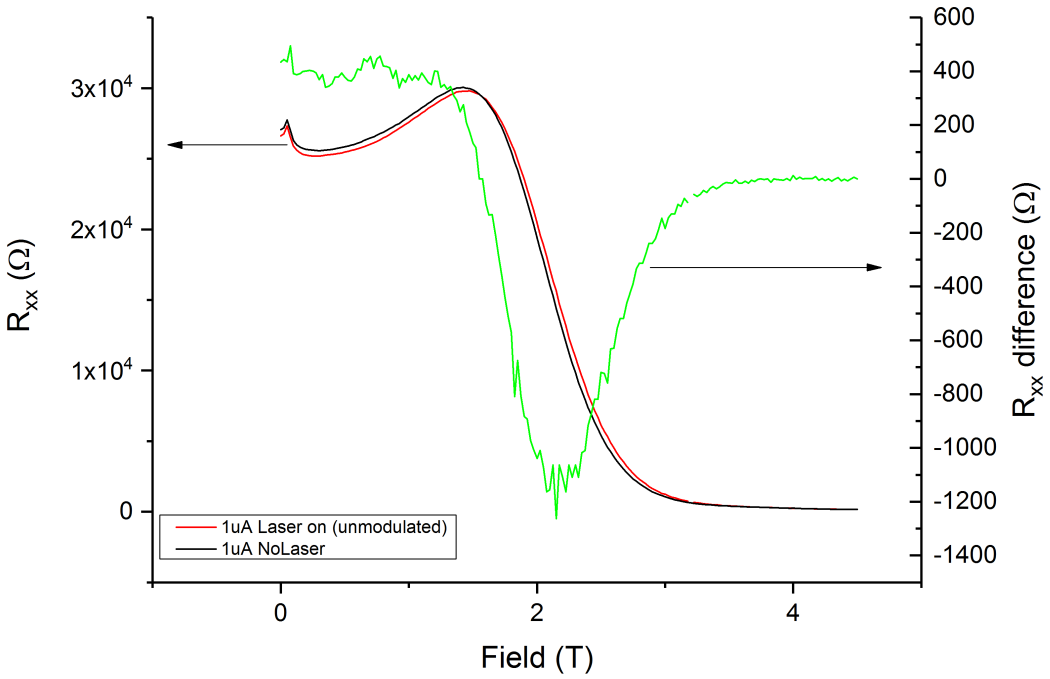

Figure 8.6.: The difference in resistance (green line) due to irradiation is approximately constant until the resistance maxima begin to crossover, which leads to a large negative difference, which decreases once the resistance curves begin to converge near the plateau.

negative once the two curves crossover.

By shifting the irradiated R_{xx} curve so that its maximum aligns in magnetic field with the maximum of the curve without the laser, the resulting difference curve provides a baseline for what would be the case in more usual data. The curves in figures (fig.8.7a) and (fig.8.7b) are unaltered difference values rather than the modulus. The minimum arises due to the two resistance curves getting closer together near their maxima. The irradiated curves are not broader than the unirradiated ones as clearly seen visually when they are shifted together, and by the positive difference values. However, there is a change in shape, an effective broadening of the whole SdH oscillation when it is left unshifted because the oscillation is not segregated from the data before it. Except for a few negative values as the curves converge near the plateau, all the difference values are positive. The resistance of the plateau is higher when irradiated which causes the negative values (fig.8.7a, fig.8.7b). The percentage change in resistance is not the same for the two bias currents bias current

with the SdH maxima aligned. In addition, the biggest difference in resistance now occurs at the start of the slope of the SdH oscillation and decreases as the curves converge, rather than occuring right at the base of the slope near the plateau. This shows that the position of the photoresponse as compared to the resistance or its derivative is due to the change in carrier density.

Comparing the difference for the shifted difference curve to the original difference curves shows a significant, qualitative change in shape. It is also clear that shifted difference curves are much smaller.

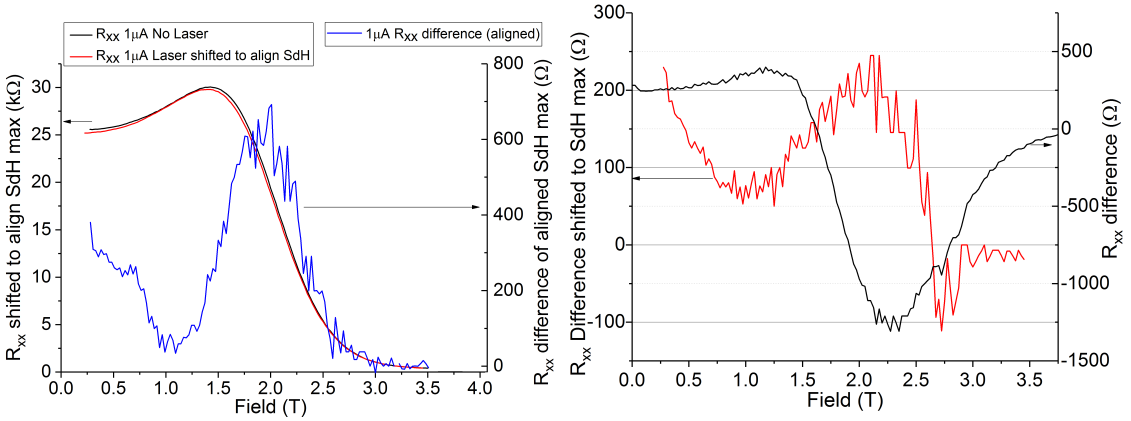

(a) 1μA bias current. The irradiated R_{xx} curve is shifted down in magnetic field to align the maxima of the two curves. Taking the difference in this way demonstrates a more usual difference behaviour.

(b) 10μA bias current. Comparing the absolute value in R_{xx} difference with the difference from aligned curves shows the dramatic alteration in shape and magnitude, despite the maxima misalignment being small.

Figure 8.7.: R_{xx} difference with SdH peaks aligned

Having determined the origin of the photoresponse to be due to the change in resistance under radiation, and its position in magnetic field to be due to the change in carrier density, it would be preferable to have a faster and more succinct method for showing the nature of the response. Although in this measurement system there was no way to vary bath temperature, by taking the bias currents to establish different effective electron temperatures an analysis like that by Horstmann et al. [92] can be performed. In this case the difference in resistance at 1μA and 10μA will give an uncalibrated temperature coefficient, but it should still suffice for removing bolometric effects from the photoresistivity.

Two tests are possible. One is to divide the resistance under unmodulated irradiation by the effective temperature coefficient. This is not an exact replica of what was perfomed

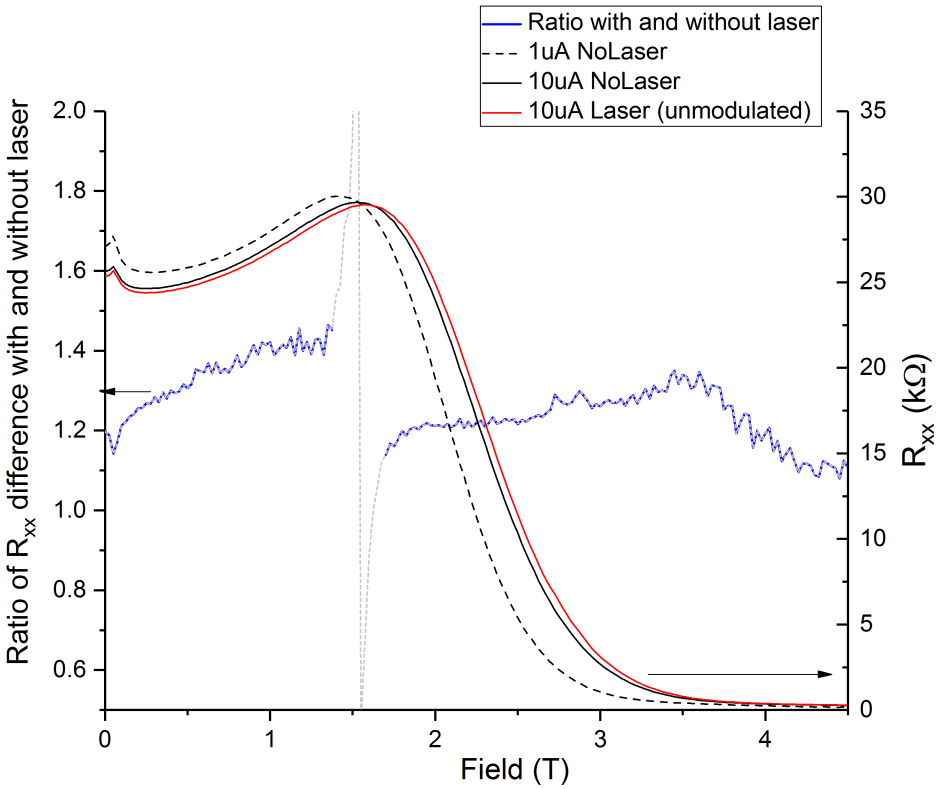

Figure 8.8.: Taking the ratio of the difference due to irradiation minus a low current to irradiation at a higher current should reveal any features obscured by bolometric heating. The absence of any features shows the photoresponse to be bolometric in origin. Using the two different currents helps to take account of the temperature coefficient in a similar way to Horstmann et al. [92].

previously in [92] because the numerator is DVM transport not photoresponse from a lock-in, but as the maximum possible resistance change is seen under unmodulated irradiation it sets an upper limit. The other is to divide modulated photoresponse in terms of photoresistance by the effective temperature coefficient. In both cases the small features that remain correlate to the behaviour of the resistance, with the only sizeable feature being the divergence at 1T due to the curves crossing each other and the difference subsequently going to zero.

Making an alteration to the method to find a ratio of the difference in resistance when irradiated and not can provide greater sensitivity and applicability to both modulated and unmodulated situations. Rather than dividing the resistance or photoresistance by the difference in resistance at two (effective) temperatures, this means taking the difference when irradiated from the lower temperature and dividing as before by the difference at the

two temperatures. The bolometric nature of the photoresponse at low magnetic field is shown in (fig.8.8) using this ratio: R_{xx}(1μA No Laser) - R_{xx}(10μA Unmodulated Laser)/ R_{xx}(1μA No Laser) - R_{xx}(10μA No Laser).

For Horstman et al. removing the bolometric contribution revealed a previously obscured CR signal, but as can be seen here there are no features remaining (once the divergence where curves cross is accounted for).

8.2.2. Properties of the photoresponse

The photoresponse on the plateau can be said to have been generally featureless, like curve (2) in (fig.8.9) where the data was take in two parts to increase the sensivity for the measurement of the plateau. Curve (1) is the one presented at the start of the chapter in (fig.8.1) because it had the largest photoresponse observed, together with usual transport data. Curves (1) and (3) show some of the unusual features that were observed. The carrier density is a possible factor in these behaviours, as it was changed between measurement runs. The carrier density values for curves (1) and (2) are estimates due to unusual features in their V_{xy} curves, which means that based on more usual data, curve (2) is actually likely to have had a carrier density a factor of 2 smaller: $3 \times 10^{10}\text{cm}^{-2}$.

Curve (3) with its much lower carrier concentration has a low Fermi energy $\sim$ 7meV. Not only is this much lower than the 20-30meV seen for the rest of the data taken, but it approaches the level of electron-hole puddles that occur near the Dirac point in graphene. The high photoresistance is reflected in the high longitudinal resistance (2kΩ at 3T up to 3.6kΩ at 11T) in this measurement. However, unlike the bulk the resistance which increases smoothly, the photoresistance has small increases which were somewhat reproducible and these could be indicative of new conduction paths being created. Similar photoresistance was seen using a 2-terminal configuration at a higher carrier density where the resistance was known to be 26.5kΩ.

The photoresponse seen at high field (fig.8.9)in curve (1) does bear a resemblance to the wide resonances seen in the work by Deacon et al. [94]. If it was considered to be a peak centred at 12T, it would however be even wider, 8T, compared to the 4T widths seen in [94]. It is not possible to say whether the rising low level response at high field reaches a maximum at 12T for certain. Furthermore at a photon energy of 124meV the resonance would be expected at 9T.

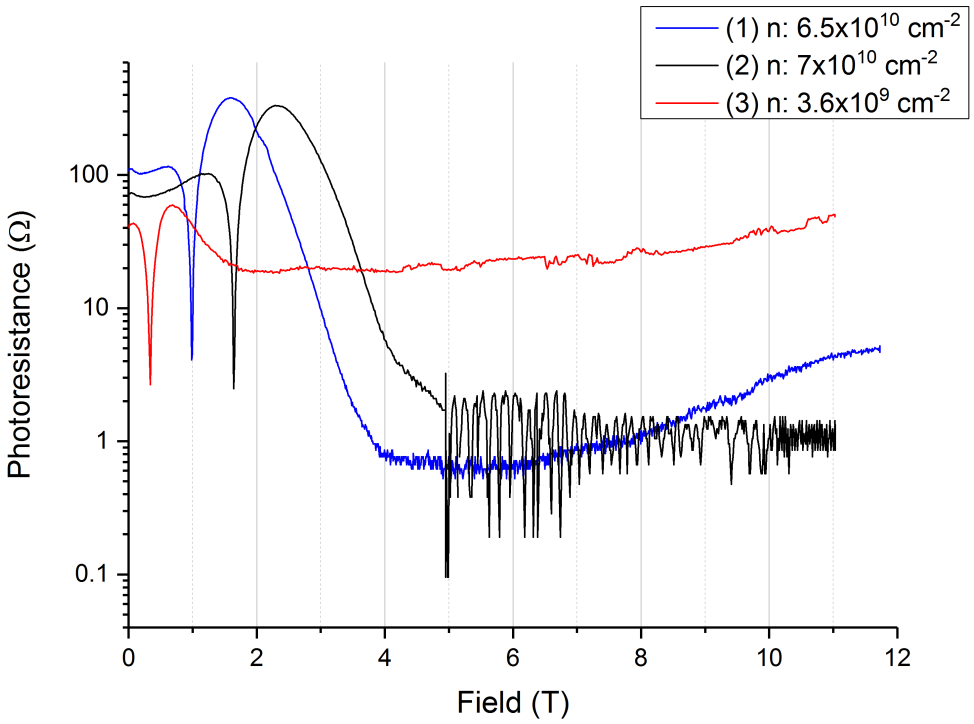

Figure 8.9.: A typical response curve (2) contrasted with one at low carrier density (3) and one with a rising response at high field (1). (2) was measured in two parts in order to increase sensitivity on the plateau.

Other possible explanations relate to the substrate. SiC has a restrahlen band, with anomalously high reflectance occuring at 10µm. Data was taken using irradiation with 5µm laser diode to investigate whether this was having an effect, however the wide rise at high magnetic field was not observed again with either diode so the cause could not be determined. The data under 5µm irradiation showed the bolometric effect seen with 10µm irradiation and no other features, but all signal was orders of magnitude smaller. Since coupling, photon energy, diode outpower all play a role in the different magnitude of the photoresponse seen, it has not been possible to establish if the restrahlen band also contributes.

Charge transfer from the substrate could be a possible contributing factor. However, the recent work in quantifying the charge transfer would indicate the opposite, instead maintaining close to exact filling [95] and thus facilitating the long plateaus seen in EpiG Hall devices [51]. In fact, the persistence of integer filling is the best estimate at this time

for the absence of large photoresponse like that in Deacon et al. [94]. Although Watanabe et al. have claimed to see a (much smaller) cyclotron resonance based photovoltaic response [122] it was not discernible in the presence of dc bias current at 5K which is the closest approximation to the data here.

8.2.3. Current dependence of the photoresponse

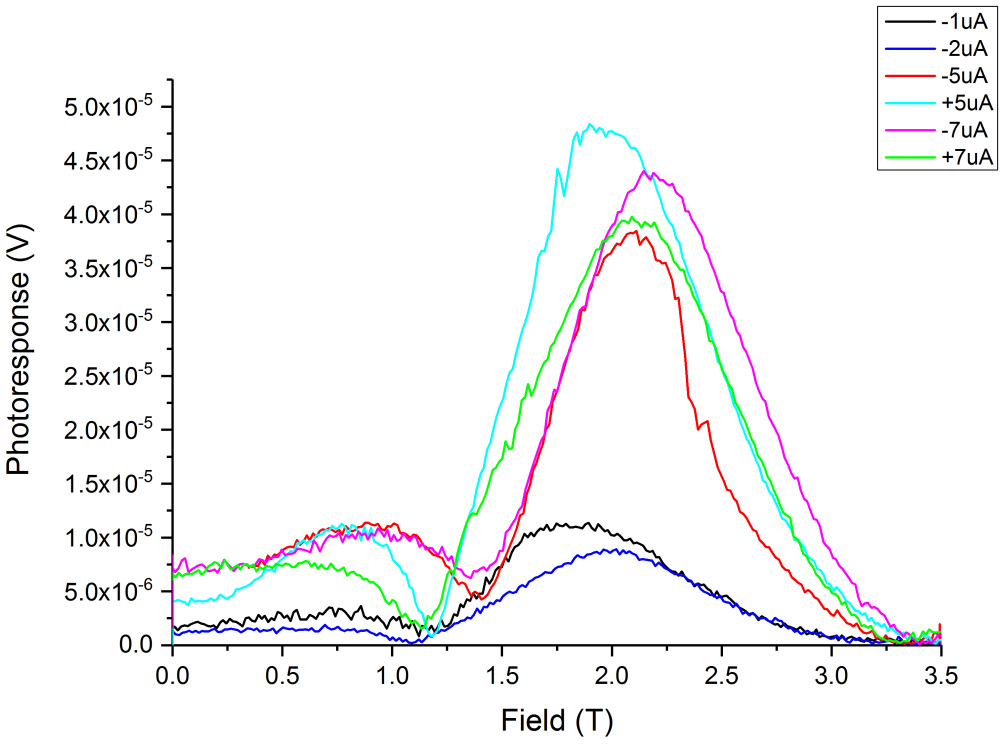

Figure 8.10.: The current dependence of the bolometric photoresponse was investigated using low power modulation. These measurements were taken at high frequency ac modulation (∼3kHz)

Applying increasing bias current is usually a good way to establish a temperature dependence, by establishing equivalence with Joule heating. Unfortunately the dependence of response on current is neither straightforward, nor is it universal across data runs.

The features of the dominant component reverse sign when the bias current is reversed, a common bolometric response trait. At one particular power setting (and therefore wavelength), the negative and positive parts of the component were more equal in size and the resulting response curve had two humps instead. This shows that the shape of response

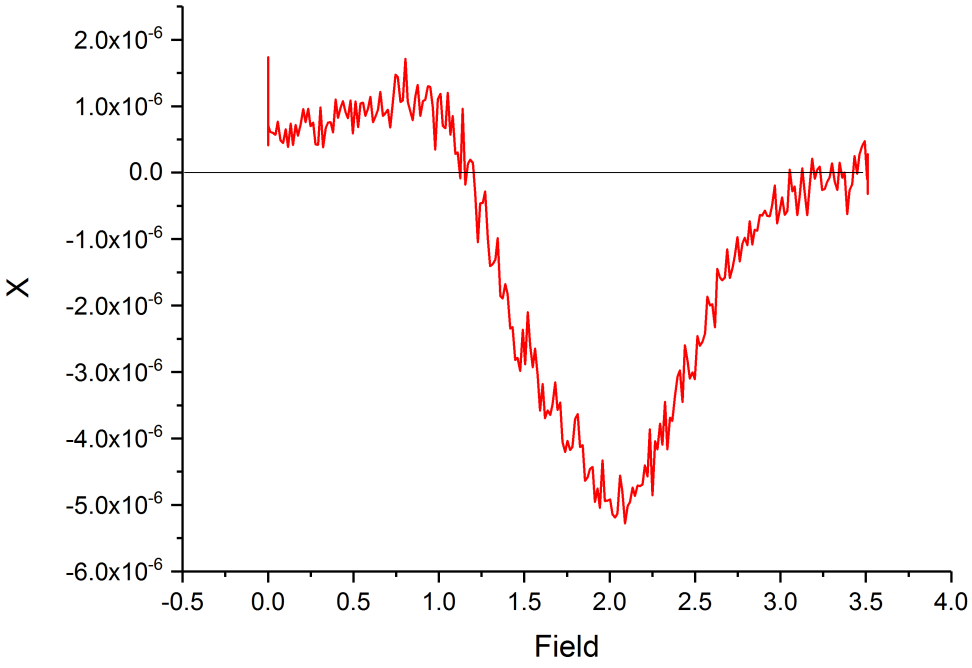

Figure 8.11.: The dominant component of lock-in voltage has a strong magnetic field dependence. The shape is found to correlate difference in R_{xx} due to irradiation (fig.8.4). This was taken at low power modulation, but the shape is unchanged at higher modulation or bias current.

and so presumable the difference in resistance due irradiation can be altered.

The dependence of photoresponse on device bias current was investigated using small modulation of the power around the usual mid point of the diode, resulting in low overall power and small modulation of the power. It can be said that in general the magnitude of the signal increased with bias current, and that reversing the current direction produced a slightly smaller response (fig.8.10). 5μA and -2μA showed deviation, with the former significantly larger than expected and the latter smaller. However, bearing in mind the real value of the response and its origin, a proper evaluation of the response needs to take the total response into account (fig.8.12a) [2]. The total response is usually larger than the peak, but the amount varies depending on the amount of offset in signal recorded (which also explains the slight decrease in the total response for -7μA).

[2] When evaluating the total response from magnitude of response data this means adding the value of the smaller peak to the larger one, but also subtracting the value of the "minimum" between the two.

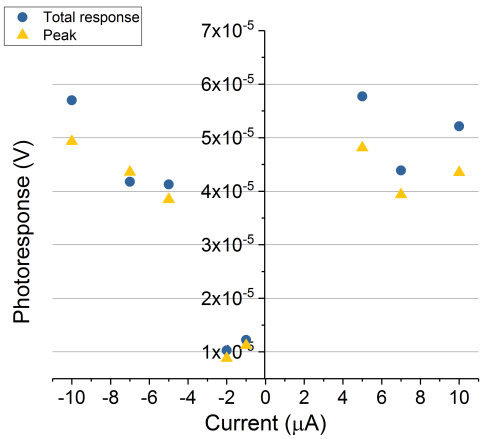

(a) The photoresponse increases with bias current. A linear dependence is possible but results in many outliers.

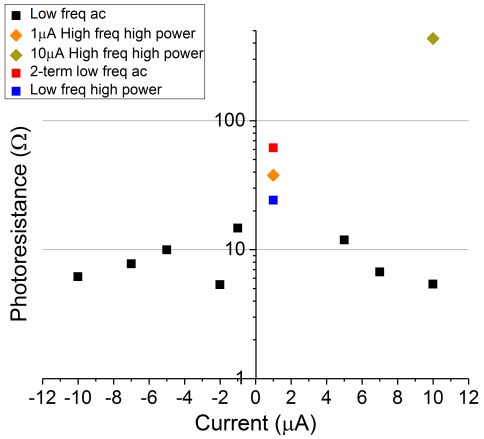

(b) The diamond points are data collected at low frequency ac modulation and show much greater photoresistance as well as increase with bias current rather than decreas as at high frequency modulation.

Figure 8.12.: Current dependence and effect of frequency of ac modulation

The photoresponse in volts is significant because of the signal to noise ratio, but as a physical interpretation the photoresistance can be more interesting. The increase in response does not does not keep pace with the increase in current (fig.8.12b), so in terms of a photoresistance the response seems to be decreasing (14Ω at -1μA to 6Ω at -10 μA). However, these low excitation measurements were taken at a high frequency ac modulation (∼ 3kHz), whereas much a greater signal was obtained at low frequency (11Hz). Measuring at low frequency ac modulation, increasing the current consistently increased the size of the response recorded. The increase from 1μA to 10μA increased the signal by two orders of magnitude, and so the photoresistance by a factor of 10. At low excitation there had been no indication of anything but a weak dependence of signal on modulation frequency.

The photoresistance plot shows low frequency measurements with squares and the high frequency ones with diamonds (fig.8.12b). The highest signal obtained at 1μA with larger modulation and so excitation comparable to the high frequency measurements is included for comparison as is a 2-terminal measurement at high excitation which gave the largest signal recorded for 1μA at low frequency modulation.

Considering the clearly bolometric nature of the low field response and the demonstration of its origin as due to the difference in resistance and altered carrier density under irra-

diation, it is still not clear why there is such a significant increase in photoresponse with bias current when measured at low frequency ac modulation. For a future application as a bolometric detector, such as that by Kalugin et al. [89], this could warrant further investigation.

Effect of dc current

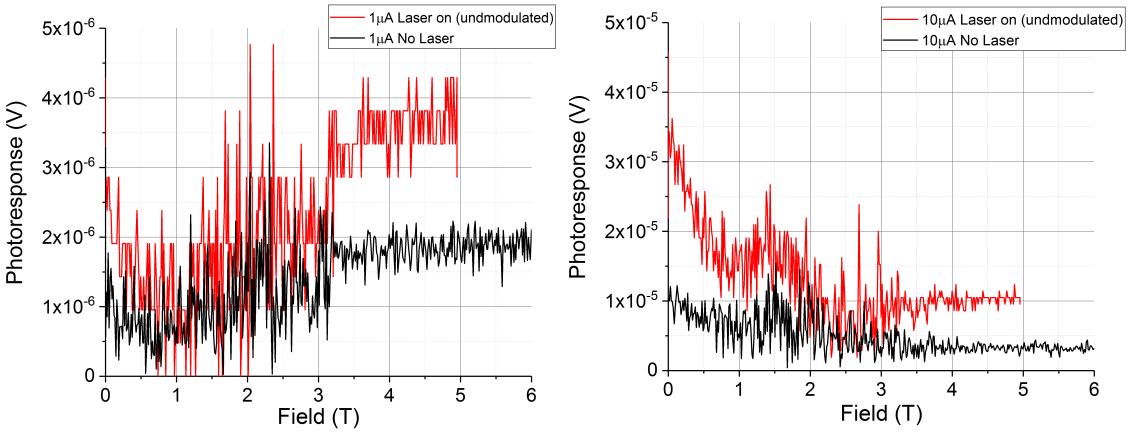

(a) The photoresponse at 1μA bias current increases with magnetic field until the plateau is reached.

(b) The photoresponse at 10μA bias current decreases with magnetic field until the plateau is reached and is most noisy in the region of the SdH oscillation. This becomes pronounced under irradiation.

Figure 8.13.: Photoresponse to unmodulated laser recorded on lock-in

The suppression of resistance by increased bias current, but particularly the alteration to the SdH oscillation is of significance in these measurements of photoconductivity in epitaxial graphene. Investigations have been carried out in semiconductors 2DEGs regarding the suppression of resistivity by the application of an electric field in the presence of a strong magnetic field [124]. In these works extra oscillations were also present in the magneto-oscillations [125, 126]. The latter are clearly absent here, as they were for Tan et al. [65] yet they still attribute the inversion of their SdH maximum with increased bias current on their graphene device to altered transport due to the electric field of the dc current.

Photoresponse data was recorded for resistance measurements irradiated with unmodulated laser power. Of course, in the absence of modulation the photoresponse data is very noisy, and in fact without modulation the “locked-in” frequency has no significance so any

similarities are coincidental and the data would be discarded. Nonetheless some features were discerned, and it seems to illustrate a qualitative change in behaviour between 1μA and 10μA (fig.8.13a, fig.8.13b).

It is known that there is inhomogeneity in the device and that the contact resistances are poor. However there were also unusual non-linear I-V characteristics with a magnetic field dependence that were recorded, which also suggest a change in transport.

Whether due to charge transfer, or an alteration in electron diffusion by the electric field [126], it seems that the photoresponse, especially when the laser power is modulated to simulate chopping, amounts to a change between different energy distributions in the device.

8.3. Discussion

A sizeable photoresponse was observed at low magnetic field, with no significant features found on the $\nu = 2$ plateau (fig.8.1). This was found to be bolometric in nature, but significantly affected by a small misalignment in the SdH oscillation under irradiation (fig.8.2). The misalignment indicates a change in carrier density, or perhaps an alteration to electron diffusion [65, 124]. Since it is now known that in epitaxial graphene the breadth of the $\nu = 2$ plateau is due charge transfer maintaining integer filling [95], rather than other mechanisms found in conventional 2DEGs, this could potentially be of interest in the future, especially where dc biasing is unavoidable as it was here.

It is unclear whether the bolometric effect is linear in current, but the components reverse with negative bias current showing at least that much agreement with other works [122, 121, 115, 88]. Further investigation is needed into the frequency dependence, but it is likely that as long as one component dominates the lock-in signal a simple dependence will be found. If the components are altered the shape of the photoresponse is altered significantly.

The absence of a photoresponse such as that seen by Deacon et al. is not clear [94], although the persistent integer filling may be the cause. The presence of photovoltaic response on the plateau such as that seen by Watanabe et al. [122] cannot be ruled out as it would not be expected to be seen at 4.2K. No CR resonance away from the flank of the plateau was observed [121, 115], but the width of the plateau, absence of electrostatic

gating and the high photon energy required for graphene do not make epitaxial graphene the ideal material for observing that type of response.

The bolometric photoresponse was found to correspond to the difference in resistance due irradiation. However, the magnitude of the resistance differences at different bias currents does not fully account for the magnitude of photoresistance obtained. Whether there are any transverse components contributing could not be studied in time, but the change in transverse resistance due to irradiation is less than 1% greater at 10μA than 1μA bias current.

These measurements verified the robustness of the corona discharge gating against external radiation, as well as providing unique information on epitaxial graphene, but also suggesting a technique other than cyclotron emission would be better for investigating quantum Hall breakdown.

9. Noise measurement in the quantum Hall regime

Schurr et al. [97] demonstrated that at equilibrium the noise of 2DEG corresponds to its macroscopic resistance. Using a Hall bar allows the noise power density of one equipotential line to be measured in the quantum Hall regime, which then corresponds to the transverse resistance as both equipotential lines are crossed travelling between the source and drain contacts. Using two contacts on opposite sides of the device allows the cross-spectral density to be found, which corresponds to the longitudinal resistance. However, they did this by looking at the introduction and increase of 1/f noise up to about 11 kHz as a result of applied current (and filling factor). Meanwhile, Chida et al. [99] employed a resonator set-up with a simple two-contact AlGaAs/GaAs heterostructure device, so the noise is determined by the transverse resistance on the plateau. They applied increasing bias voltage and record the 'excess noise', so-called because it is in excess of that caused by the device at thermal equilibrium. They observed a sharp breakdown behaviour

In transport measurements it is usually longitudinal resistance which is investigated at breakdown, because a deviation from zero resistance is more readily observable than deviation from the Hall resistance value. Typically $\Delta R_{xy} = k\ \Delta R_{xx}$, with $k \sim 0.7$ for GaAs and ~ 0.1 for graphene [127]. However, by using two amplifiers and extracting the cross-correlation of the excess noise, Chida et al. found that they were able to very sensitively determine not only the breakdown, but precursor behaviour attributed to non-equilibrium electrons with the quantum Hall state still intact. Below are presented investigations on Hall bars, using cross-correlation at one contact in a 4-terminal transport configuration together with transport measurement.

9.1. System validation using AlGaAs/GaAs 2DEG

Following tests of the probe and eliminating noise sources at room temperature, 77K and 4.2K, it was deemed at good idea to evaluate the system with a well known conventional 2DEG Hall bar device. This could then be compared to existing noise measurements of the QH regime. It also has the advantage of many features due to its parabolic energy dispersion, which then ought to give an idea of what to look for in the sparser graphene landscape.

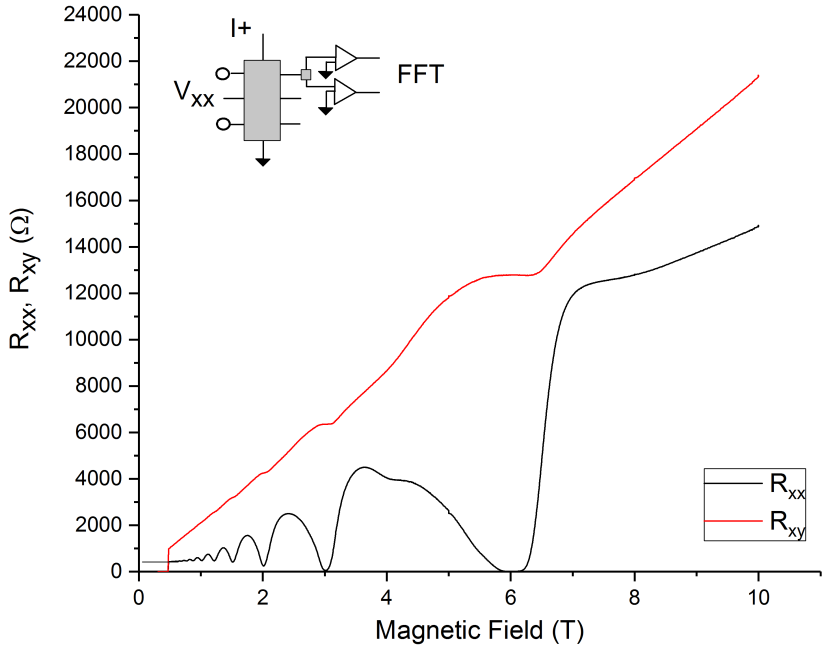

Figure 9.1.: R_{xx} and R_{xy} for GaAs with carrier density, n = 2.5×10^{11}cm^{-2}. The $\nu = 2$ plateau at 6T is fully quantised and just less than 0.4T wide.

As described earlier, the LC circuit together with the resistance of the device creates a resonance peak in voltage and using two amplifiers allows the correlation, Xr, of the noise to be extracted. Xr has subtracted the uncorrelated part of the noise, that is relevant to each amplifier, but unrelated to the sample of S1 and S2. As is clearly seen in figure 9.2 the background contributions of the amplifiers are much reduced.

The area under the resonance peak is a measure of dissipation and hence reflects the resistance of the device. the centre frequency is determined by L and C, while the width (at the full width half maximum) of the resonance is given by $1/2\pi RC$ (6.1). However,

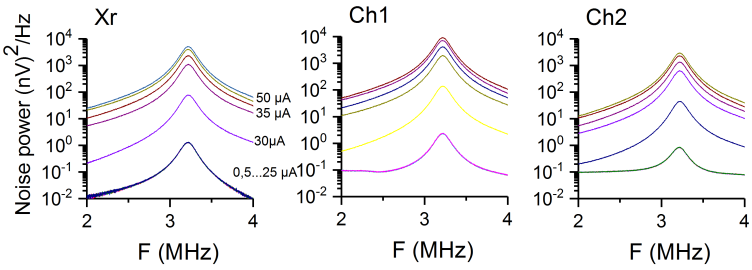

Figure 9.2.: Comparison of the noise powers (S1, S2) of the amplifiers on channel 1 and 2 with the correlation of the noise on the two channels, Xr at multiple currents.

here R is an effective resistance as it is actually the impedance of the measurement system as whole. For a measurement in the quantum Hall state, the amplifier will form a parallel resistance reducing the effective resistance accordingly.

The total square gain of the measurement system can be calculated by dividing the peak value by the effective resistance from the width. The effective resistance is what should be being recorded, while the peak is supposed to be that value multiplied by the gain.

Looking at figure 9.3a it is clear that the resistance is unchanging for a broad range of current then increases abruptly. Plotting the normalised Xr values against bias current this is revealed to be a very sharp breakdown behaviour (fig.9.3a).

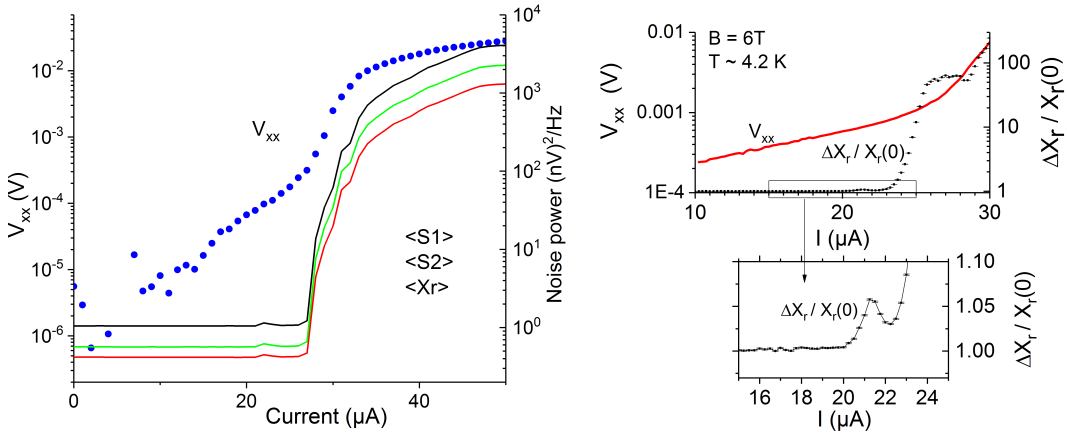

(a) The noise breakdown is very sharp and corresponds the change in V_{xx}.

(b) Normalised Xr shows the hump at 21µA to be precursor behaviour

Figure 9.3.: Breakdown and precursor behaviour

Figure 9.3a contrasts this sharp noise breakdown with V_{xx} and shows good agreement in

shape and position in current, indicating that it is indeed breakdown of the QH state. Below the critical current, I_c, V_{xx} is small but linear.

There is a slight rise in noise prior to I_c at about 21μA. In order to better examine it, change in correlated noise is plotted in figure 9.3b. Although still small, enlarging the feature it can be seen to be a well resolved precursor behaviour, with the feature better defined than even that seen by Chida et al. [99]. This indicates that this technique is a very sensitive measure for QH breakdown.

It is perhaps instructive to compare precursor behaviour to cyclotron emission by the device. As shown in many investigations [84, 83], CE occurs prior to breakdown, once the Hall slope is sufficient to generate significant non-equilibirum transport to the contacts. It then becomes much larger once breakdown occurs. Precursor behaviour in terms of the bootstrap heating model, can be interpreted as the presence of non-equlibrium electrons, but before the avalanche has fully developed.

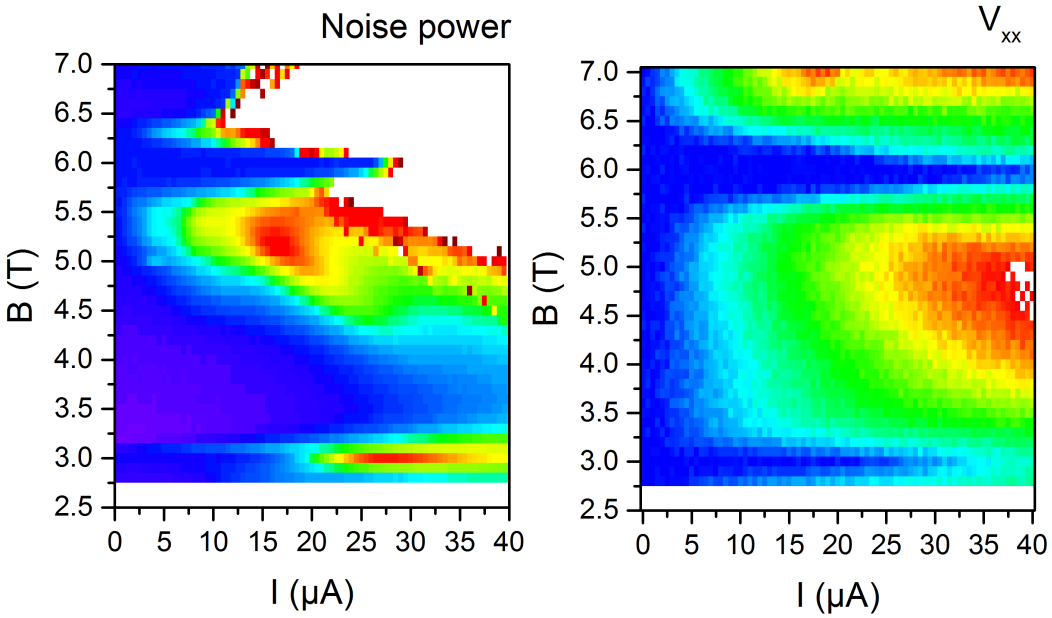

Figure 9.4.: Colour maps of noise power and V_{xx} over broad range of field and bias current. The $\nu = 2$ and $\nu = 4$ plateaus present in both. Noise is more sensitive to breakdown, but having V_{xx} for comparison helps to interpret the noise colour map.

By performing an automated series of current sweeps at different magnetic fields a colour

map of breakdown can be obtained (fig.9.4). Comparing the colour maps for V_{xx} and noise power it can be seen that both the $\nu = 2$ and $\nu = 4$ plateaus are well resolved. The noise is shown to be more sensitive to current, and so the breakdown on the plateaus are very sharp. Looking between the two plateaus it can be seen that it is also sensitive to the plateau broadening at $\nu = 2$ and therefore filling factor. The gradual change in V_{xx} does not reveal details of the system effectively, but does give better definition to the position of the plateau, so it seems the two plots are complimentary.

9.2. Noise measurement of epitaxial graphene

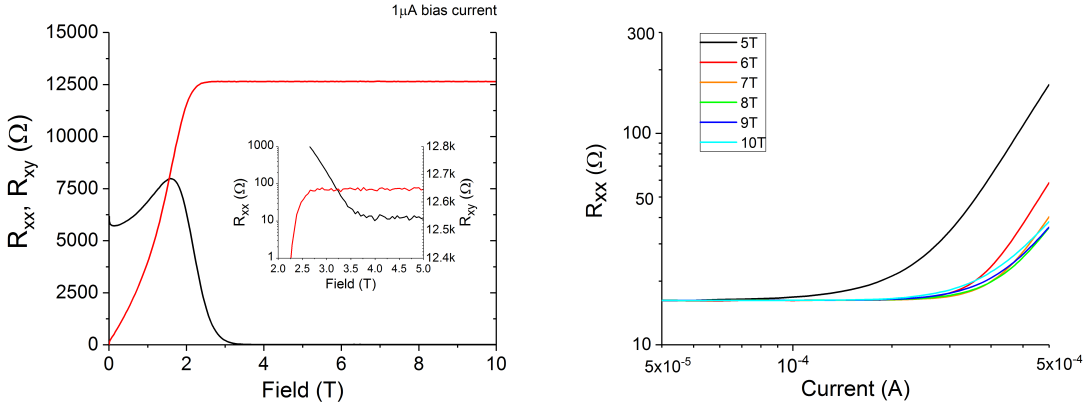

(a) R_{xx} vanishes but does not go to zero and R_{xy} reaches a plateau, but not of the quantised value.

(b) Breakdown-like behaviour is observed in R_{xx}, with very high values of I_c

Figure 9.5.: Transport on epitaxial graphene

Using the same configuration as for the GaAs measurement, an epitaxial graphene (EpiG) sample was mounted on the probe. However, as demonstrated in figure 9.5a, EpiG at low carrier density reaches the $\nu = 2$ plateau easily within 5T, and does not have multiple SdH oscillations. Instead there is wide plateau which ought to be well suited to investigating the breakdown of the quantum Hall effect.

It was found that the Hall bar had high contact resistance of 150Ω. In spite of this, the nominally $\nu = 2$ plateau showed very little deviation (fig.9.5a), and breakdown-like behaviour was observed at unexpectedly high bias currents (fig.9.5b) despite the absence of proper quantisation (fig.9.5a inset).

Breakdown current, I_c is usually the value at which the dissiptionless QH state becomes resistive once more. Since a significant increase in resistance is observed in this data, which constitutes a change in behaviour for the device, it will be referred to as breakdown current for simplicity.

There were shifts in initial transport and noise values, but collectively the datasets showed cohesive behaviour. Considering the high currents and prolonged measurement batches the device was subjected to, the shifts could be due to low level thermal cycling of the device.

The breakdown current can be observed for lower values of magnetic field of this wide $\nu = 2$ plateau, but are barely observable for higher magnetic field within the safely applicable bias current range of 600μA (fig.9.5b). I_c at 5T is markedly lower than for 6T, and the values for 7T to 10T are all closely grouped around the 6T value.

It is found that the noise behaviour agrees closely with the resistance and neither show any precursor behaviour (fig.9.5b, 9.6a). However, it is clear that this breakdown behaviour is much more gradual than for the GaAs device and is not the typical sharp breakdown.

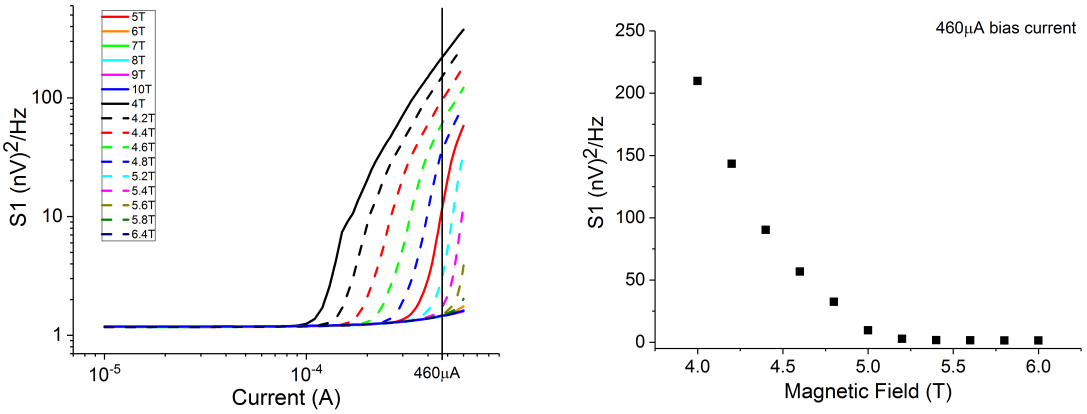

(a) Noise power spectrum curves for magneticfields between 4 and 10T.

(b) Fixed current (460μA)curve showing the noise power dependence on magnetic field.

Figure 9.6.: Noise at high magnetic field

The appearance of sharpness in the noise values is due to the log-log scale, but is also indicative of the greater sensitivity of the type of measurement. The breakdown current at 4T is much lower than for 5T, and so is left off fig 9.5b. The noise power curves for between 4T to 5T and between 5T and 6T are included in order to demonstrate that there is an S-shape present in the noise (fig 9.6a) albeit on a log-log scale. The S-shape is a key component of bootstrap type heating [77, 76], but despite the similarity here it evolves over hundreds of microamps.

At higher magnetic field (6-10T), not only is saturation not reached within the bias currents applied, the but the increase in noise is minimal. Excess noise at high field is the result of QH breakdown (fig.9.6a). For the grouped values of I_c barely any excess noise is seen.

The excess noise at low fields is the result of dissipative transport. Figure 9.7b shows a cross section at 40μA, which has a cross-over at 2T. This higher noise corresponds to the

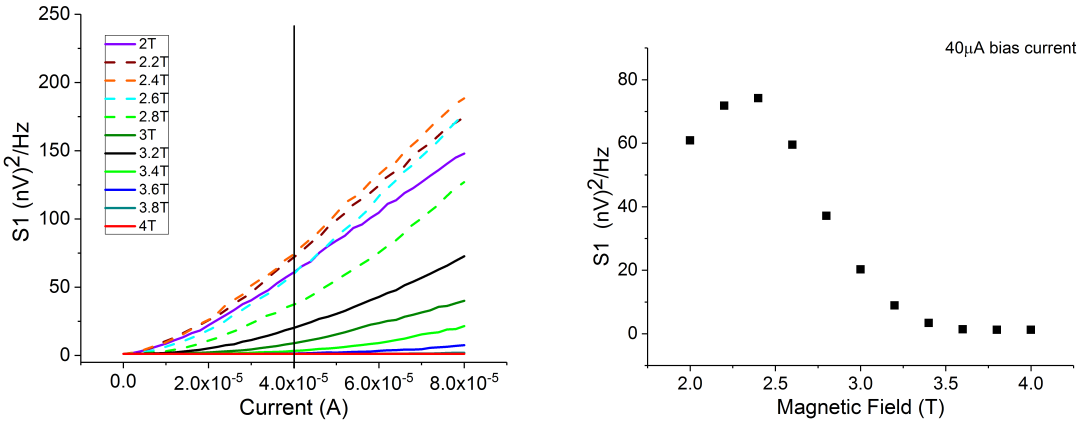

(a) Noise power spectrum curves for magnetic fields between 2 and 4T.

(b) Fixed current (40μA) section of noise curves showing the dependence on magnetic field.

Figure 9.7.: Noise at low magnetic field

sample resistance values as measured by magnetotransport. Comparing this to the inset of figure 9.3a), the crossover corresponds to the resistance which is dominant (prior to the plateau[1] this is R_{xx}).

In both high and low magnetic field the behaviour is determined by the relationship of the bias current to the available extended states. Considering the orders of magnitude higher current applied at high field there is remarkably little difference in the magnitude of noise recorded at low field and low current. The mechanism and dynamics behind the heating in the two regimes deserves further consideration, as despite the similarities, they ought be different as at low field simple dissipative heating occurs, while at high field the dissipationless state is broken.

The resistance plot of figure 9.5b is reproduced in figure 9.8 in more detail in order to demonstrate that there is a systematic cross-over behaviour in I_c. The highest I_c is obtained at 8T and there is a clear change in slope for the dissipative current on either side of it. The curves between 9T and 10T are included to demonstrate that these changes are a continuous transformation. The grouping and cross-over may be explained by charge transfer from the substrate which prevents deviation from exact integer filling as seen in [95].

[1] This is may be due to bias current, but longitudinal components were not reported in the one contact transverse resistance measurement by Schurr et al. [97].

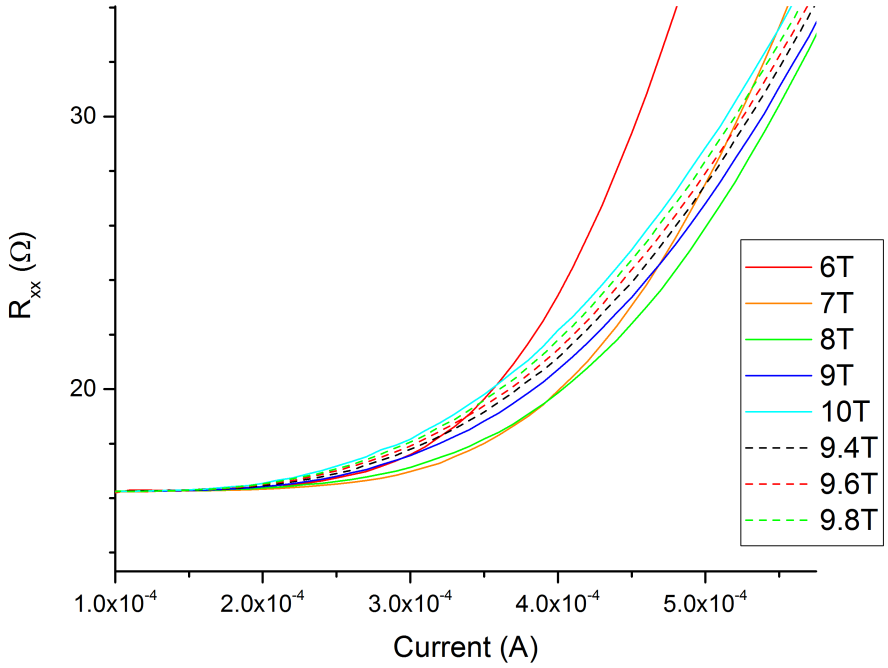

Figure 9.8.: The I_c values for B>6T are very close together, but still form a continuous crossover as maximum I_c is reached at 8T and the slope for dissipation alters.

However, choosing the value of I_c is made difficult by the similarity and grouping of the curves. While some deviation starts to occur at 200μA, it is difficult to quantify a change before 300μA, where the change in resistance is about 10%. Selecting 20Ω deviation to be the value for breakdown is an increase of 25% but the curves can be distinguished.

Alternatively looking at the change in resistance for the curves at 400μA where the 8T curve diverges from the 7T one, yields the type of asymmetry characteristic for plots of I_c against magnetic field or filling factor, but as seen for epitaxial graphene. In conventional 2DEGs the same plots are typified by symmetric 'triangle behaviour' [76] with the maximum at exactly integer filling factor. The asymmetry in EpiG is due to charge transfer, which has recently been shown to have strong magnetic field dependence [95]. As a result once on the $\nu = 2$ plateau and at integer filling the deviation away from it is predicted to be small and gradual, supporting this as the explanation for figure 9.8.

Unfortunately the bunching of I_c values at high field affects the noise measurements in the

same way. Nonetheless figure 9.6a shows there is an advantage in using noise to determine breakdown at lower fields as opposed using the resistance value. This is thanks to the sharpness of the increase, which may be due to the high sensitivity of the measurement system as seen with GaAs.

At low fields, i.e. before the plateau, the noise is high and dissipative. As a result the transport measurements need to be considered as well, because the current dependences of R_{xx} at different magnetic fields are not straight forward, so a constant value cannot simply be applied to obtain the temperature. Graph 9.9a shows the current dependence of the longitudinal resistance between 2T and 4T i.e. from the maximum of the SdH oscillation to the plateau. There is clear non-linear behaviour at low currents, and two gradients, resulting in a curvature which diminishes as the field is increased. While this is not under investigation here, it should be noted that the slope of this behaviour can be completely reversed at sufficiently high field.

High contact resistance is a possible cause for unusual non-linear behaviour at low bias currents (fig.9.9a), and may be the reason that R_{xx} did not go to zero, instead ranging between 11 and 18 ohms.

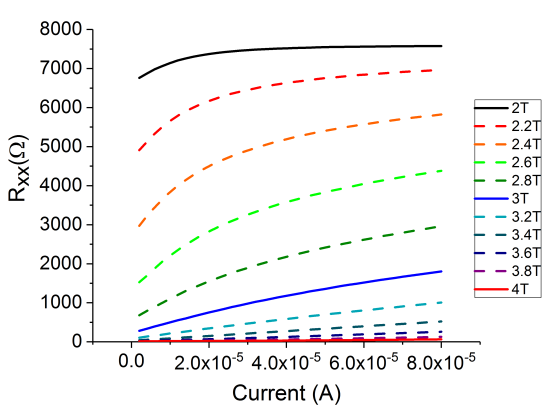

(a) A gradient is seen in the current dependence of R_{xx} with a curvature at low field attributed to an offset in the device.The gradient is reduced with increasing magnetic field and can even be reversed.

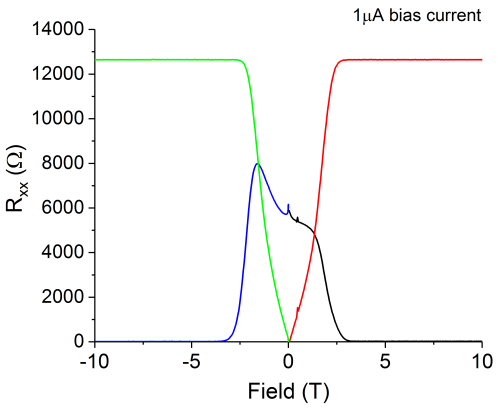

(b) R_{xx} and R_{xy} plotted for both field directions. There is a SdH oscillation for -B but not +B. The absence of the oscillation is a sometime feature of EpiG.

Figure 9.9.: Transport asymmetry and offset

The full range of behaviour, including measurement of different current ranges to check for consistency, was carried out from 0T to 10T and in both magnetic field polarities. The

same behaviours were seen, but were found to occur at different magnetic field and current values. This appears to be as a result of the asymmetric transport behaviour as seen in figure 9.9b). This suggests that the shift may be carrier density related and may explain why it is dependent on both current and field.

9.2.1. Evaluation of the breakdown

The theoretical thermal noise and ideal shot noise, $S_V = 4k_B R_{xy} + 2e\ I\ R_{xy}$ give large values because in this configuration R_{xy} dominates, giving 20 nV^2/Hz at 1μA, which is large even compared to the noise values found at breakdown. Additionally attempting to plot S_V divided by R_{xx} to relate it to temperature gave slow rising curves and S-shapes that could not be successfully quantified, nor related to a T^3 or T^4 energy loss rate.

Fortunately, Chida et al. [99] were able to correlate the excess noise observed as a result of quantum Hall breakdown with an electron temperature that was of the order of the cyclotron energy (10K). Theirs was a resonant circuit set up like the one used here and so it is possible to apply the same method of analysis. The use of the GaAs sample to test the measurement system will now make a direct comparison possible.

The peak of the resonance (in nV^2/Hz) is given by

$$P_0 = A\left[S_V + \left(\frac{ZR}{Z+R}\right)^2 S_I + \left(\frac{ZR}{Z+R}\right)^2 S_{dev}\right] \tag{9.1}$$

S_I and S_V are the current and voltage noise of the amplifiers, Z is the impedance of the system and R is the resistance of the device. A is the square of the total gain of the amplifier, which was found to be 7×10^5. S_{dev} is the excess noise caused by applying bias voltage plus the thermal noise at zero bias.

Where current and voltage noise of the amplifier are small, the first two terms become negligible. If the impedance is much greater than the resistance, then ZR/Z+R gives approximately the effective resistance, as found from width of the resonance. That value can be used, or, since the value of the device resistance in the quantum Hall state is close to the value of the effective resistance, an estimation can be made to simplify the term in brackets to R.

S_{dev} is current noise so rearranging the simplified relationship gives

$$S_I = \frac{P_0}{AR^2} \tag{9.2}$$

Making the approximation to R makes a small difference to S_I. The temperature is then $T_N = S/4k_BG$ where G is the conductance. In Chida there was a 10 percent change in conductance and the excess noise was observed to go from 0 to 30×10^{-27} A^2/Hz. By contrast in the GaAs sample used here the largest change in conductance (using $\Delta R_{xy} = k\ \Delta R_{xx}$) was 3 percent, but the change in noise at breakdown was three orders of magnitude (fig.9.3a). This means that even if, for example, S_I is calculated at the lowest, quantised value to be on the order of 1K, the resulting temperature after breakdown is improbably high.

Comparing the results of graphene to GaAs, due to the much more gradual increase, even the highest noise value recorded which was at 4T with 600μA bias curren (fig.9.6a) is an order of magnitude smaller than that recorded for GaAs. One way to investigate the difference in behaviour at breakdown between the two materials is to consider the relative amplitude of the noise.

In figures 9.6a and 9.7a the noise is given by the value of the peak, which increases by orders of magnitude with bias current, but which includes a background. The background is always an order of magnitude smaller than the peak value, so its subtraction has little effect, but figure 9.3b shows that the sensitivity of the measurement is increased if the peak is normalised by a zero current value. Similarly, normalising the peak by a value close to it (3MHz) is more sensitive to the change in peak with current: the relative amplitude.

For GaAs the highest relative peak is found at 30μA, but the shape of figure 9.8a actually agrees with figure 9.3a in terms of the bootstrap heating model [77, 76, 128]. At the critical current where the energy gain rate exceeds the energy loss rate and the avalanche of electron- hole pairs occurs, the noise has other contributing processes not just thermal ones and so shows a sharp increase. As saturation is approached with the loss rate exceeding the gain rate, a higher, but decreasing relative amplitude is found.

However for graphene the relative amplitudes are very similar at all bias currents, with slightly higher values before the breakdown-like increase in resistance and slightly lower afterwards. The highest value at 100μA could be a small increase from non-thermal contributions, but it is not possible to be sure especially due to the fluctuation in relative amplitude values.

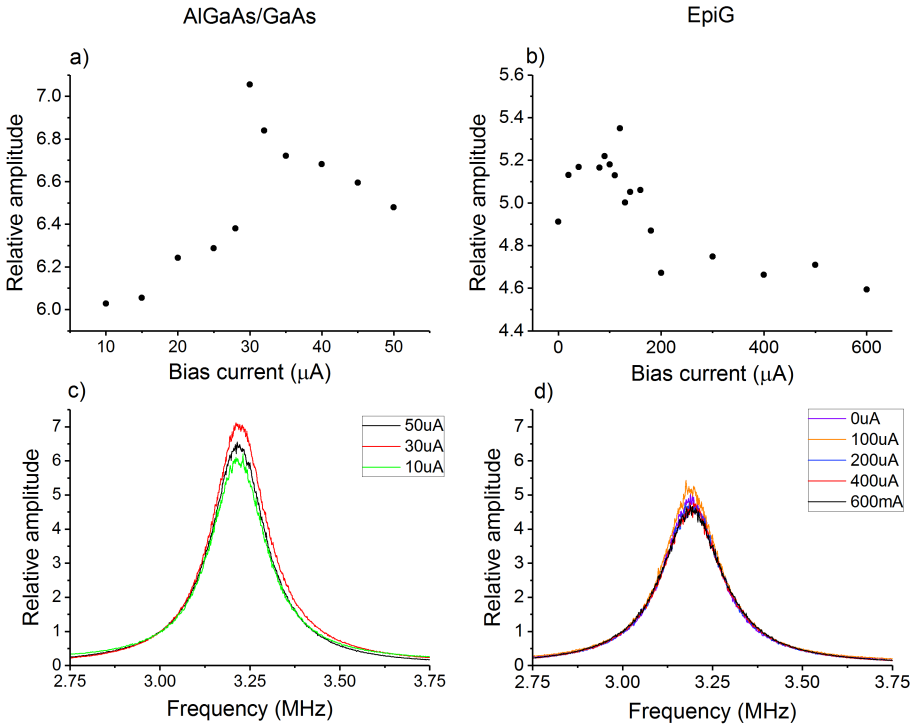

Figure 9.10.: c) and d) show the relative amplitude of the resonant noise peak, the peak divided by the value at 3MHz. For relative amplitude vs bias current shows GaAs (a) to have a marked increase at breakdown, with viable bootstrap type heating interpretation. For graphene (b) the relative amplitude changes little and actually decreases after breakdown.

There is currently no explanation for the lower relative amplitude after breakdown, but it suggests that the mechanisms that trigger avalanche type breakdown in GaAs are not present in graphene. It seems from log scale plots of the noise divided by longitudinal resistance (not included) that there is heating going on, but it is possible that the overheating is not suffiiciently large to overcome the length scale of the potential fluctuations [76]. At breakdown GaAs undergoes an order of magnitude increase in noise due to an increase in bias current of 2μA, while the same size of increase in noise for graphene requires an increase of 170μA. Together with the fact that in graphene there is no jump in either resistance or noise suggests a gradual overall change in the device, so the breakdown may originate in some way from the bulk rather than the edge states.

9.2.2. Discussion

Measurement of an AlGaAa/GaAs heterostructure allowed the measurement system to be characterised using a well a quantised device, which showed a sharp breakdown indicative of bootstrap heating. Using two channels to measure at one contact allows the measurement to be sensitive enough to detect precursor behaviour from the correlation of the noise, Xr. Obtaining colour maps also shows the greater sensitivity of the noise to breakdown, compared to V_{xx}, but also the need to use V_{xx} as a basis for comparison.

The graphene device, which was not fully quantised, showed breakdown-like behaviour but at very high bias currents. The noise measurements in particular showed very little increase at magnetic fields above 6T. The critical currents at 6T to 10T grouped together and did not show the triangle behaviour on the plateau that coventional 2DEGs do. There was a maximum value at 8T, and there was a notable change in the slope of the breakdown increase. Since the charge transfer on the $\nu = 2$ plateau for epitaxial graphene has been quantified [95] and shown to keep the filling factor close to integer filling over many tesla this result not only makes sense, but illustrates the magnetic field dependent charge transfer established in [95]. The gradual increase (and changing slopes) highlight the difficulty in how to define the critical current.

Qualitatively the sharp breakdown of the GaAs sample agrees extremely well with the findings of Chida et al. [99], but the noise increase is several orders of magnitude higher preventing the extraction of the electron temperature. If the one contact measurement of noise is considered to measure the proportion of states in the equipotential line, with breakdown resulting in the loss of some of those states, then the conductance and excess noise data of Chida et al. illustrates this well. If this is the case then a gradual, slow breakdown possibly indicates that a mechanism which is not directly coupled to the equipotential line is causing the change, and so it could originate in the bulk of the device.

10. Summary and Conclusion

During this project epitaxial graphene devices were investigated in magnetic fields and low temperature to evaluate some of properties of the material with respect to its use in the quantum standard for resistance.

The experimental work required a broad variety of equipment development, both individual and collaborative. A 12T cryostat to be operated at 4.2K was refurbished and a probe was constructed, wired and programmed for use with the tuning fork based scanning probe microscopy and also with an optical fibre. A quantum cascade laser was characterised before using it to evaluate the response of EpiG to 10μm irradiation. A puck for sample loading into a cryogen-free dilution refrigerator was modified. A probe for noise measurement was built together with homemade amplifiers and their power supply.

The heat dissipation, cyclotron resonance and quantum Hall breakdown of epitaxial graphene were investigated. Weak localisation measurements demonstrated energy loss rates proportional to $T_e^3 - T_L^3$, even under microwave irradiation. In graphene this is indicative of the presence of supercollisions, but the temperature of 8K is less than the value where they are expected to occur. It was also shown that up to the GHz regime no additional inelastic scattering is seen in EpiG due to microwave irradiation. The phase coherence time is shorter than the period of incoming radiation, so there is no time for direct interaction, and as a result the effect remains bolometric.

The cyclotron resonance of EpiG Hall bars was probed by irradiation at 10μm (30THz), but was not found. An unusual response was observed at the Shubnikov-de Haas oscillation instead, which in addition to being bolometric indicated a change in carrier density. After multiple attempts it seems that due to the very broad nature of the resonance in graphene, it covers a lot of localised states which means that high carrier densities are preferable for interacting with the cyclotron resonance. This is then at odds with the requirements for good quantisation, which would provide the best state for detecting resonant absorption because R_{xx} would go from zero to finite value.

The noise measurement setup using a resonant peak was found be very sensitive and successfully probed quantum Hall breakdown in GaAs. It was even able to reveal precursor behaviour with better resolution than that reported in [99]. When investigating epitaxial graphene no precursor behaviour was observed and any breakdown behaviour was smooth. The device was not properly quantised, but still exhibited breakdown-like behaviour with very high I_c of order 600μA. The breakdown current values were demonstrative of the charge transfer from the substrate on the $\nu = 2$ plateau, which maintains integer filling and creates the long width of the plateau.

Bibliography

[1] M. d. Podesta, "A new approach to the kelvin," *IEEE Instrumentation Measurement Magazine*, vol. 18, pp. 28–31, December 2015.

[2] M. de Podesta, "Rethinking the kelvin," *Nat Phys*, vol. 12, pp. 104–104, Jan. 2016.

[3] B. W. Petley, *The Fundamental Physical Constant and the Frontier of Measurement*. Adam Hilger Ltd, 1985.

[4] N. M. Zimmerman, "A primer on electrical units in the Syst'eme International," *American Journal of Physics*, vol. 66, no. 4, pp. 324–331, 1998.

[5] J. Flowers, "The route to atomic and quantum standards," *Science*, vol. 306, no. 5700, pp. 1324–1330, 2004.

[6] T. J. B. M. Janssen, S. Rozhko, I. Antonov, A. Tzalenchuk, J. M. Williams, Z. Melhem, H. He, S. Lara-Avila, S. Kubatkin, and R. Yakimova, "Operation of graphene quantum Hall resistance standard in a cryogen-free table-top system," *2D Materials*, vol. 2, no. 3, p. 035015, 2015.

[7] B. N. Taylor, "New international representations of the volt and ohm effective january 1, 1990," *IEEE Transactions on Instrumentation and Measurement*, vol. 39, pp. 2–5, Feb 1990.

[8] S. P. Giblin, S. J. Wright, J. D. Fletcher, M. Kataoka, M. Pepper, T. J. B. M. Janssen, D. A. Ritchie, C. A. Nicoll, D. Anderson, and G. A. C. Jones, "An accurate high-speed single-electron quantum dot pump," *New Journal of Physics*, vol. 12, no. 7, p. 073013, 2010.

[9] S. Giblin, M. Kataoka, J. Fletcher, P. See, T. Janssen, J. Griffiths, G. Jones, I. Farrer, and D. Ritchie, "Towards a quantum representation of the ampere using single electron pumps," *Nat Commun*, vol. 3, pp. 930–, July 2012.

[10] F. Stein, D. Drung, L. Fricke, H. Scherer, F. Hohls, C. Leicht, M. Gtz, C. Krause, R. Behr, E. Pesel, K. Pierz, U. Siegner, F. J. Ahlers, and H. W. Schumacher, "Validation of a quantized-current source with 0.2ppm uncertainty," *Applied Physics Letters*, vol. 107, no. 10, 2015.

[11] K. S. Novoselov, A. K. Geim, S. V. Morozov, D. Jiang, M. I. Katsnelson, I. V. Grigorieva, S. V. Dubonos, and A. A. Firsov, "Two-dimensional gas of massless Dirac fermions in graphene," *Nature*, vol. 438, pp. 197–200, Nov. 2005.

[12] T. Yager, A. Lartsev, K. Cedergren, R. Yakimova, V. Panchal, O. Kazakova, A. Tzalenchuk, K. H. Kim, Y. W. Park, S. Lara-Avila, and S. Kubatkin, "Low contact resistance in epitaxial graphene devices for quantum metrology," *AIP Advances*, vol. 5, no. 8, 2015.

[13] K. S. Novoselov, Z. Jiang, Y. Zhang, S. V. Morozov, H. L. Stormer, U. Zeitler, J. C. Maan, G. S. Boebinger, P. Kim, and A. K. Geim, "Room-temperature quantum Hall effect in graphene," *Science*, vol. 315, no. 5817, pp. 1379–1379, 2007.

[14] A. J. M. Giesbers, G. Rietveld, E. Houtzager, U. Zeitler, R. Yang, K. S. Novoselov, A. K. Geim, and J. C. Maan, "Quantum resistance metrology in graphene," *Applied Physics Letters*, vol. 93, no. 22, 2008.

[15] A. Tzalenchuk, S. Lara-Avila, A. Kalaboukhov, S. Paolillo, M. Syvajarvi, R. Yakimova, O. Kazakova, J. J. B. M., V. Fal'ko, and S. Kubatkin, "Towards a quantum resistance standard based on epitaxial graphene," *Nat Nano*, vol. 5, pp. 186–189, Mar. 2010.

[16] T. J. B. M. Janssen, N. E. Fletcher, R. Goebel, J. M. Williams, A. Tzalenchuk, R. Yakimova, S. Kubatkin, S. Lara-Avila, and V. I. Falko, "Graphene, universality of the quantum Hall effect and redefinition of the SI system," *New Journal of Physics*, vol. 13, no. 9, p. 093026, 2011.

[17] A. Satrapinski, S. Novikov, and N. Lebedeva, "Precision quantum Hall resistance measurement on epitaxial graphene device in low magnetic field," *Applied Physics Letters*, vol. 103, no. 17, 2013.

[18] T. Yager, A. Lartsev, S. Mahashabde, S. Charpentier, D. Davidovikj, A. Danilov, R. Yakimova, V. Panchal, O. Kazakova, A. Tzalenchuk, S. Lara-Avila, and S. Kubatkin, "Express optical analysis of epitaxial graphene on SiC: impact of morphology

on quantum transport," *Nano Letters*, vol. 13, no. 9, pp. 4217–4223, 2013. PMID: 23941358.

[19] A. Lartsev, S. Lara-Avila, A. Danilov, S. Kubatkin, A. Tzalenchuk, and R. Yakimova, "A prototype of Rk/200 quantum Hall array resistance standard on epitaxial graphene," *Journal of Applied Physics*, vol. 118, no. 4, 2015.

[20] K. S. Novoselov, A. K. Geim, S. V. Morozov, D. Jiang, Y. Zhang, S. V. Dubonos, I. V. Grigorieva, and A. A. Firsov, "Electric field effect in atomically thin carbon films," *Science*, vol. 306, no. 5696, pp. 666–669, 2004.

[21] A. K. Geim and K. S. Novoselov, "The rise of graphene," *Nat Mater*, vol. 6, pp. 183–191, Mar. 2007.

[22] P. R. Wallace, "The band theory of graphite," *Phys. Rev.*, vol. 71, pp. 622–634, May 1947.

[23] S. Latil and L. Henrard, "Charge carriers in few-layer graphene films," *Phys. Rev. Lett.*, vol. 97, p. 036803, Jul 2006.

[24] M. I. Katsnelson, "Graphene: carbon in two dimensions," *Materials Today*, vol. 10, no. 12, pp. 20 – 27, 2007.

[25] J. R. Wallbank, D. Ghazaryan, A. Misra, Y. Cao, J. S. Tu, B. A. Piot, M. Potemski, S. Pezzini, S. Wiedmann, U. Zeitler, T. L. M. Lane, S. V. Morozov, M. T. Greenaway, L. Eaves, A. K. Geim, V. I. Fal'ko, K. S. Novoselov, and A. Mishchenko, "Tuning the valley and chiral quantum state of Dirac electrons in van der Waals heterostructures," *Science*, vol. 353, no. 6299, pp. 575–579, 2016.

[26] V. V. Cheianov and V. I. Fal'ko, "Selective transmission of Dirac electrons and ballistic magnetoresistance of *n-p* junctions in graphene," *Phys. Rev. B*, vol. 74, p. 041403, Jul 2006.

[27] Fal'ko, "Electronic properties and the quantum hall effect in bilayer gaphene," *Phil. Trans. R. Soc. A*, vol. 366, no. 1863, pp. 205–219, 2008.

[28] Y. Liu, G. Bian, T. Miller, and T.-C. Chiang, "Visualizing electronic chirality and Berry phases in graphene systems using photoemission with circularly polarized light," *Phys. Rev. Lett.*, vol. 107, p. 166803, Oct 2011.

[29] M. T. Greenaway, E. E. Vdovin, A. Mishchenko, O. Makarovsky, A. Patane, J. R.

Wallbank, Y. Cao, A. V. Kretinin, M. J. Zhu, S. V. Morozov, V. I. Fal[rsquor]ko, K. S. Novoselov, A. K. Geim, T. M. Fromhold, and L. Eaves, "Resonant tunnelling between the chiral Landau states of twisted graphene lattices," *Nat Phys*, vol. 11, pp. 1057–1062, Dec. 2015.

[30] A. K. Geim, "Graphene: Status and prospects," *Science*, vol. 324, no. 5934, pp. 1530–1534, 2009.

[31] S. Bae, H. Kim, Y. Lee, X. Xu, J.-S. Park, Y. Zheng, J. Balakrishnan, T. Lei, H. Ri Kim, Y. I. Song, Y.-J. Kim, K. S. Kim, B. Ozyilmaz, J.-H. Ahn, B. H. Hong, and S. Iijima, "Roll-to-roll production of 30-inch graphene films for transparent electrodes," *Nat Nano*, vol. 5, pp. 574–578, Aug. 2010.

[32] Y. Hernandez, V. Nicolosi, M. Lotya, F. M. Blighe, Z. Sun, S. De, M. T., B. Holland, M. Byrne, Y. K. Gun'Ko, J. J. Boland, P. Niraj, G. Duesberg, S. Krishnamurthy, R. Goodhue, J. Hutchison, V. Scardaci, A. C. Ferrari, and J. N. Coleman, "High-yield production of graphene by liquid-phase exfoliation of graphite," *Nat Nano*, vol. 3, pp. 563–568, Sept. 2008.

[33] K. R. Paton, E. Varrla, C. Backes, R. J. Smith, U. Khan, A. ONeill, C. Boland, M. Lotya, O. M. Istrate, P. King, T. Higgins, S. Barwich, P. May, P. Puczkarski, I. Ahmed, M. Moebius, H. Pettersson, E. Long, J. Coelho, S. E. OBrien, E. K. McGuire, B. M. Sanchez, G. S. Duesberg, N. McEvoy, T. J. Pennycook, C. Downing, A. Crossley, V. Nicolosi, and J. N. Coleman, "Scalable production of large quantities of defect-free few-layer graphene by shear exfoliation in liquids," *Nat Mater*, vol. 13, pp. 624–630, June 2014.

[34] A. C. Ferrari, J. C. Meyer, V. Scardaci, C. Casiraghi, M. Lazzeri, F. Mauri, S. Piscanec, D. Jiang, K. S. Novoselov, S. Roth, and A. K. Geim, "Raman spectrum of graphene and graphene layers," *Phys. Rev. Lett.*, vol. 97, p. 187401, Oct 2006.

[35] T. Ohta, A. Bostwick, J. L. McChesney, T. Seyller, K. Horn, and E. Rotenberg, "Interlayer interaction and electronic screening in multilayer graphene investigated with angle-resolved photoemission spectroscopy," *Phys. Rev. Lett.*, vol. 98, p. 206802, May 2007.

[36] K. V. Emtsev, F. Speck, T. Seyller, L. Ley, and J. D. Riley, "Interaction, growth, and ordering of epitaxial graphene on SiC(0001) surfaces: A comparative photoelectron spectroscopy study," *Phys. Rev. B*, vol. 77, p. 155303, Apr 2008.

[37] K. V. Emtsev, A. Bostwick, K. Horn, J. Jobst, G. L. Kellogg, L. Ley, J. L. McChesney, T. Ohta, S. A. Reshanov, J. Rohrl, E. Rotenberg, A. K. Schmid, D. Waldmann, H. B. Weber, and T. Seyller, "Towards wafer-size graphene layers by atmospheric pressure graphitization of silicon carbide," *Nat Mater*, vol. 8, pp. 203–207, Mar. 2009.

[38] T. Yager, A. Lartsev, S. Mahashabde, S. Charpentier, D. Davidovikj, A. Danilov, R. Yakimova, V. Panchal, O. Kazakova, A. Tzalenchuk, S. Lara-Avila, and S. Kubatkin, "Express optical analysis of epitaxial graphene on SiC: Impact of morphology on quantum transport," *Nano Letters*, vol. 13, no. 9, pp. 4217–4223, 2013. PMID: 23941358.

[39] P. Blake, E. W. Hill, A. H. Castro Neto, K. S. Novoselov, D. Jiang, R. Yang, T. J. Booth, and A. K. Geim, "Making graphene visible," *Applied Physics Letters*, vol. 91, no. 6, 2007.

[40] Luxmi, S. Nie, P. Fisher, R. Feenstra, G. Gu, and Y. Sun, "Temperature dependence of epitaxial graphene formation on SiC(0001)," *Journal of Electronic Materials*, vol. 38, no. 6, pp. 718–724, 2008.

[41] P. T. B. Shaffer, "A review of the structure of silicon carbide," *Acta Crystallographica Section B*, vol. 25, pp. 477–488, Mar 1969.

[42] L. S. Ramsdell, "Studies on silicon carbide," *Am. Mineral.*, vol. 32, pp. 64–82, Feb 1947.

[43] G. Harris, ed., *Properties of silicon carbide*. INSPEC, London,1995.

[44] R. Yakimova, T. Iakimov, G. Yazdi, C. Bouhafs, J. Eriksson, A. Zakharov, A. Boosalis, M. Schubert, and V. Darakchieva, "Morphological and electronic properties of epitaxial graphene on SiC," *Physica B: Condensed Matter*, vol. 439, pp. 54 – 59, 2014. 5th South African Conference on Photonic Materials (SACPM 2013).

[45] H. Huang, W. Chen, S. Chen, and A. T. S. Wee, "Bottom-up growth of epitaxial graphene on 6H-SiC(0001)," *ACS Nano*, vol. 2, no. 12, pp. 2513–2518, 2008.

[46] J. Kim, H. Park, J. B. Hannon, S. W. Bedell, K. Fogel, D. K. Sadana, and C. Dimitrakopoulos, "Layer-resolved graphene transfer via engineered strain layers," *Science*, vol. 342, no. 6160, pp. 833–836, 2013.

[47] N. Srivastava, G. He, Luxmi, P. C. Mende, R. M. Feenstra, and Y. Sun, "Graphene

formed on SiC under various environments: comparison of Si-face and C-face," *Journal of Physics D: Applied Physics*, vol. 45, no. 15, p. 154001, 2012.

[48] J. B. Hannon and R. M. Tromp, "Pit formation during graphene synthesis on SiC(0001): *In situ* electron microscopy," *Phys. Rev. B*, vol. 77, p. 241404, Jun 2008.

[49] F. Varchon, R. Feng, J. Hass, X. Li, B. N. Nguyen, C. Naud, P. Mallet, J.-Y. Veuillen, C. Berger, E. H. Conrad, and L. Magaud, "Electronic structure of epitaxial graphene layers on SiC: Effect of the substrate," *Phys. Rev. Lett.*, vol. 99, p. 126805, Sep 2007.

[50] S. Kopylov, A. Tzalenchuk, S. Kubatkin, and V. I. Falko, "Charge transfer between epitaxial graphene and silicon carbide," *Applied Physics Letters*, vol. 97, no. 11, 2010.

[51] J. A. Alexander-Webber, A. M. R. Baker, T. J. B. M. Janssen, A. Tzalenchuk, S. Lara-Avila, S. Kubatkin, R. Yakimova, B. A. Piot, D. K. Maude, and R. J. Nicholas, "Phase space for the breakdown of the quantum Hall effect in epitaxial graphene," *Phys. Rev. Lett.*, vol. 111, p. 096601, Aug 2013.

[52] T. J. B. M. Janssen, A. Tzalenchuk, S. Lara-Avila, S. Kubatkin, and V. I. Fal'ko, "Quantum resistance metrology using graphene," *Reports on Progress in Physics*, vol. 76, no. 10, p. 104501, 2013.

[53] G. Bergmann, "Weak localization in thin films: a time-of-flight experiment with conduction electrons," *Physics Reports*, vol. 107, no. 1, pp. 1 – 58, 1984.

[54] F. V. Tikhonenko, A. A. Kozikov, A. K. Savchenko, and R. V. Gorbachev, "Transition between electron localization and antilocalization in graphene," *Phys. Rev. Lett.*, vol. 103, p. 226801, Nov 2009.

[55] E. McCann, K. Kechedzhi, V. I. Fal'ko, H. Suzuura, T. Ando, and B. L. Altshuler, "Weak-localization magnetoresistance and valley symmetry in graphene," *Phys. Rev. Lett.*, vol. 97, p. 146805, Oct 2006.

[56] E. McCann, "Staying or going? Chirality decides!," *Physics*, vol. 2, p. 98, Nov 2009.

[57] H. Suzuura and T. Ando, "Crossover from symplectic to orthogonal class in a two-dimensional honeycomb lattice," *Phys. Rev. Lett.*, vol. 89, p. 266603, Dec 2002.

[58] F. V. Tikhonenko, D. W. Horsell, R. V. Gorbachev, and A. K. Savchenko, "Weak localization in graphene flakes," *Phys. Rev. Lett.*, vol. 100, p. 056802, Feb 2008.

[59] S. Lara-Avila, A. Tzalenchuk, S. Kubatkin, R. Yakimova, T. J. B. M. Janssen, K. Cedergren, T. Bergsten, and V. Fal'ko, "Disordered Fermi liquid in epitaxial graphene from quantum transport measurements," *Phys. Rev. Lett.*, vol. 107, p. 166602, Oct 2011.

[60] P. A. Lee and T. V. Ramakrishnan, "Disordered electronic systems," *Rev. Mod. Phys.*, vol. 57, pp. 287–337, Apr 1985.

[61] V. I. Fal'ko, "Effect of a microwave field on the quantum correction to the conductivity," *Sov. Phys. JETP*, vol. 65, no. 2, pp. 397–399, 1987.

[62] J. Q. Zhang, S. Vitkalov, and A. A. Bykov, "Nonlinear resistance of two-dimensional electrons in crossed electric and magnetic fields," *Phys. Rev. B*, vol. 80, p. 045310, Jul 2009.

[63] S. Wang and P. E. Lindelof, "Microwave-enhanced phase-relaxation observed in weak-localization experiments," *Phys. Rev. Lett.*, vol. 59, pp. 1156–1159, Sep 1987.

[64] A. M. R. Baker, J. A. Alexander-Webber, T. Altebaeumer, and R. J. Nicholas, "Energy relaxation for hot Dirac fermions in graphene and breakdown of the quantum Hall effect," *Phys. Rev. B*, vol. 85, 2012.

[65] Z. Tan, C. Tan, L. Ma, G. T. Liu, L. Lu, and C. L. Yang, "Shubnikov-de Haas oscillations of a single layer graphene under dc current bias," *Phys. Rev. B*, vol. 84, p. 115429, Sep 2011.

[66] S. S. Kubakaddi, "Interaction of massless Dirac electrons with acoustic phonons in graphene at low temperatures," *Phys. Rev. B*, vol. 79, p. 075417, Feb 2009.

[67] A. C. Betz, S. H. Jhang, E. Pallecchi, R. Ferreira, G. Feve, J.-M. Berroir, and B. Placais, "Supercollision cooling in undoped graphene," *Nat Phys*, vol. 9, pp. 109–112, Feb. 2013.

[68] A. C. Betz, F. Vialla, D. Brunel, C. Voisin, M. Picher, A. Cavanna, A. Madouri, G. Fève, J.-M. Berroir, B. Plaçais, and E. Pallecchi, "Hot electron cooling by acoustic phonons in graphene," *Phys. Rev. Lett.*, vol. 109, p. 056805, Aug 2012.

[69] M. W. Graham, S.-F. Shi, D. C. Ralph, J. Park, and P. L. McEuen, "Photocurrent measurements of supercollision cooling in graphene," *Nat Phys*, vol. 9, pp. 103–108, Feb. 2013.

[70] T. S. M. T. J. A. T. S. L.-A. S. R. Y. C.-T. L.-J. L. A.M.R. Baker, J.A. Alexander-Webber and R.J.Nicholas, "Energy loss rates of hot Dirac fermions in epitaxial, exfoliated, and cvd graphene," *Phys. Rev. B*, vol. 87, 2013.

[71] J. A. Alexander-Webber, A. M. R. Baker, P. D. Buckle, T. Ashley, and R. Nicholas, "High-current breakdown of the quantum Hall effect and electron heating in InSb/AlInSb," *Phys. Rev. B*, vol. 86, 2012.

[72] Y. Ma, R. Fletcher, E. Zaremba, M. D'Iorio, C. T. Foxon, and J. J. Harris, "Energy-loss rates of two-dimensional electrons at a GaAs/Al_xGa_{1-x}As interface," *Phys. Rev. B*, vol. 43, pp. 9033–9044, Apr 1991.

[73] D. K. Efetov and P. Kim, "Controlling electron-phonon interactions in graphene at ultrahigh carrier densities," *Phys. Rev. Lett.*, vol. 105, p. 256805, Dec 2010.

[74] M. Fuhrer, "Viewpoint: Textbook physics from a cutting-edge material," *Physics 3, 106*, 2010.

[75] K. von Klitzing, "Developments in the quantum Hall effect," *Phil. Trans. R. Soc. A*, vol. 363, pp. 2203–2219, 2005.

[76] S. Komiyama and Y. Kawaguchi, "Heat instability of quantum Hall conductors," *Phys. Rev. B*, vol. 61, pp. 2014–2027, Jan 2000.

[77] S. Komiyama, T. Takamasu, S. Hiyamizu, and S. Sasa, "Breakdown of the quantum Hall effect due to electron heating," *Solid State Communications*, vol. 54, no. 6, pp. 479 – 484, 1985.

[78] U. Klass, W. Dietsche, K. Klitzing, and K. Ploog, "Imaging of the dissipation in quantum-Hall-effect experiments," *Zeitschrift fr Physik B Condensed Matter*, vol. 82, no. 3, pp. 351–354, 1991.

[79] N. N. Zinovev, A. V. Akimov, L. J. Challis, A. F. Jezierski, and M. Henini, "Far-infrared emission from two-dimensional electron and hole gases in GaAs/(AlGa)As heterojunctions," *Semiconductor Science and Technology*, vol. 9, no. 5S, p. 831, 1994.

[80] S. Komiyama, H. Sakuma, K. Ikushima, and K. Hirakawa, "Electron temperature of hot spots in quantum Hall conductors," *Phys. Rev. B*, vol. 73, p. 045333, Jan 2006.

[81] M. Büttiker, "Absence of backscattering in quantum Hall conductors multiprobe conductors," *Phys. Rev. B*, vol. 38, p. 9375, 1988.

[82] P. C. van Son and T. M. Klapwijk, "Current contacts and current distribution in the quantum Hall effect," *EPL (Europhysics Letters)*, vol. 12, no. 5, p. 429, 1990.

[83] Y. Kawano, Y. Hisanaga, and S. Komiyama, "Cyclotron emission from quantized Hall devices: injection of nonequilibrium electrons from contacts," *Phys. Rev. B*, vol. 59, pp. 12537–12546, May 1999.

[84] K. Ikushima, H. Sakuma, S. Komiyama, and K. Hirakawa, "Imaging of cyclotron emission from edge channels in quantum Hall conductors," *Phys. Rev. Lett.*, vol. 93, p. 146804, Sep 2004.

[85] T. J. B. M. Janssen, A. Tzalenchuk, R. Yakimova, S. Kubatkin, S. Lara-Avila, S. Kopylov, and V. I. Fal'ko, "Anomalously strong pinning of the filling factor ν=2 in epitaxial graphene," *Phys. Rev. B*, vol. 83, p. 233402, Jun 2011.

[86] V. Eless, T. Yager, S. Spasov, S. Lara-Avila, R. Yakimova, S. Kubatkin, T. J. B. M. Janssen, A. Tzalenchuk, and V. Antonov, "Phase coherence and energy relaxation in epitaxial graphene under microwave radiation," *Applied Physics Letters*, vol. 103, no. 9, p. 093103, 2013.

[87] P. Avouris and C. Dimitrakopoulos, "Graphene: synthesis and applications," *Materials Today*, vol. 15, no. 3, pp. 86 – 97, 2012.

[88] Y. Kawaguchi, K. Hirakawa, M. Saeki, K. Yamanaka, and S. Komiyama, "Performance of high-sensitivity quantum Hall far infrared photodetectors," *Applied Physics Letters*, vol. 80, no. 1, pp. 136–138, 2002.

[89] N. G. Kalugin, L. Jing, W. Bao, L. Wickey, C. Del Barga, M. Ovezmyradov, E. A. Shaner, and C. N. Lau, "Graphene-based quantum Hall effect infrared photodetector operating at liquid nitrogen temperatures," *Applied Physics Letters*, vol. 99, no. 1, 2011.

[90] M. Orlita and M. Potemski, "Dirac electronic states in graphene systems: optical spectroscopy studies," *Semiconductor Science and Technology*, vol. 25, no. 6, p. 063001, 2010.

[91] W. Heiss, P. Auer, E. Gornik, C. R. Pidgeon, C. J. G. M. Langerak, B. N. Murdin, G. Weimann, and M. Heiblum, "Determination of Landau level lifetimes in AlGaAs/GaAs heterostructures with a ps free electron laser," *Applied Physics Letters*, vol. 67, no. 8, pp. 1110–1112, 1995.

[92] R. Horstman, E. Broek, J. Wolter, R. van der Heijden, G. Rikken, H. Sigg, P. Frijlink, J. Maluenda, and J. Hallais, "Cyclotron resonance from the far-infrared transmission and the photoconductivity of a two-dimensional electron gas in a GaAs/AlGaAs heterojunction," *Solid State Communications*, vol. 50, no. 8, pp. 753 – 756, 1984.

[93] K.-C. Chuang, R. S. Deacon, R. J. Nicholas, K. S. Novoselov, and A. K. Geim, "Cyclotron resonance of electrons and holes in graphene monolayers," *Philosophical Transactions of the Royal Society of London A: Mathematical, Physical and Engineering Sciences*, vol. 366, no. 1863, pp. 237–243, 2008.

[94] R. S. Deacon, K.-C. Chuang, R. J. Nicholas, K. S. Novoselov, and A. K. Geim, "Cyclotron resonance study of the electron and hole velocity in graphene monolayers," *Phys. Rev. B*, vol. 76, p. 081406, Aug 2007.

[95] J. A. Alexander-Webber, J. Huang, D. K. Maude, T. J. B. M. Janssen, A. Tzalenchuk, V. Antonov, T. Yager, S. Lara-Avila, S. Kubatkin, R. Yakimova, and R. J. Nicholas, "Giant quantum Hall plateaus generated by charge transfer in epitaxial graphene," *Scientific Reports*, vol. 6, pp. 30296–, July 2016.

[96] J. Schurr, H. Moser, K. Pierz, G. Ramm, and B. P. Kibble, "Johnson - Nyquist noise of the quantized Hall resistance," *IEEE Transactions on Instrumentation and Measurement*, vol. 60, pp. 2280–2285, July 2011.

[97] J. Schurr, F. Ahlers, and L. Callegaro, "Noise and correlation study of quantum Hall devices," *IEEE Transactions on Instrumentation and Measurement*, vol. 62, pp. 1574–1580, June 2013.

[98] M. Büttiker, "Scattering theory of thermal and excess noise in open conductors," *Phys. Rev. Lett.*, vol. 65, pp. 2901–2904, Dec 1990.

[99] K. Chida, T. Arakawa, S. Matsuo, Y. Nishihara, T. Tanaka, D. Chiba, T. Ono, T. Hata, K. Kobayashi, and T. Machida, "Observation of finite excess noise in the voltage-biased quantum Hall regime as a precursor for breakdown," *Phys. Rev. B*, vol. 87, p. 155313, Apr 2013.

[100] L. DiCarlo, J. R. Williams, Y. Zhang, D. T. McClure, and C. M. Marcus, "Shot noise in graphene," *Phys. Rev. Lett.*, vol. 100, p. 156801, Apr 2008.

[101] J. Tworzydło, B. Trauzettel, M. Titov, A. Rycerz, and C. W. J. Beenakker, "Sub-Poissonian Shot noise in graphene," *Phys. Rev. Lett.*, vol. 96, p. 246802, Jun 2006.

[102] Katsnelson, M. I., "Zitterbewegung, chirality, and minimal conductivity in graphene," *Eur. Phys. J. B*, vol. 51, no. 2, pp. 157–160, 2006.

[103] A. Lartsev, T. Yager, T. Bergsten, A. Tzalenchuk, T. J. B. M. Janssen, R. Yakimova, S. Lara-Avila, and S. Kubatkin, "Tuning carrier density across Dirac point in epitaxial graphene on SiC by corona discharge," *Applied Physics Letters*, vol. 105, no. 6, 2014.

[104] J. S. Moon, D. Curtis, S. Bui, M. Hu, D. K. Gaskill, J. L. Tedesco, P. Asbeck, G. G. Jernigan, B. L. VanMil, R. L. Myers-Ward, C. R. Eddy, P. M. Campbell, and X. Weng, "Top-gated epitaxial graphene fets on Si-face SiC wafers with a peak transconductance of 600 mS/mm," *IEEE Electron Device Letters*, vol. 31, pp. 260–262, April 2010.

[105] F. Speck, J. Jobst, F. Fromm, M. Ostler, D. Waldmann, M. Hundhausen, H. B. Weber, and T. Seyller, "The quasi-free-standing nature of graphene on H-saturated SiC(0001)," *Applied Physics Letters*, vol. 99, no. 12, 2011.

[106] M. Tokarczyk, G. Kowalski, M. Modonek, J. Borysiuk, R. Stpniewski, W. Strupiski, P. Ciepielewski, and J. M. Baranowski, "Structural investigations of hydrogenated epitaxial graphene grown on 4H-SiC (0001)," *Applied Physics Letters*, vol. 103, no. 24, 2013.

[107] S. Lara-Avila, *Magnetotransport characterization of epitaxial graphene on SiC*. PhD thesis, Chalmers University of Technology, 2012.

[108] S. Lara-Avila, K. Moth-Poulsen, R. Yakimova, T. Bjørnholm, V. Falko, A. Tzalenchuk, and S. Kubatkin, "Non-volatile photochemical gating of an epitaxial graphene/polymer heterostructure," *Advanced Materials*, vol. 23, no. 7, pp. 878–882, 2011.

[109] V. Eless, "The dynamics of the photochemical gating of epitaxial graphene," Master's thesis, Royal Holloway, University of London, 2012.

[110] M. M. Shahin, "Mass spectrometric studies of corona discharges in air at atmospheric pressures," *The Journal of Chemical Physics*, vol. 45, no. 7, pp. 2600–2605, 1966.

[111] M. M. Shahin, "Nature of charge carriers in negative coronas," *Appl. Opt.*, vol. 8, pp. 106–110, Jan 1969.

[112] R. B. Comizzoli, "Uses of corona discharges in the semiconductor industry," *Journal of The Electrochemical Society*, vol. 134, no. 2, pp. 424–429, 1987.

[113] E. R. Abraham and E. A. Cornell, "Teflon feedthrough for coupling optical fibers into ultrahigh vacuum systems," *Appl. Opt.*, vol. 37, pp. 1762–1763, Apr 1998.

[114] L. DiCarlo, Y. Zhang, D. T. McClure, C. M. Marcus, L. N. Pfeiffer, and K. W. West, "System for measuring auto- and cross correlation of current noise at low temperatures," *Review of Scientific Instruments*, vol. 77, no. 7, 2006.

[115] Y. Kawano, Y. Hisanaga, H. Takenouchi, and S. Komiyama, "Highly sensitive and tunable detection of far-infrared radiation by quantum Hall devices," *Journal of Applied Physics*, vol. 89, no. 7, pp. 4037–4048, 2001.

[116] Z. Jiang, Y. Zhang, H. L. Stormer, and P. Kim, "Quantum Hall states near the charge-neutral Dirac point in graphene," *Phys. Rev. Lett.*, vol. 99, p. 106802, Sep 2007.

[117] Z. Jiang, E. A. Henriksen, L. C. Tung, Y.-J. Wang, M. E. Schwartz, M. Y. Han, P. Kim, and H. L. Stormer, "Infrared spectroscopy of Landau levels of graphene," *Phys. Rev. Lett.*, vol. 98, p. 197403, May 2007.

[118] E. A. Henriksen, Z. Jiang, L.-C. Tung, M. E. Schwartz, M. Takita, Y.-J. Wang, P. Kim, and H. L. Stormer, "Cyclotron resonance in bilayer graphene," *Phys. Rev. Lett.*, vol. 100, p. 087403, Feb 2008.

[119] M. L. Sadowski, G. Martinez, M. Potemski, C. Berger, and W. A. de Heer, "Landau level spectroscopy of ultrathin graphite layers," *Phys. Rev. Lett.*, vol. 97, p. 266405, Dec 2006.

[120] Y. B. Vasil'ev, S. D. Suchalkin, Y. L. I. Ivanov, P. S. S. V. Kop'ev, and I. G. Savel'ev, "Photoconductivity under the conditions of the quantum Hall effect," *JETP Lett*, vol. 56, no. 8, p. 377, 1992.

[121] N. G. Kalugin, Y. B. Vasilyev, S. D. Suchalkin, G. Nachtwei, B. E. Sagol, and K. Eberl, "Dynamics of the far-infrared photoresponse in quantum Hall systems," *Phys. Rev. B*, vol. 66, p. 085308, Aug 2002.

[122] S. Masubuchi, M. Onuki, M. Arai, T. Yamaguchi, K. Watanabe, T. Taniguchi, and T. Machida, "Photovoltaic infrared photoresponse of the high-mobility graphene

quantum Hall system due to cyclotron resonance," *Phys. Rev. B*, vol. 88, p. 121402, Sep 2013.

[123] T. J. B. M. Janssen, A. Tzalenchuk, R. Yakimova, S. Kubatkin, S. Lara-Avila, S. Kopylov, and V. I. Fal'ko, "Anomalously strong pinning of the filling factor $\nu = 2$ in epitaxial graphene," *Phys. Rev. B*, vol. 83, p. 233402, Jun 2011.

[124] W. Zhang, H.-S. Chiang, M. A. Zudov, L. N. Pfeiffer, and K. W. West, "Magneto-transport in a two-dimensional electron system in dc electric fields," *Phys. Rev. B*, vol. 75, p. 041304, Jan 2007.

[125] J. Q. Zhang, S. Vitkalov, and A. A. Bykov, "Nonlinear resistance of two-dimensional electrons in crossed electric and magnetic fields," *Phys. Rev. B*, vol. 80, p. 045310, Jul 2009.

[126] I. A. Dmitriev, M. G. Vavilov, I. L. Aleiner, A. D. Mirlin, and D. G. Polyakov, "Theory of microwave-induced oscillations in the magnetoconductivity of a two-dimensional electron gas," *Phys. Rev. B*, vol. 71, p. 115316, Mar 2005.

[127] T. J. B. M. Janssen, J. M. Williams, N. E. Fletcher, R. Goebel, A. Tzalenchuk, R. Yakimova, S. Lara-Avila, S. Kubatkin, and V. I. Fal'ko, "Precision comparison of the quantum Hall effect in graphene and gallium arsenide," *Metrologia*, vol. 49, no. 3, p. 294, 2012.

[128] Y. Kawano and T. Okamoto, "Noise-voltage mapping by a quantum-Hall electrometer," *Applied Physics Letters*, vol. 87, no. 25, 2005.